ALMA MATER STUDIORUM
UNIVERSITÀ DI BOLOGNA

Facoltà di Scienze Matematiche Fisiche e Naturali
Dipartimento di Astronomia

Dottorato di Ricerca in Astronomia
Ciclo XXI (2006-2008)

EoR IN ALTERNATIVE COSMOLOGICAL SCENARIOS

Dottorando:
Daniela Crociani

Relatore:
Chiar.mo Prof. Lauro Moscardini

Coordinatore:
Chiar.mo Prof. Lauro Moscardini

Esame Finale Anno 2009

SCUOLA DI DOTTORATO IN SCIENZE MATEMATICHE, FISICHE E ASTRONOMICHE
SETTORE SCIENTIFICO DISCIPLINARE: AREA 02 - SCIENZE FISICHE
FIS/05 ASTRONOMIA E ASTROFISICA

Introduction

The reionization redshift represents a fundamental milestone in the history of the universe, since at this epoch the first sources of light can ionize the intergalactic medium (IGM) with significant repercussions on the following formation of the structures. As an example, the ultra-violet (UV) radiation can heat the gas, preventing the collapse of the smallest galaxies that can be destroyed by the photoionization. The re-heating of the IGM can also reduce the formation of the molecular hydrogen, that is a fundamental ingredient of the star formation, determining the effectiveness of the hosting source to the IGM ionization.
It is then important to know when the first and the final stages of reionization take place and the way in which this process occurs. Several observational test made up to now to characterize the epoch of reionization (EoR) paint it as a quite complex phenomenon that is at present still unclear. In fact, a first estimate of the reionization redshift z_{reion} can be achieved from the polarization spectrum of the Cosmic Microwave Background (CMB) radiation. The IGM ionization can produce an additional peak on large physical scales, corresponding to the horizon size at the reionization epoch, whose amplitude is related to the IGM optical depth. The recent analysis based on the 5-year WMAP (Komatsu et al., 2008) data shows that $z_{reion} \sim 11$, probing an early reionization. Other estimates come from the observational tests on the large scale structures, as the Lyα galaxies at $z = 5.7$ and 6.5. Their characteristic luminosity function shows a lack of time evolution, that is consistent with a fully ionized IGM at $z_{reion} \sim 6$ (Malhotra & Rhoads, 2004). Similar results have been obtained from the analysis of the spectra of the high-z QSOs (Fan et al., 2004; Goto, 2006; Willott et al., 2007, 2009) and Gamma Ray Bursts (GRB) (Totani et al., 2006). In fact, the typical light-curve of their emission shows a flux decrement corresponding to the Lyα wavelength, in agreement with $z_{reion} = 6.5$. Other observations related to the IGM temperature at $z \lesssim 4$ (Hui & Haiman, 2003) are still consistent with a late reionization redshift, possibly following a first IGM ionization at earlier epochs.
Then, the outlined picture for reionization describes it as an inhomogeneous and not instantaneous process, for which the evolution, the nature and the role of the same ionizing sources are still indetermined. The future observational probes, anyway, can help us to clarify these obscure aspects. The major chance is represented by the next Planck's observations, that are expected to probe the CMB polarization spectrum with high accuracy at the lower multipole moments, so that to infer the IGM optical depth with a precision of $\sim 6\%$ (unlike the present 20% provided by WMAP) (Holder et al., 2003; Mukherjee & Liddle, 2008). As a consequence, these observations should allow to distinguish between different, although simple, reionization models and to constrain the possible extended or instantaneous nature of this process (Bruscoli et al., 2002). Other information can be revealed by the investigations of the new interferometers as LoFAR, SKA, MWA and PAST. The purpose of such researches is to detect the radiation at the 21-cm wavelength emitted by the neutral hydrogen, tracing the IGM ionization history throughout the evolution of the universe. This emission can also be measured as an additional small ($\lesssim 20\mu K$) contribution to the CMB temperature (Ciardi & Madau, 2003; Shapiro et al., 2008). Anyway, the success of this kind of tests is strongly related to the capability of the interferometers to receive signal from the actual reionization redshift. In fact, most of these instruments have been planned to detect the radiation coming from $z \lesssim 9$, then they are in practice ineffective in case of an earlier reionization, but just in giving a lower limit for z_{reion}.
Because of its nature, the reionization process is strictly related to the structure formation scenario. In fact, the ionization action of the galaxies is usually dependent on the properties of the hosting dark matter halos and the recombination of the gas is determined by the local density.

Then, the predicted reionization picture should, in principle, vary when different assumptions concerning the hierarchic evolution of the dark matter perturbation are made. As a consequence, the reionization observables can be used to probe not only the IGM state but also the structure formation paradigm. However, the growth of the density fluctuations is indeed determined by the cosmological background. In fact, the rate at which their amplitude increases is a direct function of the matter and dark energy contents of the universe. Then, as an indirect probe, the observational tests on reionization can constrain also the cosmological framework.
From this point of view, the purpose of this work is to investigate the ability of the reionization observables in constraining the structure formation and the properties of the background universe. In doing this, we have assumed theoretical prescriptions for the hierarchic growth of the density perturbations and suitable models describing the ionization and the recombination of the IGM, making predictions for the evolution of reionization both in the standard ΛCDM universe and in two different chosen alternative cosmologies.
We first assume a universe with a dark energy component varying in time. In fact, although the standard model based on the cosmological constant Λ does not conflict with the recent observations and is widely used in literature, the introduction of Λ implies theoretical problems of various nature, as the fine tuning required to obtain the present-day similar values for the dark matter and the dark energy density (the so-called 'coincidence' problem). Moreover, the last observational test on SNIa (Wood-Vasey et al., 2007) does not reject the possible evolution of the equation of state of the dark energy (the so-called 'quintessence' component). Anyway, the time-evolution of the dark energy density indeed affects the growth of the matter fluctuations and, as a consequence, the distribution of the ionizing source.
The other case we consider in this Thesis is represented by a flat ΛCDM universe characterized by a primordial non-Gaussian overdensity field. In the common picture for inflation, the density fluctuation field rising after the accelerated expansion is assumed to have a Gaussian statistics. Actually, the self-interaction of the scalar field driving inflation can give rise to a tiny deviation, modifying the distribution of the overdensity field and affecting the following hierarchic growth. This scenario is also probed by the observational tests related to the CMB bispectrum, that allow to estimate a small degree of non-Gaussianity (Komatsu et al., 2008), or to the quasar distribution in the Sloan Digital Sky Survey (SDSS) (Slosar et al., 2008).
This Thesis is organized as follows:

1. in Chapter 1, the fundamental bases of the cosmological background used in this Thesis will be reviewed. In particular, we will illustrate the theoretical reasons which lead us to consider alternative universes, focusing our attention on the Peebles & Ratra (2003) and Brax & Martin (2000) models that will be adopted to describe the quintessence component in the present work;

2. in Chapter 2, we will review the structure formation paradigm that allows to infer the statistical properties of the collapsed objects. A particular attention will be turned to the non-Gaussianity case and to the introduction of the Matarrese et al. (2000) formalism which can be adopted to describe the effect of non-Gaussianity on the structure evolution, that will be used in our analysis. We will finally introduce the different types of non-Gaussianity considered for our predictions;

3. Chapter 3 is devoted to a general description of the reionization process, its main stages, the kind of the sources driving the IGM ionization and the observational probes that can constrain the epoch at which the reionization ends;

4. the aim of Chapter 4 is to give a brief overview of the several theoretical models proposed up to now to investigate the ionization history of the universe. Together with a summary description of the approaches widely used in literature that we will not assume, we will present a deeper discussion of the analytic method proposed by Furlanetto et al. (2004a) and the semi-analytic formalisms of Furlanetto & Oh (2005) and Avelino & Liddle (2006), that have been adopted in this Thesis to predict the reionization scenario in alternative cosmologies;

5. in Chapter 5, we will present the reionization picture outlined for a quintessence universe as predicted by the Furlanetto et al. (2004a) and Furlanetto & Oh (2005) theoretical models.

Through these approaches, it is possible to infer the detailed features of the HII regions as their typical radius and the global properties of the reionization, as the ionized filling factor, that will be compared to the ΛCDM universe. These theoretical predictions can be constrained by observations possible in the next future.

6. in Chapter 6, the Avelino & Liddle (2006) model will be applied to a standard universe in which the primordial overdensity field has a non-Gaussian statistics. We will estimate the evolution of the ionized fraction and the optical depth of the IGM, comparing our results to the reionization picture predicted for the standard Gaussian case and discussing the possibility to infer non-Gaussianity through the current WMAP probes;

7. finally, Chapter 7 is dedicated to a brief introduction of the future prospects of this work, from a point of view of the next observations of the interferometers.

Chapter 1

Cosmological background

The aim of this chapter is to review the main foundations of the modern cosmology. At present, the most powerful instrument that allows the investigation of the dynamic and evolution of the universe on large scales is the Einstein's General Relativity (GR hereafter). In this context, gravity is not a real force but the action of matter and energy on the test particles is mediated by the metric tensor g of the 4-dimensional space-time and it is represented by the Einstein equations (Einstein, 1915a,b, 1916) that, using natural units with $c = \hbar = 1$, read as

$$G_{ik} \equiv R_{ik} - \frac{1}{2} g_{ik} R = 8\pi G T_{ik} \ , \tag{1.1}$$

where G_{ik} is the Einstein's tensor, R and R_{ik} are the Ricci scalar and the Ricci tensor respectively, g is the metric tensor describing the space-time geometry and T_{ij} is the energy-momentum tensor representing the matter-energy content. Up to now, Einstein's GR showed itself to be a successful theory in describing many of cosmological aspects and it is nowadays the basis of the cosmological models reviewed in this chapter.

1.1 Basic principles

1.1.1 The Cosmological Principle

The Cosmological Principle asserts that on large scale (i.e. $\geq$ 100 Mpc) the universe is totally homogeneous and isotropic, so that there are neither preferred positions nor directions.
This idea was first proposed in the 1920s by Einstein and other relativistic cosmologists without any observational reason, but only assuming basically a simplicity in the global structure of the universe and in the local behaviour of matter. In this case, the solutions to the field equations of GR leads to relatively simple cosmological models. Afterwards, Bondy, Gold and Hoyle introduced the idea of a Perfect Cosmological Principle, that states the homogeneity and the isotropy of the universe not only in space but also in time. This leads to the development of the steady-state theory, subsequently abandoned toghether with the Perfect Principle itself since unable to easy describe the properties of the CMB, radio sources and the He abundance. Another attempt has been made to justify the cosmological principle on the basis of the last observations of the CMB. In fact, in the standard Big Bang theory two regions sufficiently distant from each other cannot be in causal contact at any time after the origin of the universe. Then, the cosmological principle can explain the homogeneity observed on scales larger than that expected to be in causal contact. Today the Cosmological Principle is assumed since it agrees with basically all of the recent observations, in particular with the isotropy and the (almost perfect) homogeneity of the CMB, demonstrating that the level of anisotropy of the universe is $\sim 10^{-5}$.

1.1.2 The expansion of the universe

Another observational evidence is the expansion of the universe, for which every observer, independently on its location, sees a systematic receeding of the distant galaxies from the Milky Way.

Although in a first moment it could be related to the proper motion of the galaxies, this phenomenon has not a dynamical origin and is caused only by the expansion of space.
This idea is supported by the theoretical approach of GR, since the Einstein's equations provide stationary non-static solutions, and by the observations of distant galaxies made by Edwin Hubble in the 1920's, who measured a systematic redshift in their light spectra.
Hubble noticed that the receeding velocity v of the galaxies is proportional to their distance d as follows:

$$v = H_0 d \ , \tag{1.2}$$

in which H_0 is the so-called Hubble constant (measured at the present day) that, in despite of its name, is not constant but varies with t. Therefore, as pointed out by the Cosmological Principle, every observer in the Universe sees the distant galaxies receeding with the velocity given by Eq. (1.2) so that this statment was called Hubble Law. The parameter H_0 can be measured with observations and, beeing of large use in cosmology and not known exactly, it is conventionally represented by the adimensional parameter $h = H_0/(100 \text{ km/s/Mpc})$.

1.2 The Robertson Walker metrics

The number of the independent Einstein's equations can be reduced if the Cosmological Principle is assumed. In this case, the space-time manifold can be written as the warped product of $\mathbb{R}$ and the metric of the universe assumes a unique form, the Roberston-Walker metric (Robertson, 1933; Walker, 1933; Robertson, 1935), in which the interval ds between two events is given by

$$ds^2 = (dt)^2 - a(t)^2 \left[\frac{dr^2}{1 - Kr^2} + r^2 (d\theta^2 + \sin^2 \theta \mathrm{d}\phi^2) \right] \ , \tag{1.3}$$

where c is the speed of light, $a(t)$ is the parameter related to the expansion of the universe having the dimension of a length, t is the proper time and (r, θ, ϕ) are the polar comoving coordinates, with r dimensionless. The term K represents the curvature parameter of the hypersurface Σ that can assume three possible values:

$K = +1 \implies \Sigma$ is an hyperspherical space and the Universe is closed;
$K = \ 0 \implies \Sigma$ is an Euclidean space and the Universe is flat;
$K = -1 \implies \Sigma$ is and hyperbolic space and the Universe is open.

Eq. (1.3) can be also written as

$$ds^2 = (dt)^2 - a(t)^2 \left[\mathrm{d}f_K(r) + r^2 (d\theta^2 + \sin^2 \theta \mathrm{d}\phi^2) \right], \tag{1.4}$$

where $f_K(r)$ is a function strictly related to the curvature parameter K:

$$f_K(r) = \begin{cases} \sinh^{-1}(r) & \text{if } K = -1 \ , \\ r & \text{if } K = \ \ 0 \ , \\ \sin^{-1}(r) & \text{if } K = +1 \ . \end{cases}$$

Determining the geometry of the space-time is an important aspect since it affects the evolution of the universe and the distribution of the inner structures. As we will see in sect. 1.5, it is strongly dependent on its matter-energy content.

1.2.1 Proper and comoving coordinates

The rod distance between two space-like events in a reference frame in which they are simultaneuos is called the proper distance d_p. Using Eq. (1.4) allows to relate d_p to the expansion of the universe, by setting $dt = 0$ and by integrating along the distance r between them:

$$d_p = a(t) \int_0^r \frac{\mathrm{d}f_K(r')}{\mathrm{d}r'} \mathrm{d}r' = a(t) f_K(r) \ . \tag{1.5}$$

Given its definition, the proper distance has no operational meaning since it is impossible to measure simultaneously all the distance elements that connect the two events. Furthermore, the distance changes with time, since the relation between the proper distances measured at the present time t_0 and at $t < t_0$ is

$$d_p(t_0) = a(t_0) f_K(r) = \frac{a(t_0)}{a(t)} d_p(t) \ . \tag{1.6}$$

The proper distance measured at t_0 is the so-called comoving distance d_c,

$$d_c = a(t_0) f_K(r) \ , \tag{1.7}$$

that is a powerful instrument for defining a reference frame in which the comoving coordinates do not depend on the expansion itself and the position of the objects varies only because of their proper motions. Since $a(t_0)$ will be here assumed to be equal to the unity, physical and comoving coordinates are related by the expansion factor as

$$\boldsymbol{r}(t) = a(t)\boldsymbol{x}(t) \ , \tag{1.8}$$

where $\boldsymbol{r}$ is the proper length and $\boldsymbol{x}$ is the comoving one, with $a(t)$ dimensionless.
Finally, for some applications, it is convenient to define the conformal time as

$$\mathrm{d}\tau \equiv \frac{\mathrm{d}t}{a(t)} \ . \tag{1.9}$$

It is important to stress that from the theoretical point of view, the Hubble law can be obtained directly by the velocity expression in proper coordinates:

$$\boldsymbol{v} = \frac{\mathrm{d}\boldsymbol{r}}{\mathrm{d}t} = \dot{a}(t)\boldsymbol{x}(t) + a(t)\dot{\boldsymbol{x}}(t) \ , \tag{1.10}$$

in which the second term is due to the proper motion and it can be neglected on large scales. Then, defining $H(t) \equiv \dot{a}(t)/a(t)$, we return to the Hubble law $\boldsymbol{v} = H(t)\boldsymbol{r}(t)$.

1.2.2 The Redshift

In order to describe the receding motion of the galaxies caused by the expansion of the universe it has been introduced a parameter called redshift, directly measurable with the observations, that relates the wavelenghts of the observed and the emitted radiations, λ_e and λ_0 respectively, as follows:

$$z = \frac{\lambda_0 - \lambda_e}{\lambda_e} \ . \tag{1.11}$$

It is possible to demonstrate that this parameter is directly related to the expansion factor. In fact fixing t_e and t_0 as the times at which a first photon is emitted by a galaxy at distance r and then received by the observed, and $t_e + \delta t_e$ the time of the emission of a second photons, received by the observer at $t_0 + \delta t_0$, from Eq. (1.3) we can write

$$\int_{t_e}^{t_0} c\frac{\mathrm{d}t}{a(t)} = f_K(r) = \int_{t_e+\delta t_e}^{t_0+\delta t_0} \frac{\mathrm{d}t}{a(t)} \ , \tag{1.12}$$

because their comoving distance does not change. Then, assuming that δt_0 and δt_e are small, from the comparison between the left and right members of Eq. (1.12) we obtain $\delta t_0/a(t_0) = \delta t_e/a(t_e)$ or analogously $a(t_e)/\lambda_e = a(t_0)/\lambda_0$ that leads to $1 + z = a(t_0)/a(t_e)$. Then the redshift parameter at a given time t in which the light has departed reads as

$$1 + z = \frac{a(t_0)}{a(t)} \tag{1.13}$$

and the relation between proper and comoving distances becomes

$$d_p = \frac{d_c}{1+z} \ . \tag{1.14}$$

1.3 Cosmological Models

1.3.1 The Friedmann Models

The development of all modern cosmology is based on the GR. In order to be able to solve the Einstein's equations it is necessary to know the matter-energy content of the universe, that is usually assumed to be a perfect fluid, represented by the stress-energy tensor T

$$T_{ij} = -pg_{ij} + (p+\rho)U_iU_j \ , \tag{1.15}$$

where ρ is the density, p is the pressure and U is the 4-dimension velocity field of the fluid, normalized such that $g_{ij}U_iU_j = -1$. The velocity field has no spatial component and is parallel to the time direction. Introducing the RW metric and Eq. (1.15) in Einstein's equations (1.1), we derive two different equations for the expansion of the universe:

$$\ddot{a} = -\frac{4\pi}{3}G\Big(\rho + 3p\Big)a \tag{1.16}$$

for the time-component ($i = j = 0$), and

$$\dot{a}^2 + K = \frac{8\pi}{3}G\rho a^2 \tag{1.17}$$

for the space-space component ($i, j = 1, 2, 3$), while the space-time component would lead to the unuseful identity 0=0. These last two equations are the Friedmann-Roberston-Walker (FRW) equations, that are not independent to each other, since the second one can be obtained by the first one simply assuming the adiabaticity of the expansion of the Universe:

$$\mathrm{d}(\rho a^3) = -3pa^2\mathrm{d}a \ . \tag{1.18}$$

A combination of these three equations can lead to

$$\left(\frac{\dot{a}^2}{a_0}\right) - \frac{8\pi}{3}G\rho\left(\frac{a}{a_0}\right)^2 = -\frac{K}{a_0} \ , \tag{1.19}$$

that, once integrated, allows to obtain $a(t)$. The simplest solution of Eq. (1.16) and (1.17) is represented by the Friedmann models, that describe the content of matter-energy of the universe as a fluid with equation of state:

$$p = w\rho \ , \tag{1.20}$$

where w is generally a time-dependent paramenter and depends on which kind of component is considered.

1.4 The components of the universe

1.4.1 Matter and Radiation

Inserting the equation of state in Eq. (1.18) and integrating allows to obtain

$$\rho(z) = \rho_0 \exp\left[-3\int_1^a (1+w(z))\frac{\mathrm{d}a(z)}{a(z)}\right] \ , \tag{1.21}$$

which represents the time-evolution of the density of the given component characterized by the w parameter.
One of the constituent of the cosmic fluid is radiation, i.e. a fluid of non-degenerate, ultrarelativistic particles in thermal equilibrium. Its equation of state is characterized by $w = 1/3$ that determines the evolution of its density $\rho_r(z) = \rho_{0,r}a^{-4}$, where the subscript 0 represents the corresponding value at the present time t_0. Since its energy spectrum can be described by that of a thermal black body whose temperature T is related to the density as

$$\rho_r = \frac{\pi^2 k_B^4}{15}T_r^4 \ , \tag{1.22}$$

in which k_B is the Boltzmann constant. From this relation it follows that $T_r = T_{0,r}a^{-1}$.
Nowadays, the recent observations agrees in asserting that the most predominant component of the universe is dark matter (DM hencefor), a fluid not coupled with photons and affected only by the gravity action. Also, it is accepted that DM is cold, i.e. its mean thermal energy is negligible when compared to the rest mass energy of the constituent particles before decoupling from radiation. As a consequence its pressure is negligible with respect the energy density, that implies $w = 0$. This property is shared also by the baryonic, luminous matter, since for a perfect gas of particle of mass m, $w = k_BT/mc^2 \simeq 0$. The evolution of the density of the matter, resulting by inserting $w = 0$ in Eq. (1.21), is $\rho_m(z) = \rho_{0,m}a^{-3}$. From the difference between the evolution of the matter and the density component, given their present values, it is evident that it must exist a given time such that $\rho_r = \rho_m$. This epoch is the so called equivalence epoch and is characterized by $a_{eq} = \rho_{0,r}/\rho_{0,m}$.

1.4.2 Dark Energy

At present, the observational evidences agree with a model of expanding universe ($\dot{a}(t_0) > 0$) that is accelerating ($\ddot{a}(t_0) > 0$). Then, from Eq. (1.16) it is obviuos that $p_0 < -c^2\rho_0/3$, implying that the dominant component of the cosmic fluid has $w < -1/3$. As a consequence its pressure is negative, meaning that the nature of the dominating component, responsible for the expansion of the universe, today should differ by any kind of non-relativistic matter or radiation. Moreover, its role in the structure formation is still debated. In fact, some recent theories do not reject its possible coupling with DM. It is commonly called dark energy (DE hereafter), but actually its nature is unknown and in the following subsections we will briefly describe the main theoretical models proposed to describe its effects on the dynamic of the universe.

The cosmological constant

Probably the most used way to model the effects of DE in the universe is the introduction of the cosmological constant. This concept rises from the first common accepted idea that the universe should be stable and static, that matematically translates in $\ddot{a} = 0$ and, as already mentioned in the previous paragraph, this reflects in the immediate consequence of a negative pressure for the dominant component. Then, to avoid what seemed an innatural conjecture, Einstein introduced the cosmological constant Λ in his equations:

$$R_{ij} - \frac{1}{2}g_{ij}R - \Lambda g_{ij} = -8\pi G T_{ij} \ , \tag{1.23}$$

that allows static solutions when suitable values of Λ are assumed. These models are called the Einstein universes and can be obtained by the Friedmann's equations substituting in Eq. (1.16) and (1.17) the effective pressure and density

$$\tilde{p} = p - \frac{\Lambda}{8\pi G} \tag{1.24}$$

$$\tilde{\rho} = \rho + \frac{\Lambda}{8\pi G} \ . \tag{1.25}$$

However, after the discover of the expansion of the universe, the static solutions lost their validity and as a consequence the use of Λ to produce static solutions has been abandoned. It is after the later observations of the acceleration of the universe that the interest in the cosmological constant has been renewed and today it is used to represents the DE component. The parameter Λ is directly related to its density:

$$\Lambda = 8\pi G\rho_\Lambda \tag{1.26}$$

and corresponds to a fluid with a constant $w = -1$ in the equation of state.
Anyway, the introduction of the cosmological model gives rise to some theoretical problems. The first is the so called 'cosmic coincidence problem', that consists in the similarity of the density of DM and DE today, namely $\Omega_{m,0} \sim 0.3$ and $\Omega_{\Lambda,0} \sim 0.7$ (see the next section for the definition of the last two parameters). Since actually we are not in a special epoch and these two components should have a quite different cosmological evolution, the similar values of $\Omega_{m,0}$ and Ω_Λ require a strong fine-tuning in the initial conditions (IC) of their evolution.

The other main problem related to the cosmological constant is its actual low value, i.e. $\Lambda < 10^{-55}\mathrm{cm}^{-2}$. This corresponds to a mass $m_\Lambda = (|\Lambda|/(8\pi G))^{1/4} < 10^{-32}$ eV that is much smaller of the electron mass $m_e = 5.11 \times 10^5$ eV. But, despite its low value, this quantity plays a crucial role in the gravity of the universe, that is possible only assuming the strong fine-tuning in the IC.
To avoid these problems, nowadays the recent theoretical models associated the DE component to a form of energy evolving in time, the so called quintessence, that is not in conflict by the last observations probed by the SNIa.

Quintessence

The quintessence is one of the proposed solutions to the theoretical problems produced by the cosmological constant. In this picture, the DE is associated to the energy density of a scalar field Φ, that can be represented by a spinless particle with no charge coupled only to gravity (and at best weakly coupled to the baryonic matter, otherwise it would allow the existence of a "fifth force" that is not actually observed). In general, this field can depend on the spatial position and time and its evolution is determined by its self-interacting potential $V(\Phi)$, shallow enough that the energy density decreases with the expansion of the universe more slowly than that of the matter. The evolution of the scalar field in GR is described by the Lagrangian

$$\mathcal{L} = \frac{1}{2} g^{ik} \Phi_{,i} \Phi_{,k} - V(\Phi) \tag{1.27}$$

where the notation $,i$ represents the coordinate derivation. In a comoving coordinate system with the diagonal metric $\{c^2, -a^2, -a^2, -a^2\}$, the equations of Eulero-Lagrange

$$\partial_\mu \left[\frac{\partial(\mathcal{L}a^3)}{\partial(\partial_\mu \Phi)} \right] - \frac{\partial(\mathcal{L}a^3)}{\partial \Phi} = 0 \tag{1.28}$$

provide the equation of the evolution of the field, the so called Klein-Gordon equation:

$$\ddot{\Phi} + 3H(z)\dot{\Phi} + \frac{\mathrm{d}V}{\mathrm{d}\Phi} = 0 \ , \tag{1.29}$$

in which the term $\nabla^2\Phi/a^2$ has been neglected since we consider only the homogeneous part of the scalar field and, moreover, the expansion of the universe would make it null rapidly. In this equation, the first term represents the inertial term of the motion, while the second one is the friction produced by the expansion of the universe and the third one is related to the action of the potential.
From Eq. (1.27) it is possible to determine the density and the pressure associated to the scalar field

$$\rho_\Phi = \frac{\dot{\Phi}^2}{2} + V(\Phi) \tag{1.30}$$

$$p_\Phi = \frac{\dot{\Phi}^2}{2} - V(\Phi), \tag{1.31}$$

and the w parameter, that rises directly from the equation of state:

$$w = \frac{\dot{\Phi}^2 - 2V(\Phi)}{\dot{\Phi}^2 + 2V(\Phi)} \ . \tag{1.32}$$

From the last equation, it is evident that the detailed behaviour of the equation of state is strictly related to the shape of the potential and the possible evolution in time of the scalar field. In case of a quintessence component, the w parameter can vary with time, reducing to values smaller than $-1/3$ at present time, in order to allow the accelerated expansion of the universe observed today. Then, in general way the density of the quintessence can be written as $\rho_\Phi(z) = \rho_{0,\Phi} a^{-3(1+w)}$, with $w = w(z)$. A particular case rises up when the scalar field evolves slowly in time, so that $\dot{\Phi}^2 \ll V(\Phi)$ today. In fact, in this case we would obtain $w \sim -1$, i.e. the energy density approximates the effect of the cosmological constant.
Finally, we briefly review the main characteristics of a quintessence field:

1. although assumed homogeneous, the distribution of the quintessence field is not prefectly uniform. Writing $\Phi(\vec{x},t) = \Phi_0(\vec{x}) + \delta\Phi(\vec{x},t)$, in which the first term represents the spacially uniform part and the second one the deviations from it, the equation of Steinhardt & Caldwell (1998) allows to achieve the evolution of the fluctations

$$\delta\Phi_k^{''} + 2aH\delta\Phi_k^{'} + \left(k^2 + a^2\frac{\partial^2 V}{\partial\Phi^2}\right)\delta\Phi_k = -\frac{1}{2}h_k^{'}\Phi_0^{'} \tag{1.33}$$

   where h is the trace of the metric of syncronous gauge perturbation and the derivation is made with respect to the conformal time τ;

2. given the evolution of the w parameter of the equation of state, it is always possible to achieve the shape of its producing potential;

3. not all the potential in literature produce small parameters of mass. Some quintessence models, as those reviewed in 1.6, involve energy parameters for the scalar field comparable to the energy scales of the particle physics (> 1 Gev);

4. the quintessence field does not produce strong effects on the observable quantities. For example, the power spectra of the matter density and the CMB can be modified, but not in a catastrophic way;

5. not all the potentials are sensitive to the IC. This is the true power of some scalar field modelling, since it permits to avoid the fine tuning problem related to the cosmological constant. These alternative cosmologies produce an evolution at low z for the scalar field that does not depend on the IC and, for this reason, they have tracking properties;

6. the quintessence cosmologies are independent of the IC on $\delta\Phi$.

1.5 Cosmological parameters

Let us define the critical density of the universe at a generic instant as the matter-energy density for which the spatial curvature of the universe vanishes:

$$\rho_c(t) = \frac{3H(t)^2}{8\pi G}\ , \tag{1.34}$$

that for $t = t_0$ can be written as $\rho_{c,0} = 1.87 \times 10^{-29} h^2$ gr cm^{-3} and is directly related to the geometrical structure of the universe. In fact substituting in Eq. (1.19), we obtain

$$H_0^2\left(1 - \frac{\rho_0}{\rho_{c,0}}\right) = -\frac{K}{a_0^2}\ . \tag{1.35}$$

Since the critical density sets a preferred matter-energy content in the universe, its value is used as a reference for the other densities, then the density parameter of a given i-th component at a given cosmological epoch is

$$\Omega_i(t) = \frac{\rho_i(t)}{\rho_c(t)} = \frac{8\pi G\rho_i(t)}{3H(t)^2}\ . \tag{1.36}$$

Including the use of the Hubble and the density parameters in the Eq. (1.17), it results

$$H^2 = H_0^2\left[\Omega_{r,0}a^{-4} + \Omega_{m,0}a^{-3} + \Omega_{\Lambda,0}\exp\left(-3\int_1^a(1+w)\frac{\mathrm{d}a}{a}\right) - \Omega_{K,0}a^{-2}\right] \tag{1.37}$$

where the term Ω_K is the density parameter related to the spatial curvature, that can be included as a source of gravity and corresponds to $\Omega_{K,0} = K/H_0^2$. When evaluated at present, Eq. (1.37) becomes

$$(\Omega_{r,0} + \Omega_{m,0} + \Omega_{\Lambda,0}) - \Omega_{K,0} = \Omega_0 - \Omega_{K,0} = 1 \tag{1.38}$$

where Ω_0 is the total density parameter for the matter-energy content of the universe. As results from the above equation, the geometry of the universe is strongly dependent on it, in fact, positive

values for Ω_0 leads to a positive curvature ($K = +1$) and viceversa. The case $\Omega_0 = 1$ implies a null curvature ($K = 0$), that means a flat universe, and the Eq. (1.37) becomes

$$H^2 = H_0^2 \left[\Omega_{r,0} a^{-4} + \Omega_{m,0} a^{-3} + (1 - \Omega_{r,0} - \Omega_{m,0}) \exp\left(-3 \int_1^a (1+w) \frac{\mathrm{d}a}{a} \right) \right] . \tag{1.39}$$

Finally, we also introduce the deceleration parameter, defined as

$$q \equiv \frac{\ddot{a}a}{\dot{a}^2} \tag{1.40}$$

that describes the acceleration status of the universe. If the universe is accelerating, its value is negative and the contrary is true for positive values.
With the introduction of the cosmological parameters, the expansion factor at the equivalence takes a suitable form $a_{eq} = (4.47 \times 10^{-7} K^{-4}) T_{r,0}^4 \Omega_{m,0}^{-1} h^{-2}$.

1.6 Alternative cosmological scenarios

1.6.1 'Tracking' quintessence fields

A class of fields that can be considered as good candidates to solve the theoretical problems introduced by the cosmological constant are the so called tracker-fields. As already mentioned, their peculiarity is that starting from a wide range of ICs for Φ and $\dot{\Phi}$, the solution to the Klein-Gordon equation assumes always the same shape at low z, that behaves like an attractor and for this reason it is said to have tracker properties. Then, in these models the amount of the DE density today becomes naturally that observed, avoiding the fine-tuning problem. In order for a given potential to produce tracker solutions of the Klein-Gordon equations, the parameter Γ defined as

$$\Gamma \equiv \frac{V' V''}{V'^2} , \tag{1.41}$$

has to satisfy the following conditions, setting w_B and w are the w parameter for the background and for the quintessence field respectively:

1. if $w < w_B$, then $\Gamma > 1$ and must be almost constant, i.e. $|\mathrm{d}(\Gamma - 1)/(H\mathrm{d}t)| \ll |\Gamma - 1|$. This is the most interesting case, since today $w < 0$;

2. if $w_B < w < (1 + w_B)/2$, then $1 - (1 - w_B)/(6 + 2w_B) < \Gamma < 1$ and must be almost constant. Although this condition cannot be valid for all the life-time of the universe, since it would be rejected by the structure formation paradigm, some hybrid models of quintessence could allow for an initial phase in which $w_B < w$ that finishes at the beginning of the matter era, in order to agree with the observations.

From the first point, it is evident that the equation of state of the quintessence varies following that of the background. In fact, $w \leq 1/3$ in the radiative era and approaches to negative values as the universe becomes matter-dominated. At this epoch, the energy-density of the quintessence fiels decreases more slowly than that of the matter, and dominates the gravity in the last phases, when $w \sim -1$.
In the vast majority of the quintessence potentials proposed in literature, those that vary as an inverse power law have the tracking property and also admit scaling solutions, e.g. Φ is a power law of the expansion parameter a. Assuming a FRW flat universe with a quintessence field minimally coupled with the gravity and a constant w_B in time for the cosmic fluid, so that $\rho_B = \rho_{0,B}(a/a_0)^{-3(1+w_B)}$, searching for scaling solution is equivalent to set $\rho_\Phi = \rho_{0,\Phi}(a/a_0)^{-n}$ and, assumed a constant w, Eq. (1.18) implies

$$P_\Phi = \Big(\frac{n}{3} - 1 \Big) \rho_\Phi . \tag{1.42}$$

Then, Eq. (1.30) leads to

$$\dot{\Phi} = \frac{n}{3}\rho \tag{1.43}$$

$$V = \Big(1 - \frac{n}{6}\Big)\rho \tag{1.44}$$

and, through straightforward calculation, inserting the above relations in Eq. (1.17), the second FRW equation can be written as

$$\frac{\mathrm{d}\Phi}{\mathrm{d}x} = \frac{A}{x\sqrt{1 + B^2 x^{n-3(1+w_B)}}} \ , \tag{1.45}$$

where $x = a, A = \sqrt{n/8\pi/G}$ and $B = \sqrt{\rho_{0,B}/\rho_{0,\Phi}}$. This differential equation can be easily integrated if $n = 3(1 + w_B)$, producing an exponential potential, but in this case the energy-density would evolve as that of the background and it does not agree with the standard picture for the structure formation, in which the quintessence component should be negligible at earlier epoches in order to allow the hierarchic growth of matter fluctuations. Then we consider only the case $n \neq 3(1 + w_B)$, in which the integration of the Eq. (1.45) leads to

$$\begin{aligned}\Phi = \Phi_0 + \frac{2A}{[3(1 + w_B) - n]} \times \\ \ln\left[\sqrt{1 + [B^{-1}x^{(3(1+w_B)-n)/2]^2}} + B^{-1}x^{(3(1+w_B)-n)/2}\right] \ .\end{aligned} \tag{1.46}$$

In case of a dominant component of background ($B \gg 1$), the resulting potential from equations (1.44) and (1.43) is

$$V(\Phi) = \Big(1 - \frac{n}{6}\Big)\rho_{0,\Phi}\left(\frac{3(1 + w_B) - n}{2A}B\right)^{-2n/(3(1+w_B)-n)} (\Phi - \Phi_0)^{-2n/(3(1+w_B)-n)} \ . \tag{1.47}$$

and, as expected, is a inverse power law potential potential, usually written as

$$V(\Phi) = \frac{M^{\alpha+4}}{\Phi^\alpha} \ , \tag{1.48}$$

where M is a constant with the dimension of energy and $\alpha = 2n[3(1+w_B)-n]$. The corresponding value of the w parameter is

$$w = \Big(\frac{n}{3} - 1\Big) = \frac{\alpha w_B - 2}{\alpha + 2} \ , \tag{1.49}$$

so that when the universe is radiation-dominated, $w = (\alpha/3 - 2)/(\alpha + 2)$ and becomes $w = -2/(\alpha + 2)$ in the matter era. Since the behaviour of V does not depend on the IC, the different solutions of the Klein-Gordon equation will converge to the scaling solution. Then, this potential has tracking properties. Actually, the IC could affect the approximation $B \gg 1$, producing a possible upper limit to the energy-density of Φ.

1.6.2 The Peebles & Ratra (2003) potential

Ratra & Peebles (1988), and later Peebles & Ratra (2003) (RP hereafter), are the first to propose a similar kind of potential as in Eq. (1.48). In the theory of the gauge supersymmetries (SUSY), these kinds of potential are naturally generated at energies $E \leq M$, due to non-perturbative effects along float directions of the of the scalar potential. Anyway, they are based on the Kähler function, that depends on some hypotheses suitable for energy values of the field higher than M, but at smaller scales has to be verified, in order to not destroy the tracking properties. Other models based, on quantistic corrections or space-time curvature, do not suffer of this limitation.
Assuming a negligible energy-density of the quintessence with respect the background at the primordial epochs, and knowing that $a \propto t^q$ with $q = 2/3, 1/2$ in case of matter or radiation dominanting component, respectively, the Klein-Gordon equation becomes

$$\ddot{\Phi} + \frac{3q}{t}\dot{\Phi} - \frac{\alpha M^{\alpha+4}}{\Phi^{1+\alpha}} = 0 \ , \tag{1.50}$$

whose solutions have the shape $\Phi \propto t^p$, where $p = 2/(2+\alpha)$. Given the total energy density of the field $\rho_\Phi = \dot{\Phi}^2 + V(\Phi)$, from equations (1.44) and (1.48) it follows that

$$\rho_\Phi \propto t^{2(p-1)} = t^{-2\alpha/(2+\alpha)} \ , \tag{1.51}$$

in which is evident the slower decreases of the energy-density of the field with respect the background. In fact, since the background-density is $\rho_B \propto t^{-2}$, their rate $\rho_\Phi/\rho_B \propto t^{4/(\alpha+2)}$ shows that for $\alpha > -2$ the energy-density of the field is negligible in the early cosmological epoches, becoming higher and higher as the time increases. Then, at the beginning, the field is small enough to allow the growth of the DM halos and sufficiently large to give rise the accelerated expansion of the universe at the end. Once the quintessence field dominates the gravity, the shape of the potential is not valid anymore, as we will discuss in the next subsection, and the scalar field slows down reducing $w \sim -1$, with $w(z=0)$ strongly dependent on α and $\Omega_{\Phi,0}$. As a general property, given the density for the field, this value is near -1 for small value of α.
This potential allows to avoid the two main problems related to the cosmological constant, since the behaviour of the solution at low z is the same for a wide range of the initial density energy (10^{-37} GeV^4 $< \rho_\Phi <$ $10^6$1 GeV^4). In fact, from the definition of the density energy we have $V'' \sim \rho_\Phi/\Phi^2$, in which the kinetic term is small enough to be neglected (the same expression can be obtained by the FRW equations). In the tracking regime,

$$\frac{\mathrm{d}^2 V(\Phi)}{\mathrm{d}\Phi^2} = \frac{9}{2}\frac{\alpha+1}{\alpha}(1-w^2)H^2 \ , \tag{1.52}$$

that combined to the previuos equation allows energy scales for the quintessence of the order of the Planck energy. Then, since the observations imply $\Omega_{\Phi,0} \sim \Omega_{m,0}$, M is such that $V(\Phi \sim M_{PL} \approx \rho_m)$, from which it results $M = (\rho_m M_{PL}^\alpha)^{1/(\alpha+4)}$ that, for $\alpha > 2$, is of the order of 1 GeV, comparable to the actual energy scales of the particle physics.

1.6.3 The Brax & Martin (2000) potential

As already mentioned in the previous subsection, when the quintessence is dominating, the shape of the Peebles & Ratra (2003) potential has to be correct, since at $z \sim 0$ the energy scale associated to the field is comparable to M_{PL} and the corrections due to the supergravity (SUGRA) must be brought. In these models, the SUSY theory is naturally modified with the introduction of the gravity, whose contribution is important at $E \leq M_{PL}$.
The scalar potential is here produced at the breaking of the symmetry between the gravity and the other forces, and its shape is related to the way in which it happens, as an example

$$V(\Phi) = \frac{M^{\alpha+4}}{\Phi^\alpha} \exp\left(\frac{k}{2}\Phi^2\right) \ , \tag{1.53}$$

where $k = 8\pi G$. The left factor is derived by the SUSY theories, while the second one is the SUGRA correction in terms of Φ/M_{PL}. The parameters M and α are the same than in the SUSY theories and under the assumption that the symmetry is broken for energy scales larger than the electroweak unification (namely, 10^2 GeV), $\alpha \leq 11$. The behaviour of the potential at earlier cosmological epochs is determined by the small ($\ll 1$) value of Φ/M_{PL}, so that V reduces to the RP power law. At late times, $\Phi \approx M_{PL}$ the exponential correction becomes important, and w parameter approaches -1, independently of α, so that also the fine-tuning on its value is avoided.

The behaviour of the equations of state for the RP and SUGRA potentials assuming a cosmological framework consistent to that proposed by the 5-year data of the Wilkinson Microwave Anysotropy Probe (WMAP) mission (see the next section for details) is illustrated in Fig. 1.1. Though the RP and SUGRA models display similar values for w today, strong differences appear at high redshifts. Parametrizing the evolution of w in terms of the expansion factor a as $w(a) = w_0 + w_a(1-a)$, we find that the RP and SUGRA models can be fitted by $w_a \sim 0.08$ and 0.55 respectively, that are still consistent with the present observational constraints. For example, Liddle et al. (2006) combining data from CMB, SNIa and baryonic acoustic oscillations found $w_a = 0.0 \pm 0.8$.
Part of the work on this Thesis will be focused on the RP and SUGRA models. Our choice is

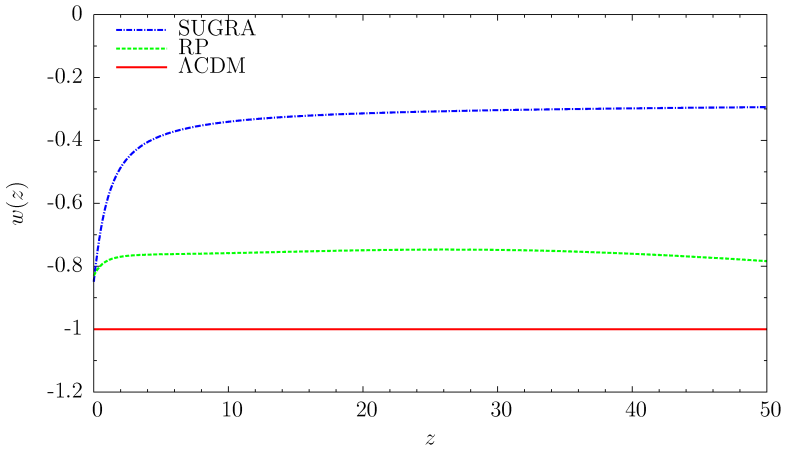

Figure 1.1: Redshift evolution of the cosmic equation-of-state parameter w. Different lines refer to ΛCDM model (red solid line), RP model (green dashed line) and SUGRA model (blue dotted-dashed line).

motivated by their physical foundations on the theory of the particles and by their characteristic tracking property, that allows us to solve the theoretical problems introduced by the cosmological constant.

1.7 The current status of the observations

Many observational test of different nature can be made in order to constrain the cosmological parameters responsible for the geometry and the evolution of the universe. The most important data set comes from the 5-year of the Cosmic Microwave Background (CMB) investigations performed by the WMAP mission, measuring the anisotropies in its temperature (TT) and polarization (EE) spectra. Anyway, the analysis of the CMB temperature power spectrum suffers of degeneracies, since different sets of cosmological parameters can rise approximatively the same spectrum of the anisotropies. Then, a more extended analysis is needed, combining this test to other types of investigation. As an example, the CMB data can be associated to the observations of the Hubble Space telescope (HST) Key Project, providing an estimate $H_0 = 72 \pm 8$ km/s/Mpc in agreement with the predictions for the WMAP data alone, $H_0 = 71.9^{+2.6}_{-2.7}$ km/s/Mpc. It also agrees with most of the values estimated by the other cosmological probes as lensed systems, SZ and X-ray observations, Cepheids distances to nearby galaxies, etc..

For that concerning the distribution of the components of the universe, as shown in Fig. 1.2 the cosmological scenario predicted by WMAP provides the DM parameter $\Omega_{m,0} = 0.258 \pm 0.030$, while $T_{r,0} = 2.726$ K, corresponding to $|Omega_{r,0} \sim 4.7 \times 10^{-5}$ that is indeed negligible with respect to the matter contribution. A consistent result is obtained by the study of the galaxy clusters, that probe the mass distribution on the large physical scales, through which the amount of matter can be constrained as $\Omega_{m,0} = 0.27^{+0.06}_{-0.05}$ (Mantz et al., 2008).
The amount of baryon of the universe is estimated by WMAP as $\Omega_{0,b}h = 0.02273 \pm 0.00062$, in agreement with the last predictions of Steigman (2007) concerning the single abundance of Deuterium and those of ^{3}He and Li (O'Meara et al., 2006; Charbonnel & Primas, 2005), derived by the standard theory of the Big Bang Nucleosynthesis. Anyway, further and detailed investigations are required, since the ^{4}He abundance extrapolated by the globular clusters observations is smaller of that involved by the Y_p parameter measured by WMAP, namely $Y_P = 0.24 \pm 0.006$.

Together with the CMB investigations, other methods of investigation as the strong lensing by the quasar could probe the cosmology of the universe, given the correlation between their abundance and the DE density. Oguri et al. (2008), analysing the large statistical sample of the SDSS, find $\Omega_\Lambda = 0.74^{+0.11}_{-0.15}$, in agreement with the WMAP measurement $\Omega_{\Lambda,0} = 0,742 \pm 0.030$ shown in Fig

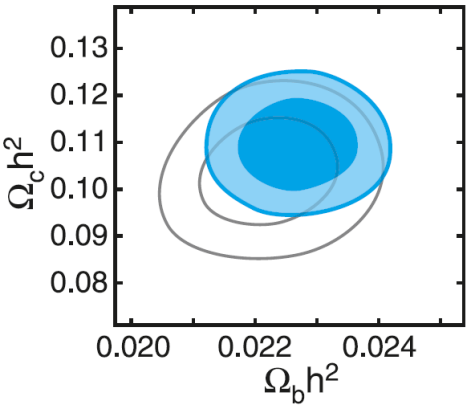

Figure 1.2: Constraints on the dark Ω_c and baryonic Ω_b matter densities (blue) from the 5-year WMAP data release at 68% and 95% limits (Dunkley et al., 2008). Parameters are consistent with the 3-year limits (grey) from Spergel et al. (2007).

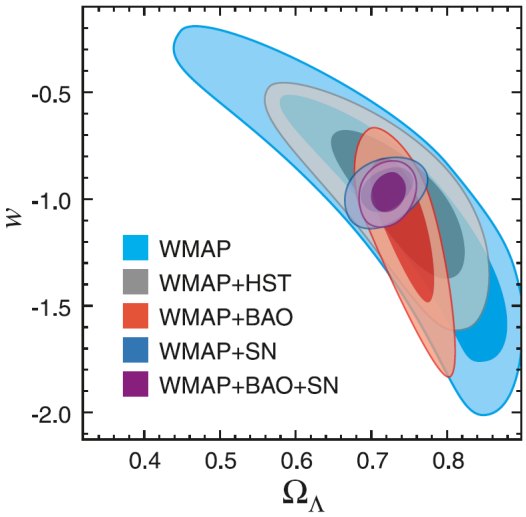

Figure 1.3: Constraints on the time-independent (constant) DE equation of state parameter, w, and the present-day DE density, Ω_Λ, assuming a flat universe. The contours show the 68% and 95% CL. The WMAP-only constraint (light blue) is compared with WMAP+HST (gray), WMAP+BAO (red), WMAP+SN (dark blue), and WMAP+BAO+SN (purple) (Komatsu et al., 2008).

1.3, but however this kind of investigations require a consistent description of the mass distribution and the baryonic physics in order to test cosmology correctly.

Finally, WMAP mission is able to constrain the time-evolution of the w parameter for the DE component. Currently, although the stronger constraints on the presence of DE come from the distance information, other useful methods (as the estimate of the expansion rate of the universe at $z \gtrsim 0.5$, the Integrated Sachs Wolfe effect and the effect of the DE on the growth of structures at low z) could be helpful in the investigation of the DE nature. But at the moment, the current data set are not able to distinguish between the effects of the DE and the space curvature, then a degeneracy affects the estimates. Assumming a flat universe, the current WMAP data set alone is not able to put strong constraints on the determination of the w parameter, as shown in Fig. 1.4. Instead, the data on the SNIa could break the degeneracy between the DE parameter and the present day DE density, obtaining $-0.098 < 1 + w < 0.159$ at 95% confidence level and a similar result is obtained also considering the baryonic acustic oscillations (BAO). If a constant equation of state is assumed (but not a flat universe), as shown in Fig. 1.4 the WMAP data should be coupled

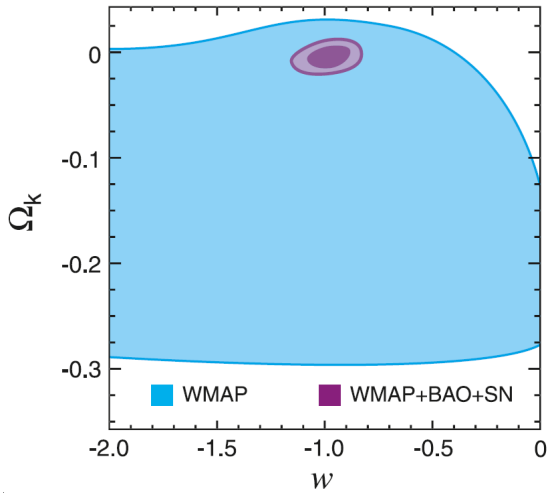

Figure 1.4: Joint two-dimensional marginalized constraint on the time-independent (constant) DE equation of state parameter, w, and the curvature parameter K. The contours show the 68% and 95% CL. The WMAP-only constraints (light blue; 95% CL) are compared with WMAP+BAO+SN (purple; 68% and 95% CL) (Komatsu et al., 2008).

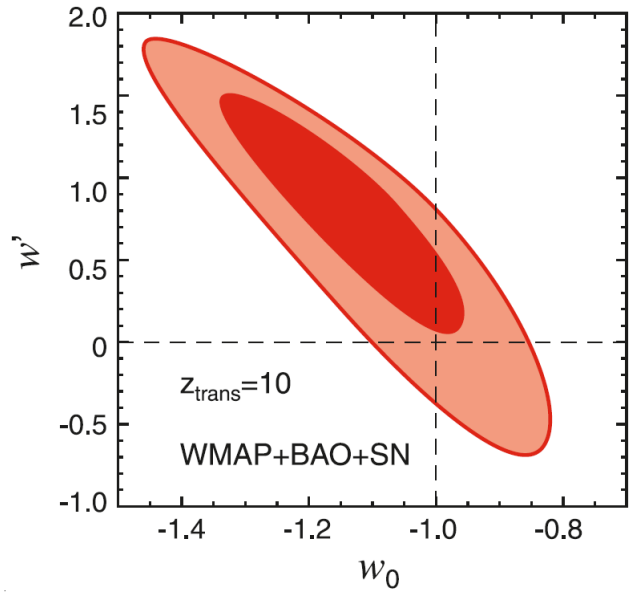

Figure 1.5: Constraints on models of time-dependent DE equation of state, $w(z)$, derived from the WMAP distance priors combined with the BAO and SN distance data. The parameter w_0 represents the value of w at the present epoch, while w' corresponds to $\mathrm{d}w/\mathrm{d}z$ estimated at $z = 0$. z_{trans} is the transition redshift above which $w(z)$ approaches -1. Here, a flat geometry and $z_{\mathrm{trans}} = 10$ are assumed, although the constraints are similar for the other values of z_{trans}. The contours show the 68.3% and 95.4% CL (Komatsu et al., 2008).

to those of the BAO to put meaningful constrains on the curvature of the universe at $\sim 1\%$ of level, allowing $-0.0175 < \Omega_K < 0.085$ and $-0.11 < 1 + w < 0.14$ at 95% CL. On the other hand, CMB is sensitive to the distance to the decoupling epoch via the locations of peaks and troughs of the acoustic oscillations, which can be measured precisely. These results are in agreement with a flat universe in which the w parameter is ~ -1.

Moreover, the WMAP data allow to constrain a possible time-dependence of the w parameter, as illustrated in Fig. 1.5, for which the present-day value of w results $-0.33 < 1 + w_0 < 0.21$ at 95%

CL if the redshift at which w approaches -1 is $z_{\rm trans} = 10$.
In this Thesis, we will assume a cosmological framework consistent with the WMAP data for the 1-year (Spergel et al., 2003) and the 5-year of investigation, however the cosmic scenario predicted by the two releases is similar and cannot affect the conclusions of this work.

Chapter 2

The formation of the cosmic structures

In this chapter, the theoretical scenario for the formation of the cosmic structures, their evolution and the statistical properties useful to this Thesis work will be reviewed. In order for the theoretical modeling of the cosmological framework to allow a description of the formation of the structures observed today, an extension describing the hystory of the collapsed objects is required. The best theoretical improvement proposed up to know is represented by the inflationary picture, consisting in an early accelerated exponential expansion of the universe driven by a scalar field, analogous to the quintessence. This possibility was first introduced by Guth (1981) and then developed by Linde (1982a,b); Albrecht & Steinhardt (1982); Linde (1983) and offers several theoretical advantages. In fact, it could not only represent a reasonable answer to the classical limits of the standard cosmological model based on Big Bang as the horizon problem, but also provides a mechanism that allows the formation of small density fluctuations in the matter-energy content of the universe. According to this scenario, the accelerated expansion is responsible for the amplification of the overdensity field and, in the post-end phase of inflation, the DM overdensity field grows by its self-gravity, detaching itself from the background evolution and collapsing on its own to become a DM halo. On the other hand, the destiny of the baryonic matter is a bit different, due to its coupling to the radiation field before the recombination era. In fact, only after this epoch, the gas is free to fall in the potential wells produced by the DM gravity, allowing the formation of the galaxies observed today.

2.1 Linear Evolution

2.1.1 The Jeans instability

The two main elements determining the evolution of the perturbation are gravity, produced by the matter-content of the perturbations, that makes the fluid collapsed, and the random walks of the particles due to their temperature, responsible for the escape of the particles from the potential wells. In a spherical region of radius λ and mass M with a inner tiny overdense perturbation $\delta\rho$ (with respect to the mean density of the universe ρ_B), the collapse is possible if the gravity force exceeds the pressure, i.e.

$$F_g \simeq \frac{GM}{\lambda^2} > F_p \simeq \frac{v_s^2}{\lambda} \ , \tag{2.1}$$

where v_s is the typical velocity of a particle in the fluid, corresponding to the sound speed in a collisional gas (or to the r.m.s. of the velocity distribution of a collisionless fluid as DM). Since the DM perturbation is tiny, the inner mass results $M \sim \rho_B \lambda^3$, then the scale at which the equilibrium is reached by the two forces is

$$R_J = \lambda \simeq \frac{v_s}{\sqrt{G\rho_B}} \ . \tag{2.2}$$

This is called the Jeans length, showing that only the fluctuations on scale larger than the Jeans radius can grow, since on the other scales they are dissipated by the random walks of the fluid. It

is important to notice that v_s is the velocity of the component that undergoes the perturbation, while ρ_B is the mean density of the universe, i.e. the one of its dominant component. In the case of cold DM (CDM), here assumed to be a collisionless fluid, the velocity of the particle is negligible after the decoupling from radiation, so that its perturbations can grow at every cosmological scale, after the equivalence epoch.

2.1.2 The Perturbation evolution

The theoretical approach to describe the evolution of the perturbations of a given field is based on the assumption that, in the linear regime, the typical value of such fluctuations is much smaller than unity. In this case, perturbing the fields of interest to the first order represents a useful analytic tool which, together with the FRW metric and under the assumption of an uniform distribution for the background universe, can provide a good theoretical picture for the growth of fluctuations. A detailed analysis in this direction is presented by Padmanabhan (1993) and Straumann (2004), but here we are interested only to recall the main aspects of their evolution in the Newtonian regime, since this is the case of the present work, i.e. spatial scales much smaller than the horizon radius, peculiar velocities smaller than the speed of light and a gravitational potential much smaller than unity (in geometrized units), slowly varying in time.
Let us introduce a generic fluid, with density ρ, velocity field $\boldsymbol{U}$, under the action of a potential Φ and a pressure p. The time-evolution for the distribution function $\rho(\boldsymbol{r}, \boldsymbol{U}, t)$ in the phase-space, where r is the position of a given fluid element, is provided by the Boltzmann Equation:

$$\frac{\partial \rho}{\partial t} + \frac{\partial \rho}{\partial \boldsymbol{r}} \cdot \boldsymbol{U} + \frac{\partial \rho}{\partial \boldsymbol{U}} \cdot \nabla_{\boldsymbol{r}} \Phi = \frac{\partial \rho}{\partial t}\Big|_{coll} \tag{2.3}$$

where the right-hand-side term accounts for the pressure contribution due to collisions. The derived equations are

$$\frac{\partial \rho}{\partial t} + \frac{\partial \rho U_i}{\partial r_i} = 0 \tag{2.4}$$

$$\frac{\partial U_i}{\partial t} + U_j \frac{\partial U_i}{\partial r_j} + \frac{\partial \Phi}{\partial r_i} = -\frac{1}{\rho}\frac{\partial p}{\partial r_i} \ , \tag{2.5}$$

where the pressure term can be written as a function of the velocity dispersion tensor, σ_{ij}^2, through the definition $p\delta_i j = \rho\sigma_{ij}^2$. Anyway, as already pointed out, DM can be considered as a collisionless fluid due to its small cross section and the pressure term can be neglected. Eq. (2.4) and (2.5) are the continuity and the Euler's equations respectively and, in order to close the system, it is necessary to introduce also the Poisson equation:

$$\triangle \ \Phi = 4\pi G\rho \ . \tag{2.6}$$

The perturbing analysis is made by assuming that a generic field q can be expressed in term of a background component q_B and a tiny deviation $\delta q \ll q_B$, such that $q = q_B + \delta q$. Inserting in the system above and removing the unperturbed solutions, the analysis of the lowest non-trivial order allows to find a differential equation for the perturbations. Generally, this investigation is made in the Fourier space, writing the perturbation $\delta \equiv \delta q/q_B$ in the real space as the sum of its Fourier components $\hat{\delta}(\boldsymbol{k})$, where $\boldsymbol{k}$ is the wavenumber corresponding to a given wavelength.
For the purpose of this Thesis, the following discussion will be focused only on expanding universes. Then, in the case of the density, combining Eqs. (2.4), (2.5) and (2.6) gives

$$\frac{\partial^2 \hat{\delta}(\boldsymbol{k})}{\partial t^2} + 2H\frac{\partial \hat{\delta}(\boldsymbol{k})}{\partial t} + (k^2 c_s^2 - 4\pi G\rho_B)\hat{\delta}(\boldsymbol{k}) = 0 \ , \tag{2.7}$$

in which $c_s^2 = \delta p/\delta\rho$ is the sound speed for a collisional fluid, that must be replaced by a quantity v_*^{-2} depending on the velocity field dispersion, in case of a collisionless field. Eq. (2.7) is a sort of oscillator equation, with the first term representing the inertial motion and the second one representing the dynamical friction due to the expansion of the universe. The third term shows

the interplay of the gravity and pressure forces due to the random motions of the particles and provides a more accurate definition for the Jeans scale:

$$R_J = c_s \sqrt{\frac{\pi}{G\rho_B}} \ . \tag{2.8}$$

On the other hand, in a case of a collisionless (DM) fluid, R_J is negligible and the third term in the left-hand side of Eq. (2.7) can be neglected.
The general solution of Eq. (2.7) can be expressed as a sum of two independent terms, that can be obtained analitically only for particular simple cosmological models, not necessarily flat, while in the other cases a numerical integration is required. In a case of a flat, DM-dominated Einstein de Sitter (EdS) universe,

$$\hat{\delta}(\boldsymbol{k}) = \hat{\delta}_-(k) + \hat{\delta}_+(k) \tag{2.9}$$

for which

$$\hat{\delta}_-(k) \propto t^{-1} \tag{2.10}$$

$$\hat{\delta}_+(k) \propto t^{2/3} \ , \tag{2.11}$$

where the minus and plus exponential indicate that the first solution decreases in time while the second one increases. For this reason the contribution of the first component can be neglected and the solution is identified with its growing mode.
Hence, in the real space, the overdensity at a given point can be written as

$$\delta(\boldsymbol{r}) = \sum_{\boldsymbol{k}} \hat{\delta}(\boldsymbol{k}) \exp(i\boldsymbol{k}\cdot\boldsymbol{r}) = V \int_V \hat{\delta}(\boldsymbol{k}) \exp(i\boldsymbol{k}\cdot\boldsymbol{r}) \frac{\mathrm{d}^3\boldsymbol{k}}{(2\pi)^3} \ , \tag{2.12}$$

where V can be thought as the volume of the 'fair sample' of the universe, and analogously

$$\hat{\delta}(\boldsymbol{k}) = \frac{1}{N} \sum_{\boldsymbol{r}} \delta(\boldsymbol{r}) \exp(-i\boldsymbol{k}\cdot\boldsymbol{r}) = \frac{1}{V} \int_V \delta(\boldsymbol{r}) \exp(-i\boldsymbol{k}\cdot\boldsymbol{r}) \, \mathrm{d}^3\boldsymbol{r} \tag{2.13}$$

in which N is the number of points in which $\delta(\boldsymbol{r})$ is sampled inside the volume V.
In general, it is preferred to express the linear solution as a function of the linear grow factor $D(z)$, defined as the ratio between the growing mode $\hat{\delta}_+(k)(t)$ at a given time t and its value at $z = 0$, namely $D(z) = \hat{\delta}_+(k,z)/\hat{\delta}_+(k, z=0)$, so that for a EdS universe it results $D(z) = (1+z)^{-1}$. It can be related to the growth factor $g(z)$ normalized to the scale factor a for which Carroll et al. (1992) found the following analytic espression:

$$g(z) = \frac{5}{2}\Omega_m(z) \left[\Omega_m(z)^{4/7} - \Omega_\Lambda(z) + \left(1 + \frac{\Omega_m(z)}{2}\right) + \left(1 + \frac{\Omega_\Lambda(z)}{70}\right) \right]^{-1} \ . \tag{2.14}$$

From the above equation, it results that $g(z) \sim 1$ at early epoch, when the matter contribution dominates the gravity, but it decreases with the expansion factor at late redshifts, during the era dominated by DE.

The growth of the matter fluctuations is affected by a quintessence component. This is clearly shown in Fig. 2.1, where the evolution for the growth factor for a standard ΛCDM cosmology is represented together with those predicted for the RP and the SUGRA quintessence cases introduced in the previous chapter. It is evident that, at the same cosmological epoch, $D(z)$ is larger for the RP and the SUGRA models. Then, the growth of the fluctuations is anticipated with respect to the standard universe and it has strong repercussions on the following structure formation.

2.2 Statistics of Gaussian random fields

The current paradigm adopted to analytically describe the evolution of the structures assumes that the overdensity field rising from the inflationary epoch is random, i.e. the value of δ at a

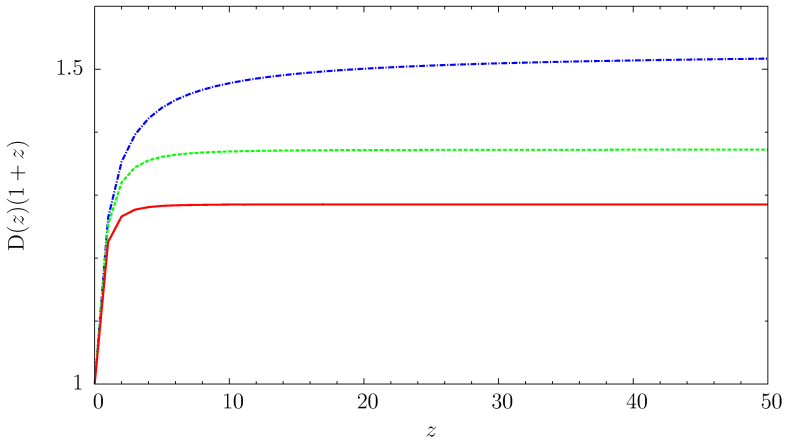

Figure 2.1: Redshift evolution of the growth factor, given in terms of $D(z)(1+z)$ and normalized to its value at the present time. Different lines refer to ΛCDM model (red solid line), RP model (green dashed line) and SUGRA model (blue dotted-dashed line).

particular point of the universe is a stochastic variable that follows a particular distribution. In theory, the statistical properties of a random field are determinated by averages over a sample of different realizations of the field, but indeed this can not be applied to our universe, since we know just one realization. The introduction of the ergodic assumption allows to solve this problem, assuming to use a sample of different regions of this universe far enough between each other to be considered as different realizations of the random field. As immediate consequence, the average over the sample can be reduced to make the spatial average over different and sufficiently large regions of the universe. This assumption has been rigorously for a particular class of random fields by Adler (1981), but it has to be remarked that when large scale are needed, there are very few far enough regions in the universe and the average loses its statistical significance. This problem is called the cosmic variance.
As predicted by the inflationary scenario, at the end of the accelerated expansion of the universe the distribution of the overdensity field should be close to a Gaussian. Actually, see Section 2.4, some tiny deviations from the Gaussian distribution are allowed, but in this section we will neglect them. In this case, the distribution of the matter field is fully described by the mean value of the overdensity field, that is null by definition, and its variance σ^2, defined such that $\sigma^2 \equiv \langle \delta^2(\boldsymbol{r}) \rangle$, that using Eq. (2.12) reads as

$$\sigma^2 = \frac{1}{V} \int \hat{\delta}(\boldsymbol{k}) \hat{\delta}^*(\boldsymbol{k}) \frac{\mathrm{d}^3\boldsymbol{k}}{(2\pi)^3} = V \int_V |\hat{\delta}(\boldsymbol{k})|^2 \frac{\mathrm{d}^3\boldsymbol{k}}{(2\pi)^3} = V \int_0^{+\infty} |\hat{\delta}(k)|^2 k^2 \frac{\mathrm{d}k}{2\pi^2} \ , \tag{2.15}$$

in which in the right hand side we take into account the cosmological principle and we consider that there is no preferred direction. Moreover, the volume V can be assumed to be large enough to satisfy the ergodic hypothesis or as small as to avoid possible space curvature. It is also possible to express the variance as a function of the power spectrum $P(k)$ of the density fluctuations, i.e.

$$P(k) \equiv |\hat{\delta}(k)|^2 \ , \tag{2.16}$$

leading to

$$\sigma^2 = V \int_0^{+\infty} P(k) k^2 \frac{\mathrm{d}k}{2\pi^2} = \int_{-\infty}^{+\infty} \Delta(k)^2 \, \mathrm{d} \ln k \ , \tag{2.17}$$

setting the adimensional power spectrum $\Delta^2(k)$ as

$$\Delta^2(k) \equiv \frac{V}{2\pi^2} k^3 P(k) \ . \tag{2.18}$$

The inflationary model produces an initial scale-free power spectrum of the form $P_i(K) = Ak^n$, where A is a normalization constant and n is the spectral index. A particular case of n has

been proposed by Harrison (1970) and Zel'Dovich (1970), that working independently, suggested $n = 1$. Assuming this particular spectral index, the fluctuations on the gravitational potential Φ are independent on the physical scale and enter inside the cosmological horizon with a constant variance. For this reason it is called a scale-invariant spectrum.
As introduced up to now, the overdensity field give no information about the statistics of the collapsed objects with a given mass. Hence, it is convenient to define the filtered overdensity field, as the convolution of the real density field with a filter function having a scale R_f:

$$\delta_f(\boldsymbol{r}; R_f) = \int \delta(\boldsymbol{r}')F(|\boldsymbol{r} - \boldsymbol{r}'|; R_f)\,\mathrm{d}^3\boldsymbol{r}' \ . \tag{2.19}$$

In the above equation, F represents the filter function, that we assume to be a top hat filter:

$$F_{TH}(|\boldsymbol{r} - \boldsymbol{r}'|; R_{TH}) = \frac{3}{4\pi R_{TH}^3}\Theta\left(1 - \frac{|\boldsymbol{r} - \boldsymbol{r}'|}{R_{TH}}\right) \ . \tag{2.20}$$

In the Fourier space, the convolution becomes a linear product between the $\hat{\delta}(\boldsymbol{k})$ field and the Fourier transform of the filter F, i.e.

$$\delta_f(\boldsymbol{r}; R_f) = \int \frac{\mathrm{d}^3\boldsymbol{k}}{(2\pi)^3} W(kR_f)\hat{\delta}(\boldsymbol{k})\exp(i\boldsymbol{k}\cdot\boldsymbol{r}) \tag{2.21}$$

where the window function W for a top hat filter is

$$W_{TH}(kR_{TH}) = \frac{3[\sin(kR_{TH}) - kR_{TH}\cos(kR_{TH})]}{(kR_{TH})^3} \ , \tag{2.22}$$

representing a low-band filter. In fact it vanishes for perturbations characterized by scales larger than R_f while equals unity in the other case. It follows that the filtered variance reads as

$$\sigma^2(R_f) = V\int_0^{+\infty} P(k)W^2(kR_f)k^2\frac{\mathrm{d}k}{2\pi^2} \ , \tag{2.23}$$

that clearly shows the behaviour of the smoothed variance as a function of mass. In fact, if the smoothing radius is null the corresponding smoothed variance results as in the unfiltered case, while when R_f becomes extremely large the variance approaches 0. Since to the filter radius corresponds a mass $M \propto R_f^3$, the smoothed variance could be considered as a decreasing function of mass. If a top-hat window function is considered, in case of a scale-free power spectrum, the variance of the smoothed field can be written as

$$\sigma^2(R_f) = \frac{2A}{n+3}\frac{(2\pi)^{n+1}}{R_f^{n+3}} \ , \tag{2.24}$$

that implies, fixed the spectral index, the following relation between the normalization of the power spectrum and the variance smoothed on a given physical scale R:

$$A = \sigma^2(R_f)\frac{R_f^{n+3}}{(2\pi)^{n+1}}\frac{n+3}{2} \ . \tag{2.25}$$

In the above equation, it is usual to set $R = 8h^{-1}$ Mpc to achieve the normalization constant A.
In the post inflationary epoch, the shape of the power spectrum suffers of the action of other physical processes. In fact, its slope is mainly modified by the Meszaros effect (Meszaros, 1974). During the radiation era, i.e. before the matter-radiation equality, the growing mode of the matter perturbation inside the horizon remains frozen also on scales larger than R_J. In fact, the growth of the perturbations is inhibited by the pressure on scales larger than the distance crossed by the acoustic waves during the free-fall time. As a consequence, the time at which the matter overdensity reaches the unity is delayed, with remarkable repercussions on the structure formation. The net effect of this phenomenon is the alteration of the initial shape of $P(k)$, that can be described using the transfer function $T(k)$ as follows

$$P(k) = P_i(k)T^2(k) = Ak^nT^2(k) \ . \tag{2.26}$$

The shape of the transfer function is obtained by numerical integrations. A commonly used formula has been first obtained by Bardeen et al. (1986),

$$T(k) = \frac{\ln(1+2.34q)}{2.34q}[1+3.89q+(1.61q)^2+(5.46q)^3+(6.71q)^4]^{-1/4} \tag{2.27}$$

where $q = k/\Gamma h^{-1}$ Mpc and Γ is the shape parameter that determines the distribution of the power on large scales and can be probed by the observations. Percival et al. (2001) estimated $\Gamma \sim 0.20$ from the Sloan Digital Sky Survey (SDSS) data, in agreement with the predictions of the analytic formula proposed by Sugiyama (1995),

$$\Gamma = \Omega_{m,0} h \exp\left[-\Omega_{b,0}\left(1+\frac{\sqrt{2h}}{\Omega_{m,0}}\right)\right] . \tag{2.28}$$

in which the contribute of the baryonic matter is considered. A similar transfer function has been implemented also Eisenstein & Hu (1998).
Finally, another effect that can modify the amplitude of the power spectrum is due to the time-evolution of matter fluctuations, following the growth factor $D(z)$. As a consequence, by its definition, the power spectrum evolves in z as

$$P(k,z) = P_i(k)T^2(k)D^2(z) . \tag{2.29}$$

2.3 Non-linear evolution

2.3.1 The Zel'dovich approximation

When the amplitude of the perturbartions approaches the unity, the validity of the linear approximation decays and the evolution of the overdensity in the non-linear regime has to be investigated through numerical simulations. There are however many semi-analytic methods that, although unable to describe the most realistic astrophysical situations, are powerful instruments to give a rough picture of the non-linear growth of the overdensity.
One of these tools has been introduced by Zel'Dovich (1970) and is the so-called Zel'dovich approximation. Assuming that the scales of interest are much smaller than the horizon scale and that the universe is matter dominated and has no curvature, the Zel'dovich approximation relates the eulerian position $\boldsymbol{r}(t)$ to the initial (Lagrangian) position $\boldsymbol{x}_0$ through the displacement $\mathrm{d}\boldsymbol{q}$:

$$\boldsymbol{r}(t) = a(t)(\boldsymbol{x}_0 + \mathrm{d}\boldsymbol{q}) , \tag{2.30}$$

where x_0 is the comoving coordinate corresponding to the starting position of the particle, while $\mathrm{d}\boldsymbol{q} = b(t)\boldsymbol{p}(\boldsymbol{x}_0)$ is the time-dependent displacement into the comoving position of the particle due to the effect of density fluctuations. The physical peculiar (i.e. not due to the expansion of the universe) velocity field is then given by

$$\dot{\boldsymbol{r}}(t) - H\boldsymbol{r} = a(t)\dot{D}(t)\boldsymbol{p}(\boldsymbol{x}_0) . \tag{2.31}$$

All the main properties of this method are encapsulated in the Jacobian matrix, $\mathcal{J}_{ij} = \partial r_i/\partial x_{0,j}$. In fact, as long as the Jacobian is not singular, the trajectories of particles do not cross and the mass conservation implies

$$\rho(\boldsymbol{x}_0,t) = \frac{a^3(t)\rho_B}{\det \mathcal{J}(\boldsymbol{x}_0,t)} = \frac{\rho_B}{[1+b(t)\lambda_1][1+b(t)\lambda_2][1+b(t)\lambda_3]} , \tag{2.32}$$

where ρ_B is the background density and $\lambda_i = \lambda_i(\boldsymbol{x}_0)$ are the eingenvalues of the Jacobian. For times close to the initial one, the peculiar displacement is small, then $b(t)\lambda_i \ll 1$ and the density fluctuation can be written to the first order as $\delta(\boldsymbol{x}_0,t) \simeq b(t)(\lambda_1+\lambda_2+\lambda_3)$. On the other hand, if at a given time t_c the shell-crossing occurs, one or more of the eingenvalues approaches to 0 so that $b(t_c) = -1/\lambda_i$ implying a collapse of the density fluctuations along the corresponding axis. In case of a single null eingenvalue, the formed structure will be bidimensional and it is called pancake.

When two eingenvalues are null the originated structure is called filament. A collapsed structure is formed if all the eingenvalues are null.
Since the Zel'dovich approximation is only a kinematical description of the action of the densitiy fluctuations on the particle trajectories, after the shell-crossing it loses its validity and the evolution of the perturbations can be investigated only through numerical simulation.

2.3.2 The collapse

As the perturbation increases, it approaches to unity and the region evolves only by its gravity, independently of the background universe. In such a case, the regions can collapse. In the following analysis, the effects of the pressure are neglected and the main component of the cosmic fluid is assumed to be DM, such that the dynamic of the region is fully described by its gravitational potential $\Phi = \Phi_B + \delta\Phi$, in which the background potential can be written as $\Phi_B = -\ddot{a}r^2/2a)$ to the lowest non-trivial order (Padmanabhan, 1993). From Eq. 1.17 it follows that

$$\Phi = \frac{2\pi G}{3}\rho_B(t)r^2 + \delta\Phi \ . \tag{2.33}$$

Let us take now a particle under the action of the gravitational potential of the overdensity field, at physical distance r from the center of a perturbed region of mass $M = 4/3\pi r^3\rho_B(t)(1+\bar{\delta}(t))$ with inner mean overdensity $\bar{\delta}$

$$\bar{\delta}(t) = 4\pi\int_0^r \delta(r',t)r'^2\,\mathrm{d}r' \ . \tag{2.34}$$

Through the integration of its equation for motion, $\ddot{r} = -GM/r^2$, it is possible to estimate its total energy

$$E = \frac{1}{2}\dot{r}^2 - \frac{GM}{r} \tag{2.35}$$

which can give us an idea of the following evolution of the perturbation. In fact, if $E > 0$ the inertial term $\ddot{r}$ in Eq. (2.35) is large enough to prevent forever the collapse of the regions. In the case $E = 0$, the expansion will possibly stop but at $r \to \infty$ and, finally, when $E < 0$ the action of the expansion will be balanced by gravity at a given time (called turn-around t_m) and, subsequently, the region will collapse. In this case, the kinetic (K) and potential (U) parts of the energy becomes

$$K \equiv \frac{\dot{r}^2}{2} = \frac{1}{2}H^2r^2 \ ; \tag{2.36}$$

$$U \equiv -\frac{GM}{r} = -\frac{1}{2}H^2r^2[1+\bar{\delta}(t)]\Omega_{m,B}(t) \ , \tag{2.37}$$

where $\Omega_{m,B}(t)$ is the background density of the region. It follows that the collapse condition reads as $\bar{\delta}(t) > \Omega_{m,B}^{-1}(t) - 1$ which, considering only the growing term of the perturbation, can be written as $\bar{\delta}_+ = 3/5\bar{\delta} > 3/5(\Omega_{m,B}^{-1}(t) - 1)$. Supposing that $E < 0$ and neglecting the kinetic term $\dot{r}$ allows the typical parameters at turn-around to be written as

$$t_m = \Big[\frac{3\pi}{32G\rho(t_m)}\Big]^{1/2} \tag{2.38}$$

$$r_m \equiv r(t_m) = r(t_i)\frac{1+\bar{\delta}(t_i)}{1+\bar{\delta}(t_i)-\Omega_{m,B}(t_i)^{-1}} \tag{2.39}$$

$$\rho(t_m) = \rho_c(t_i)\Omega_m(t_i)[1-\Omega_m(t_i)^{-1}]^3. \tag{2.40}$$

In the previous equations, t_i is a fixed initial time to which we refer since the conservation of mass-energy is assumed and ρ (and Ω_m) represent the inner density of the perturbed region, namely $\Omega_m \equiv \rho/\rho_c = \rho_B(1+\bar{\delta})/\rho_c = \Omega_{m,B}(1+\bar{\delta})$. Once the collapse is occurred, the region will reach the virial equilibrium and finally $U = -2K$. That leads to achieve the virial radius as $r_v = r_m/2$, while its time-evolution, provided by solving Eq. (2.35), allows to estimate the time corresponding to a complete virialization t_v. Numerical simulations show that $t_v \simeq 3t_m$. Fixed the virial overdensity as the ratio between the averaged density of the perturbation at t_v and the

critical density, namely $\Delta_v = \rho t_v/\rho_c(t_v)$, it can be shown that in a EdS universe $\Delta_v \simeq 178$ and the corresponding overdensity is $\delta_c \simeq 1.686$. These estimates are affected by the possible presence of DE, and a fitting formula has been found introducing an additional energy contribution to the virial relation (Wang & Steinhardt, 1998; Mota & van de Bruck, 2004; Wang, 2006; Bartelmann et al., 2006). The approximate analytic expressions for Δ_v and δ_c in a flat universe such that $\Omega_{m,B} + \Omega_{\Lambda,B} = 1$ are

$$\Delta_v = 9\pi^2[1 + 0.7076(\Omega_{m,B} - 1) + \Omega_{m,B}^{0.4403}] \ , \tag{2.41}$$

$$\delta_c = \frac{3}{5}\left(\frac{3\pi}{2}\right)^{2/3} [1 + 0.0123\log(\Omega_{m,B})] \ , \tag{2.42}$$

that, unlike in a EdS universe in which they are constant, for a generical cosmological model depend on time through $\Omega_{m,B}(z)$ (see e.g. Lacey & Cole, 1993; Eke et al., 1996; Bryan & Norman, 1998, for more details). It follows that the virial mass of the perturbed region is

$$M_v = \frac{4}{3}\pi r_v^3 \Delta_v(t_v)\rho_c(t_v) \tag{2.43}$$

and the corresponding total energy is

$$E = -\frac{1}{2}\frac{3GM_v^2}{5r_v} \ . \tag{2.44}$$

Although overdensity at virialization can be calculated in every case according to the chosen cosmological background, the use of $\Delta_v = 200$ is often preferred, since it does not depend on the cosmological model and provided that numerical simulations show as r_{200} separate the inner, in equilibrium part of a galaxy cluster from the infall, outer one.
As presented, the spherical collapse formalism counts on some hypotheses that could possibly be unrealistic. Sheth & Tormen (1999), and Sheth et al. (2001), investigate its validity through numerical simulations in a EdS universe in which the predicted adundance of the collapsed objects was compared to that obtained analytically (see next section). The appearing scenario showed that the formation of the virialized structures was in agreement with the collapse of elliptical regions, rather than spherical. Analytically, this leads to the introduction of a different threshold δ_c, namely

$$\delta_c(M, z) = \sqrt{a}\delta_c(z)\left[1 + b\left(\frac{\sigma^2(M)}{a\delta_c^2(z)}\right)^2\right] \ . \tag{2.45}$$

Here, (a, b, c) are fitting parameters, that Sheth & Tormen (1999) showed to be $a = 0.707, b = 0.5$ and $c = 0.6$ according to the predictions of the high-resolution numerical simulations and have been later improved by Jenkins et al. (2001), that find $a = 0.73, b = 0.34$ and $c = 0.81$. The peculiarity of this barrier is its dependence on the mass of the considered region, but anyway for massive structures (2.45) reduces to the spherical collapse case.

2.3.3 The statistics of the collapsed objects with Gaussian ICs

The collapse model together with the statistics of random fields allows to derive the abundance of the formed structures having a fixed mass M at a given redshift z, dubbed the mass function $n(M, z)$. More in details, it returns the comoving number density of the objects per unit mass around M and per unit redshift around z. Press & Schechter (1974) (PS74), Bond et al. (1991) and Sheth (1998), developed a theoretical formalism, the so-called excursions-set method, through which it is possible to find an analytic expression for $n(M, z)$. In the following discussion, we will recall the main results useful to the work presented in this Thesis, as achieved by Sheth (1998) to avoid the troubles of the PS74 approach.
In the excursion-set formalism, $p(\sigma^2, \delta)$ denotes the fraction of the points in a given volume such that the inner overdensity is δ over a scale of mass corresponding to $\sigma^2(M)$ and $p(\sigma^2, \delta|\sigma^{2'}, \delta', first)$ the fraction of the trajectories, having δ at σ^2, that first cross a threshold collapse $B(\sigma^2|R, z)$ at $\sigma^{2'}$ such that $\sigma^{2'} \leq \sigma^2$. Note that here B is written as a generic relation of M, z and the eulerian

radius $R(M)$ but the following treatment can be applied at best in cases where B is a linear function of σ^2 (Sheth, 1998). Hence

$$p(\sigma^2,\delta)=\int_0^{\sigma^2} p(\sigma^2,\delta|\sigma^{2'},\delta',first)f(\sigma^{2'},\delta'|R,z)\,\mathrm{d}\sigma^{2'}\ , \tag{2.46}$$

provided that at σ^2, $\delta>\delta_c(z)$. Here, f is the fraction of trajectories in the Lagrangian space that have their first crossing at σ^2, and can be related to the number of regions $N(M|R,z)$ having mass M, volume $V(M)$ in Lagrangian space and eulerian radius $R(M)$ at z:

$$f=\frac{VN}{V_{tot}}\frac{\mathrm{d}M}{\mathrm{d}\sigma^2}\ , \tag{2.47}$$

where V_{tot} is the total volume occupied by such regions in Lagrangian space. As known, the probability $p(\sigma^2,\delta)$ follows the Gaussian statistic and $p(\sigma^2,\delta|\sigma^{2'},\delta',first)$ corresponds to $p(\sigma^2,\delta|\sigma^{2'},\delta')$ when the filter is sharp in $k-$space, i.e.

$$p(\sigma^2,\delta) = \frac{1}{\sqrt{2\pi}\sigma}\exp\left(-\frac{\delta^2}{2\sigma^2}\right) \tag{2.48}$$

$$p(\sigma^2,\delta|\sigma^{2'},\delta') = \frac{1}{\sqrt{2\pi(\sigma^2-\sigma^{2'})}}\exp\left[-\frac{(\delta-\delta')^2}{2(\sigma^2-\sigma^{2'})}\right]\ . \tag{2.49}$$

When the collapsing regions are DM halos, the barrier B has no dependence neither on σ^2 nor on R (since a DM halo has null eulerian radius by definition), hence as already mentioned $B=\delta_c(z)$ and an analytic espression for f is taken directly solving (2.46):

$$f[\sigma^2,\delta_c(z)]=\frac{\delta_c(z)}{\sigma^2}p[\sigma^2,\delta_c(z)]=\frac{\delta_c(z)}{\sqrt{2\pi}\sigma^3}\exp\left[-\frac{\delta_c(z)^2}{2\sigma^2}\right]\ . \tag{2.50}$$

The mass function $n(M,z)=N(M,z)/V_{tot}$ then results

$$n(M,z)=\frac{\bar{\rho}_{0,m}}{M}f[\sigma^2,\delta_c(z)]\frac{\mathrm{d}\sigma^2}{\mathrm{d}M}=\frac{\bar{\rho}_{0,m}}{M}\frac{\delta_c(z)}{\sqrt{2\pi}\sigma^3}\exp\left[-\frac{\delta_c^2(z)}{2\sigma^2}\right]\frac{\mathrm{d}\sigma^2}{\mathrm{d}M}\ . \tag{2.51}$$

Although this formula, usually called the PS74 mass function, is in reasonable agreement with numerical simulations, with the introduction of the ellipsoidal collapse a more general espression has been proposed by Sheth & Tormen (1999) (ST99), and later by other authors as Jenkins et al. (2001)(J01) or Warren et al. (2006). The previous form for $n(M,z)$ has been improved adding the fitting parameters (A,a,p) and reads

$$n(M,z)=-\frac{\bar{\rho}_{0,m}}{M}\frac{\mathrm{d}\ln[\sigma(\mathrm{M})]}{\mathrm{dM}}\sqrt{\frac{2}{\pi}}A\left(1+\frac{1}{\nu^{2p}}\right)\nu\exp(-\nu^2/2)\ , \tag{2.52}$$

where $\nu\equiv\sqrt{a}\delta_c(z)/\sigma(M)$. Initial values for A and p were found by ST99 that achieve $A=0.322$ and $p=0.3$, that were improved by J01 in $A=0.353$ and $p=0.175$. Moreover, from Eq. (2.52), it is evident that assuming $A=0.5, a=1, p=0$ the mass function reduces to the original PS74 case.

The halo distribution provided by the spherical and the ellipsoidal collapse model are shown in Fig. 2.2, at $z=0$. It is evident that the PS74 mass function overpredict the number of low-mass structures when compared to ST99 and the J01, while underpredict it in the high-mass tail.

Due to its influence on the evolution of the matter fluctuations, the quintessence is expected to strongly affect the abundance of the dark matter halos, as shown in Fig. 2.3. Here we plot the mass function in terms of the size probability distribution $P(R)=\mathrm{d}n/\mathrm{d}\ln RV(R)/f_{col}(z)$, where f_{col} is the total collapsed mass fraction at the considered redshift, as predicted by the PS74 theory for the ΛCDM (solid line), RP (dashed line) and SUGRA (dotted-dashed line) cosmologies. For the purpose of this Thesis, we are interested in investigating the contribution of the DDE component at early epochs, i.e. when reionization begins. Then, the halo abundance is here shown at high

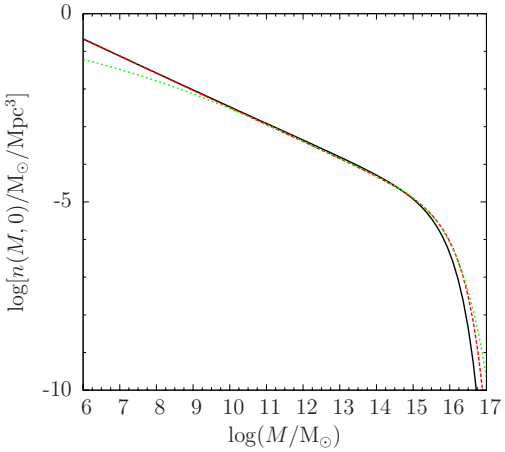

Figure 2.2: Mass function computed at present day in a ΛCDM cosmological framework consistent with the 1-year WMAP predictions. The black solid curve represents the PS74 original formulation, while the red dashed and the green dotted lines refer to the ST99 and J01 improved forms, respecively.

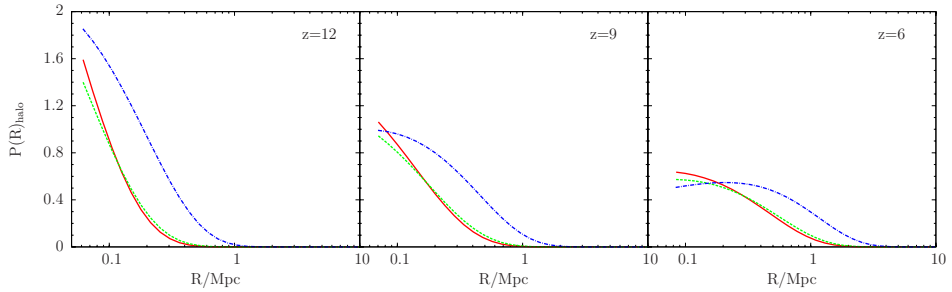

Figure 2.3: The halo distribution at different epochs: redshifts $z = 12$, $z = 9$, and $z = 6$ are shown in the panels, from left to right. For each cosmological model, the halo mass function is computed consistently to the PS74 formalism and written in terms of the halo radius. Different curves refer to ΛCDM model (solid line), RP model (dashed line) and SUGRA model (dotted-dashed line).

z. Indeed, at the same cosmological epoch, the halo distribution is dominated by larger objects in the quintessence cases, in particular in the SUGRA model, due to the earlier growth of matter fluctuations.

Analogously to the mass function, for the spherical collapse assumption it is possible to infer the halo merger rate, according to the hierarchical picture in which low mass structures aggregate each other to form higher mass objects. The first authors that analysed this problem were Lacey & Cole (1993), that related the merger rate to the conditional probability distribution that a trajectory that exceeds the barrier $\delta_c' = \delta_c(z')$ at mass M' (i.e. $\sigma^{2'}$) could re-cross the threshold at $z < z'$ (so that $\delta_c < \delta_c'$) for $M > M'$ (i.e. at $\sigma^2 < \sigma^{2'}$):

$$f(\sigma^{2'}, \delta_c'|\sigma^2, \delta_c) = \frac{\delta_c' - \delta_c}{\sigma^{2'} - \sigma^2} p(\sigma^{2'}, \delta_c'|\sigma^2, \delta_c) \ . \tag{2.53}$$

It follows that the fraction of regions of mass M' at z' that at z are contained in regions of mass M is $n(M'z'|M, z) = M/M' f(\sigma^{2'}, \delta_c'|\sigma^2, \delta_c) \mathrm{d}\sigma^{2'}/\mathrm{d}M'$, that, through straighforward calculation presented in Lacey & Cole (1993), in the limit $\Delta z \longrightarrow 0$ leads to the merger rate

$$\frac{\mathrm{d}^2 p}{\mathrm{d}\Delta M \mathrm{d}t} = \sqrt{\frac{2}{\pi}} \left| \frac{\mathrm{d}\delta_c(z)}{\mathrm{d}t} \right| \left| \frac{1}{\sigma^2} \right| \left| \frac{\mathrm{d}\sigma^2}{\mathrm{d}M} \right| \left(\frac{1}{1 - \sigma^2 \sigma^{2'}} \right)^{3/2} \exp \left[- \frac{\delta_c^2(t)}{2} \left(\frac{1}{\sigma^2} - \frac{1}{\sigma^{2'}} \right) \right] , \tag{2.54}$$

where $\Delta M = M - M'$. Given the difficulty introduced by using a barrier that does not depend linearly on the variance, at the moment it is not available an analogous espression for the merger rate in case of the ellipsoidal collapse.

2.4 Non-Gaussianity

As already explained, the standard scenario for inflation is based on a self-interacted scalar single field (inflaton) φ, evolving under the action of its potential $V(\varphi)$ minimally coupled to gravity, that is responsible for the rise of almost Gaussian density fluctuations, adiabatic on large scales. During this epoch, the inflaton dominates the gravity of the universe and, for this reason, the produced fluctuations in the energy-matter field cause the rise of adiabatic perturbations also in the geometric curvature of the universe. At the end of the inflation, the field oscillates around the minimum of its potential and decays, reheating the universe. The outcoming picture consists in an initial random overdensity field, following the Gaussian distribution, but the recent observational test (see sect. 2.5) do not reject a tiny deviation from the Gaussian statistic, also allowed by the theoretical standard inflationary paradigm. Anyway, in order for inflaton to drive the accelerated expansion, its potential $V(\psi)$ should be very flat and, as a consequence, the interaction terms responsible for the rise of non-linearities must be suppressed. It follows that producing non-Gaussianity during the inflation is forbidden, even if alternative scenarios provide at this epoch a pumping of the perturbations due to external fields, producing a non-negligible non-Gaussianity. Then, it is in the post inflation eras, i.e. during the following reheating and the radiation or matter epochs, that the possible initial non-Gaussianity can be enhanced by exploiting the conservation on large scales of the curvature perturbations up to second order.
The non-Gaussianity effect can be introduced in the following phenomenological way:

$$\Phi(\boldsymbol{x}) = \Phi_G(\boldsymbol{x}) + f_{\rm NL} * [\Phi_G^2(\boldsymbol{x}) - \langle \Phi_G^2(\boldsymbol{x}) \rangle] \ , \tag{2.55}$$

where $f_{\rm NL}$ is a parameter measuring the non-Gaussianity (NG hereafter) degree, while Φ and Φ_G are the gravitational potentials in the non-Gaussian and Gaussian model respectively. The '*' symbol denotes a convolution that is required if $f_{\rm NL}$ depends on space position, and that reduces to a scalar product in the opposite case. As it can be noticed, the above equation reduces to the Gaussian case if $f_{\rm NL} = 0$ is assumed, as provided by the definition of the NG parameter itself. In the equation above, the NG contribution is introduced in the gravitational potential of the perturbations, through an additional term proportional to Φ^2, but however, many different formalisms have been proposed in literature to account for NG effects. As an example, the perturbation can be added in the overdensity field itself (Matarrese et al., 2000) or directly in the curvature ζ, leading to $\zeta(\boldsymbol{x}) = \zeta_G(\boldsymbol{x}) + 3/5 f_{\rm NL}[\zeta_G^2(\boldsymbol{x}) - \langle \zeta_G^2(\boldsymbol{x}) \rangle]$ where the factor 3/5 renders this parameterization consistent to Eq. (2.55) (see e.g. Lo Verde et al., 2008, for details). It is interesting to note that, anyway, the NG contribution measured by last observations (see section 2.5) is smaller than 10^{-5}, not ruling the validity of the Gaussian model out.
In the Fourier space, Eq. (2.55) can be written as

$$\hat{\Phi}(\boldsymbol{k}) = \hat{\Phi}_G(\boldsymbol{k}) + \frac{1}{(2\pi)^3} \int \mathrm{d}^3\boldsymbol{k}_1 \, \mathrm{d}^3\boldsymbol{k}_2 \, \delta_D^{(3)}(\boldsymbol{k}_1 + \boldsymbol{k}_2 - \boldsymbol{k}) f_{\rm NL}(\boldsymbol{k}_1, \boldsymbol{k}_2) \hat{\Phi}_G(\boldsymbol{k}_1) \hat{\Phi}_G(\boldsymbol{k}_2) \tag{2.56}$$

in which $\delta_D^{(3)}$ is the Dirac delta function and the possible spatial dependence of $f_{\rm NL}$ is neglected. Under the assumption of mildly NG, an investigation of the NG effects on the structure formation is possible since the PDF of the smoothed overdensity field can be espressed analytically. In this case, the filtered $\delta_f(\boldsymbol{x}; R_f)$ can be found through Eq. (2.21) given the well-known relation between the potential Φ and the amplitude of the Fourier modes $\hat{\delta}(\boldsymbol{k})$

$$\hat{\delta}(\boldsymbol{k}) = M(k) \hat{\Phi}(\boldsymbol{k}) \tag{2.57}$$

where $M(k) = g(k)T(k)$ and the function $g(k)$ is related to the assumed model for the NG parameterisation. In case of the formalism here adopted, solving the Poisson equation allows to obtain

$$g(k) = \frac{2}{3\Omega_{m,0}} \left(\frac{k}{H_0} \right)^2 \tag{2.58}$$

The PDF of the filtered overdensity field can be achieved by the functional

$$P[\delta_f(\boldsymbol{x}; R_f)] = \left\langle \delta_D \left(\Phi_{G,R_f}(\boldsymbol{x}) + f_{\rm NL} \int \mathrm{d}^3\boldsymbol{y} \, F(|\boldsymbol{x} - \boldsymbol{y}|) \phi_G^2(\boldsymbol{y}) - C - \delta_f(\boldsymbol{x}; R_f) \right) \right\rangle \ , \tag{2.59}$$

where C is a normalization constant such that δ_f has null mean value. Through straightforward calculations (see Matarrese et al., 2000, for details), the resulting probability distribution for the smoothed NG overdensity field is

$$P(\delta_f) = \int \frac{\mathrm{d}\lambda}{2\pi} \exp(-i\lambda\delta_f + \mathcal{W}(\lambda)) \tag{2.60}$$

in which $\mathcal{W}$ represents the cumulant function of the $\iota - th$ order moments $\mu_\iota(R_f)$ of the smoothed density constrast, namely

$$\mathcal{W}(\lambda) \equiv \sum_{\iota=2}^{+\infty} \frac{(i\lambda)^\alpha}{\alpha!} \mu_\iota(R_f) \ . \tag{2.61}$$

In general, $\mu_\iota(R_f)$ can be written as the sum of two terms, $\mu_\iota(R_f) = f_{\rm NL}^{\iota-2}\mu_\iota^{(1)}(R_f) + f_{\rm NL}^{\alpha}\mu_\iota^{(2)}(R_f)$, in which the major NG contribution is provided only by the first component. In the following, we will treat the NG effects only at the linear order in $f_{\rm NL}$, then hereafter we will identify the momenta with their leading term, having the general form

$$\mu_\iota(R_f) \sim f_{\rm NL}^{\iota-2}\mu_\iota^{(1)}(R_f) = \int \frac{\mathrm{d}^3\boldsymbol{k}_1}{(2\pi)^3} ... \int \frac{\mathrm{d}^3\boldsymbol{k}_\iota}{(2\pi)^3} W(k_1R_f)..W(k_\iota R_f)\langle\hat{\Phi}(\boldsymbol{k}_1)..\hat{\Phi}(\boldsymbol{k}_\iota)\rangle. \tag{2.62}$$

By definition, the Gaussian statistics is characterized by null odd order moments and even order moments proportional to the $2 - th$ order one (the variance). This is not valid anymore for NG models, since the odd μ_ι's do not vanish. As a consequence, the $3 - th$ moment (the skewness) is the one at the lowest order with highest amplitude able to distinguish between NG and Gaussian distributions for the overdensity field, that could be constrained through the observations. Truncating $\mathcal{W}$ at the third element (since the $4 - th$ linear term has the same amplitude of the $3 - th$ non-linear term), the NG PDF is defined by

$$\mu_2(R_f) = \int \frac{\mathrm{d}^3\boldsymbol{k}_1}{(2\pi)^3} \int \frac{\mathrm{d}^3\boldsymbol{k}_2}{(2\pi)^3} W(k_1R_f)W(k_2R_f)M(k_1)M(k_2)\langle\hat{\Phi}(\boldsymbol{k}_1)\hat{\Phi}(\boldsymbol{k}_2)\rangle \tag{2.63}$$

$$\begin{aligned}\mu_3(R_f) = &\int \frac{\mathrm{d}^3\boldsymbol{k}_1}{(2\pi)^3} \int \frac{\mathrm{d}^3\boldsymbol{k}_2}{(2\pi)^3} \int \frac{\mathrm{d}^3\boldsymbol{k}_3}{(2\pi)^3} W(k_1R_f)W(k_2R_f)W(k_3R_f)\times \\ &M(k_1)M(k_2)M(k_3)\langle\hat{\Phi}(\boldsymbol{k}_1)\hat{\Phi}(\boldsymbol{k}_2)\hat{\Phi}(\boldsymbol{k}_3)\rangle \ .\end{aligned} \tag{2.64}$$

Here the $2 - th$ moment is determined by the power spectrum $P_\Phi(k)$ of the gravitational potential since $P_\Phi(k) \equiv \langle\hat{\Phi}(\boldsymbol{k}_1)\hat{\Phi}(\boldsymbol{k}_2)\rangle = (2\pi)^3\delta_D^{(3)}(\boldsymbol{k}_1 + \boldsymbol{k}_2)P_\Phi(k_1) = \Delta_\Phi k^{n-4}$, while the $3 - th$ moment depends on the bispectrum $\langle\hat{\Phi}(\boldsymbol{k}_1)\hat{\Phi}(\boldsymbol{k}_2)\hat{\Phi}(\boldsymbol{k}_3)\rangle$. Note that the sign of $f_{\rm NL}$ is correlated to that of the skewness, as well as of all the other even-order cumulants. It is commonly represented by the function F such that

$$\langle\hat{\Phi}(\boldsymbol{k}_1)\hat{\Phi}(\boldsymbol{k}_2)\hat{\Phi}(\boldsymbol{k}_3)\rangle = (2\pi)^3\delta_D^{(3)}(\boldsymbol{k}_1 + \boldsymbol{k}_2 + \boldsymbol{k}_3)F(k_1, k_2, k_3) \ , \tag{2.65}$$

which resumes the dependence of the 3-point correlation function on the shape of the triangle (k_1, k_2, k_3) in momentum space. The models proposed for F can be divided quite sharply into two main classes, with the consequence of a qualitatively different way to produce the skewness. The first possibility rise by taking a Taylor expansion around a Gaussian for the gravitational potential perturbation (Komatsu & Spergel, 2001) as done in Eq. (2.55), and implies a local non-linearity in real space. But this form is expected also for other mechanisms, as the curvaton scenario, or for models in which non-linearities develop outside the horizon, as the multiple-field inflation models where a second, light scalar field is considered. The function F reads as

$$F(k_1, k_2, k_3) = 2f_{\rm NL}^{loc}[P_\Phi(k_1)P_\Phi(k_2) + P_\Phi(k_1)P_\Phi(k_3) + P_\Phi(k_2)P_\Phi(k_3)] \ , \tag{2.66}$$

in which the most relevant configurations are the squeezed triangles with one side much smaller than the others, i.e. $k_1, k_2 \gg k_3$.
The second class are single field models with a non-minimal Lagrangian, where the correlation among modes is created by higher derivative operators. In this case, the stronger correlation

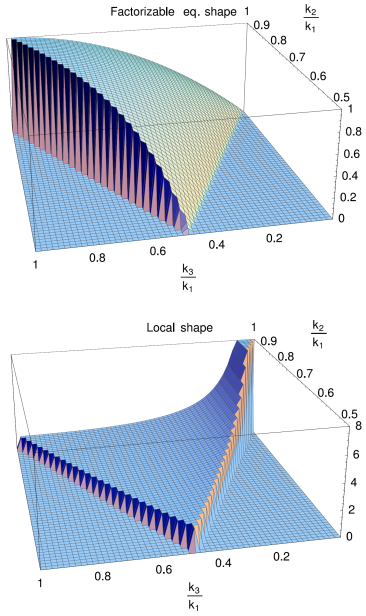

Figure 2.4: Figure 1: The function $F(1, k_2/k_1, k_3/k_1)(k_2/k_1)^2(k_3/k_1)^2$ for the equilateral shape (top panel) and for the local shape (bottom). The functions are both normalized to unity for equilateral configurations $k_2/k_1 = k_3/k_1 = 1$. Given the simmetry of F in its three arguments, it is sufficient to specify it for $k_1 \geq k_2 \geq k_3$, so that $k_3/k_1 \leq k_2/k_1 \leq 1$. Moreover, since no side can be higher than the sum of the other two in a triangle, only the region $1k_2/k_1 \leq k_3/k_1 \leq k_2/k_1 \leq 1$ is considered, setting it to zero elsewhere (Creminelli et al., 2006).

occurs among modes with comparable wavelength, i.e. $k_1 \sim k_2 \sim k_3$ in Fourier space. This class of fluctuations is called equilateral and some examples include the DBI model and the ghost inflation (Creminelli et al., 2006). In this case the function F is

$$F(k_1,k_2,k_3) = f_{\rm NL}^{equi} 6\Delta_\Phi^2 \Big[-\frac{1}{k_1^{4-n}k_2^{4-n}} + (2 \quad perm) - \frac{2}{(k_1k_2k_3)^{2-2(n-1)/3}} + \frac{1}{k_1^{1-(n-1)/3}k_2^{2-2(n-1)/3}k_3^{4-n}} + (5 \quad perm)\Big] . \tag{2.67}$$

The difference between this two cases are shown in Fig. 2.4, from which it is evident that while the contribute of the local shape is important in the edge of the Fourier space, the equilateral shape becomes important when $k_1 = k_2 = k_3$. The importance of this last case resides in the possibility to consider a scale-dependence for the NG parameter, as supposed by recent observational tests (see sect. 2.5). In this work, we also allow NG to vary with the scale, assuming the dependence proposed by Lo Verde et al. (2008), namely:

$$f_{\rm NL}(k_1,k_2,k_3) = f_{\rm NL}\left(\frac{k_1+k_2+k_3}{k_{\rm CMB}}\right)^{-2\alpha} . \tag{2.68}$$

In the following work, the normalisation of the previous relation is chosen in order to avoid violating the WMAP constraints: for this reason $f_{\rm NL}$ represents the equilateral parameter measured on the $k_{\rm CMB}$ scale of $0.086h/$ Mpc, roughly corresponding to the largest multipole used by Komatsu et al. (2008) to estimate NG in the WMAP data, $\ell = 700$. The slope α is a free parameter, assumed to be constant, such that $|\alpha| \ll 1$ between CMB and cluster scales. Following Lo Verde et al. (2008) we consider small negative values for α, to enhance NG on scales smaller than CMB.

The resulting behaviour for the $f_{\rm NL}$ parameter is shown in Fig. 2.5, where we assume $\alpha = 0, -0.1, -0.2$, for the slope of the scale dependence, and $f_{\rm NL} = -151$, and $f_{\rm NL} = 253$ as pivoting values at the CMB scale, in agreement with the WMAP equilateral constraints (see sect. 2.5

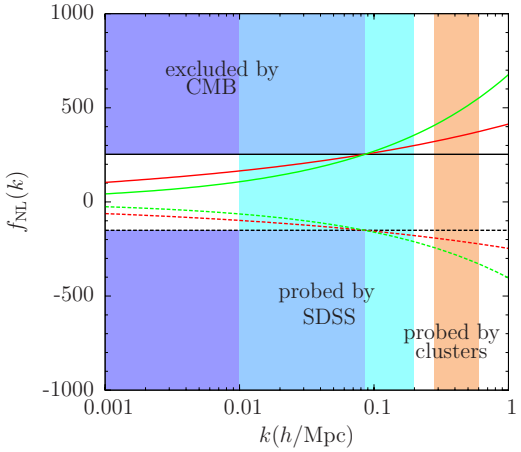

Figure 2.5: The scale dependence of the NG parameter $f_{\rm NL}$ for the models with equilateral shape considered in this work. Results for two different choices of the pivoting value, $f_{\rm NL} = -151$ and $f_{\rm NL} = 253$, are shown by dashed and solid curves, respectively. Different values for the slope α have also been used: $\alpha = 0$ (black lines), $\alpha = -0.1$ (red lines) and $\alpha = -0.2$ (green lines). The shaded regions on the right show the scales probed by the SDSS (cyan) and the galaxy clusters (orange), while the blue region refers to the range excluded at 95 per cent confidence level by the CMB data (Komatsu et al., 2008).

Komatsu et al., 2008). It is evident from the plot that, with this assumption for the NG scale-dependence relation, the absolute value of $f_{\rm NL}$ at the scales relevant for the halo formation can be a factor 2-3 larger than the maximum amount directly derived from the CMB analysis: this can amplify the possible effects of primordial NG.
In Fig. 2.6 we show, as a function of the scale R, $\mu_3(M)$ and the normalized skewness $S_3(M) = \mu_3(M)/\sigma^4(M)$, for models with both local and equilateral shapes. Both skewness parameters are given per unit NG parameter $f_{\rm NL}$; for the equilateral case we also consider the possibility of scale-dependence for the NG term. As already shown by Lo Verde et al. (2008), the two classes of models give quite different predictions for both the amplitude and the mass dependence of the two considered quantities, but this difference decreases as the mass scale increases, since the local and the equilateral cases become more and more similar. The scale-dependence of $f_{\rm NL}$ strongly affects the NG contribution for the smaller masses scales and this effect grows when higher negative α parameters are assumed.

2.4.1 The statistics of the collapsed object for non-Gaussian initial conditions

The building of a suitable formalism describing the formation of DM halos starting by non-Gaussian initial conditions involve some difficulties. In fact, the same method used in the Gaussian case can not be applied because an analytic espression for the conditional probability distribution has not been developed yet. But other techinques (Jedamzik, 1995; Nagashima & Gouda, 1997; Lee & Shandarin, 1998) might also be useful. In what follows, we will descride the analytic approach provided by Matarrese et al. (2000), but another similar treatments has been proposed in literature (e.g. Lo Verde et al., 2008) and, recently, numerical simulations (Dalal et al., 2008; Desjacques et al., 2008; Pillepich et al., 2008) have allowed to improve the analytic expression derived for the mass function of the DM halos.
Given the probability distribution for the smoothed field, it follows that the probability $P[> \delta_c(z), M]$ for a point to belong to a collapsed object at a fixed time is

$$\begin{aligned} P[> \delta_c(z), M] &= \int_{\delta_c(z)}^{\infty} {\rm d}\delta_r \, P[\delta_f(M)] \\ &= \int_{\delta_c(z)}^{\infty} {\rm d}\delta_f(M) \int_{-\infty}^{\infty} \frac{{\rm d}\lambda}{2\pi} \exp[-i\lambda\delta_f(M) + \mathcal{W}(\lambda)] \; . \end{aligned} \tag{2.69}$$

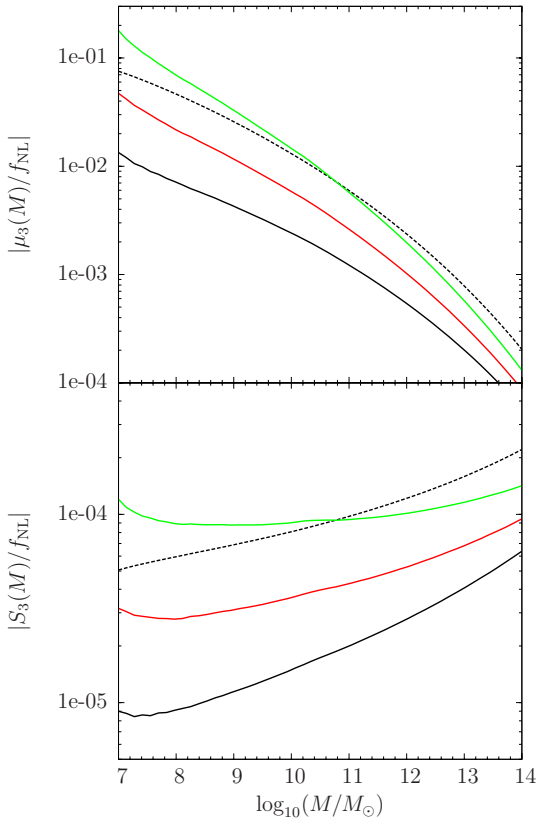

Figure 2.6: The skewness μ_3 (top panel) and the normalized skewness S_3 (bottom panel), given per unit $f_{\rm NL}$. The black dashed curve refers to the model with local shape, while the coloured solid curves present the results for the equilateral configuration with $\alpha = 0, -0.1, -0.2$ (black, red and green lines, respectively).

Neglecting the momenta of order higher than 3, the above integral can be solved analitycally only if $\delta_c(z) \geq 1/S_3(M)$, i.e. $R(M) \leq 10$ Mpc, at the linear order in $f_{\rm NL}$, leading to

$$P[> \delta_c(z), M] \approx \frac{1}{\sqrt{2\pi}} \frac{\sigma(M)}{\delta_c(z)} \exp\left[-\frac{1}{2} \frac{\delta_c(z)^2}{\sigma^2(M)} \left(1 - \frac{S_3(R)}{3} \delta_c(z) \right) \right] \tag{2.70}$$

while in the other cases $P(> \delta_c(z), M)$ can be estimated only through numerical approaches. As a consequence, the mass function $n(M, z)$ can be obtained as

$$n(M, z) = f \frac{\bar{\rho}_{0,m}}{M} \left| \frac{{\rm d}P[> \delta_c(z), M]}{{\rm d}M} \right| , \tag{2.71}$$

when we fixed $f = 2$ as in the Gaussian model, in case of mildly NG. Grossi et al. (2007) and Grossi et al. (2009) show that $n(M, z)$ can be written adding a NG correction to the Gaussian mass function, namely $n_{\rm NG}(M, z) = C_{\rm NG}(M, z) n_{\rm G}(M, z)$, where the correction $f_{\rm NL}$ is

$$C_{\rm NG}(M, z) \simeq \left| \left[\frac{1}{6} \frac{\delta_c^2(z)}{\delta_*(z)} \frac{{\rm d}S_3(M)}{{\rm d}\ln\sigma(M)} + \frac{\delta_*(z)}{\delta_c(z)} \right] \right| \exp\left[\frac{\delta_c^3(z) S_3}{6\sigma^2(M)} \right] . \tag{2.72}$$

In the previous relation, $\delta_* \equiv \delta_c \sqrt{1 - S_3(M)\delta_c/3}$.
The resulting mass function, shown in terms of ratio with respect to the Gaussian predictions, are shown in Fig. 2.7, for both local and equilateral shapes (upper and lower panels, respectively), fixed $f_{\rm NL}$ to the corresponding values at 95% CL ($f_{\rm NL} = -9, 111$ for the local shape, and $f_{\rm NL} = -151, 253$ for equilateral one). For the purpose of this Thesis, we are interested in investigating the NG effects on the mass function at early epochs, for which we assume $z = 6.5, 9$ and 13. Since the mass density

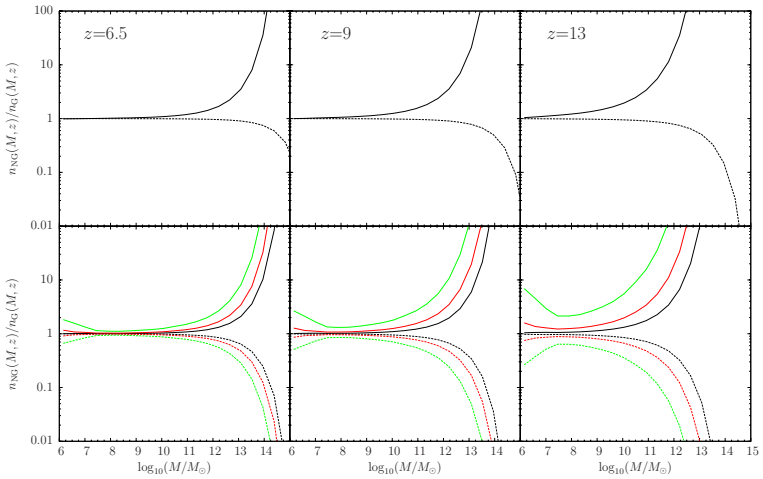

Figure 2.7: The ratio between the dark matter halo mass functions for non-Gaussian and Gaussian models, computed at $z = 6.5$ (left panels), $z = 9$ (central panels) and $z = 13$ (right panels). Top panels show the results for non-Gaussian models with local shape, where $f_{\rm NL} = -9$ (dashed lines) and $f_{\rm NL} = 111$ (solid lines) are assumed. In the bottom panels, which refer to non-Gaussian models with equilateral shape, dashed and solid lines correspond to $f_{\rm NL} = -151, 253$, respectively; black, red and green lines refer to $\alpha = 0$ (i.e. no scale-dependence), $\alpha = -0.1$ and $\alpha = -0.2$ respectively.

probability function is positively skewed in case of positive ($f_{\rm NL} > 0$) NG contributions, the probability of overcoming the collapse threshold becomes higher. As a consequence, the formation of high-mass haloes is enhanced and anticipated when $f_{\rm NL} > 0$, also by a factor of 10 at $z = 13$ for haloes with mass $M \sim 10^{11} M_\odot$ when compared to the standard scenario. We should, however, remark that high-mass haloes ($M > 10^9 M_\odot$) at early cosmological epochs are rare events, as shown also by the small number density at $z = 13$ in the reference case, $n(> 10^9 M_\odot) \lesssim 5 \times 10^{-3}/{\rm Mpc}^3$. Unlike the local model, the scale dependence of NG increases the abundance of the low-mass haloes by a factor of ~ 10 at $z = 13$ when compared to the standard case. The opposite applies for $f_{\rm NL} < 0$. As already noticed by Matarrese et al. (2000) (see also Verde et al., 2001; Grossi et al., 2007), this effect is more evident at early cosmological epochs.
As a concluding remark, we should stress that, given the difficulty introduced by non-Gaussian initial conditions, at the moment an analytic formula for the conditional probability distribution is not avalaible and, as a consequence, a formalism to infer the merger rate has not been developed yet.

2.5 The current status of observations

The statistical distribution of the matter perturbations is fully represented by its power spectrum and the related parameters, i.e. the amplitude (parameterized by σ_8) and the spectral index, that can be constrained through the observations.

A first estimate of σ_8 and n is provided by the power spectrum of the high-z QSO (Viel et al., 2004; McDonald et al., 2005; Seljak et al., 2005; Desjacques & Nusser, 2005), since the Lyα forest can probe the distribution of the matter on small scale, although this relation has still to be deeply investigated. Anyway, the comparison between the observational results of Kim et al. (2007) and the simulations of Bolton & Haehnelt (2007a) suggests a isothermal profile for the IGM $T - \delta$ relation. This allows to achieve a small value for the cosmic variance on $8h^{-1}$Mpc, that is in agreement with the 5-year WMAP estimate showed in Fig. 2.8, $\sigma_8 = 0.796 \pm 0.036$ (Dunkley et al., 2008). A similar result is obtained considering the galaxy clusters, that probe the mass distribution on the large physical scales: $\sigma_8 = 0.77^{+0.07}_{-0.06}$ (Mantz et al., 2008). A different approach consists in observing objects with well-determined distances, such as galaxies and nearby supernovae, to look for deviations from the Hubble flow given by their peculiar motions. The actual resulting variance,

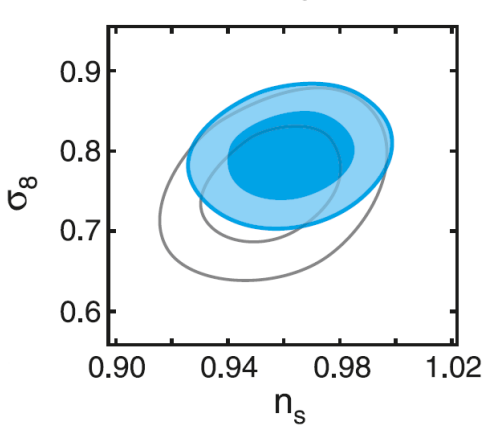

Figure 2.8: Constraints from the spectral parameters provided by 5-year WMAP data (blue), shoved for 68% and 95% CL limits. Parameters are consistent with the 3-year limits (grey lines) from Spergel et al. (2007) (Dunkley et al., 2008).

$\sigma_8 = 0.79 \pm 0.22$ (Gordon et al., 2007) is in good agreement with the other estimates.
Moreover, Fig. 2.8 shows that at the moment, the current data of 5-year WMAP show no evidence for a running spectral index n on the physical scale, preferring a constant $n = 0.963^{+0.014}_{-0.015}$ rather than the scale-invariant Harrison Zel'dovich Peebles spectrum ($n = 1$). Actually, given the large degeneracy between n, $\Omega_{0,b}$ and the electron scattering optical depth τ, more accurate measurement on smaller scales should needed.
For that concerning a possible NG in the initial overdesity field, the CMB observations allow to constrain the NG parameter $f_{\rm NL}$ for both the local and the equilateral shapes. Through the TT-spectrum, even if other methods of investigation like the Minkowski functionals, the last 5-year WMAP data allow a tiny NG degree, i.e. $< 10^{-5}$, involving $-9 < f_{\rm NL}^{loc} < 111$ for the local model and $-151 < f_{\rm NL}^{equi} < 253$, measured on the $k_{\rm CMB}$ scale of $0.086h/\,{\rm Mpc}$ ($\sim \ell = 700$) assuming the equilateral shape, at 95% CL. Similar results is found by Slosar et al. (2008), investigating the distribution of the quasars sample in the SDSS. The NG parameter lies between $-31 < f_{\rm NL} < 70$ at 95%CL when the local model is considered.
As a final remark , we should mention that, as already specified in the previous chapter, the cosmological background assumed in this work is consistent with the WMAP predictions for the 1-year and the 5-year of observations. Unlike the geometrical parameters, the predicted structure formation scenario differ mainly due to the higher value for σ_8 found by 1-year WMAP, i.e. $\sigma_8 = 0.9$, that however cannot affect the conclusions of this work.

Chapter 3

The cosmic reionization

In this chapter, the main theoretical and observational sides related to the way in which the first stars ionize the gas are illustrated, describing the main stages of the ionization history of the IGM that lead to the still unknown reionization process.
The post-inflation phase consists in the 'Dark Age', the cosmological era between the time when the CMB was emitted and the time when the evolution of structures in the universe led to the gravitational collapse of objects in which the first stars were formed. The evolution of the universe during this phase is still unknown because of the lack of information provided by the sources of light and only the formation of the first collapsed objects ends this unknown stage. The following collapse of the gas inside the potential wells of the DM halos gives rise to structures with a typical virial mass $M_v = M(T \leq 10^4)$ K, corresponding to the cooling temperature $T_{\rm cool}$ of the neutral hydrogen HI. The collapse of HI, that is mostly present in the coolant gas disguised as H_2 molecules, ignites the star formation, with the subsequent release of light that can ionize the HI in the neighbouring IGM. This is the first stage of the reionization process, that marks the end of the dark age in which all the HI in the IGM is at the neutral state. Its name is to distinguish it from the first ionization phase, occurring at the beginning of the history of the universe caused by its high temperature. The effects of HI photoionization are significant for the following formation of the structure, since the ionization of the IGM should prevent the cooling of the gas, destroying the small mass DM halos, preventing the following star formation and affecting the chemical composition of the first sources of light.

3.1 The propagation of the ionization front

The aim of this section is to describe the way in which a source of light acts on the IGM, through an analytic method. Actually, the effective ionization history of the HI strongly depends on many other physical phenomena as the feedback or the photoevaporation of minihalos (i.e. halos with masses $\lesssim 10^6$ $M_\odot$), that could be investigated only through numerical simulations because of the lack of an efficient analytic formalism for the description of their effects. Finally, the following discussion, inspired to Loeb (2006), can apply to different types of source, given its parametric nature representing the ionization action on the IGM.
Let suppose that a given source of light can ionize a region of comoving volume V such that the inner hydrogen is fully ionized (HII) and the outer gas is neutral. The size of such region indeed depends on the ionization efficiency of the inner source, represented by the free parameter ζ containing all its peculiarities, as discussed later. As an example, the efficiency ζ related to a star is indeed lower than that of a galaxy, hence the ionizing photons can be absorbed also by the tiny layers near the source and the typical size of the ionized volume V is smaller.
Once emitted by the collapsed object, the ionization front (I-front) goes far from the source, loosing the photons that are absorbed by the crossed HI. Indeed, the total number of lost photons becomes higher and higher as long as the distance between the I-front and the source increases, until the ionizing flux is fully absorbed by the neutral IGM. At the space point in which that occurs, the abrupt transition between ionized and neutral gas marks the maximum size reached by the HII volume, since the following emitted I-fronts can just mantain the ionized state inside the region,

that, without the external action of the source, would come back to the neutral phase. Then, when the maximum size is reached the HII region is at the ionization equilibrium, i.e. the recombination and the ionization rates are equal:

$$\alpha\langle n_{\rm H}^2(t)\rangle V_p = \frac{{\rm d}N_\gamma}{{\rm d}t} \ , \tag{3.1}$$

where the left-hand term is the recombination rate, in which α represents the recombination coefficient dependent on the physics of HI, $n_{\rm H}$ is the local density of hydrogen and V_p is the proper volume of the ionized region. The right-hand side is the ionization rate, with N_γ representing the total number of ionizing photons required to once ionize the inner HI, so that $N_{\rm HII} = N_\gamma$, and is related to the ionization efficiency. In Eq. (3.1), the square of the local density shows that the IGM is not uniformly distributed and that the recombination time is very short. This is usually dealt through the introduction of the clumping factor $C_{\rm HII}$, that represents the compactness degree of the IGM and is defined as $C_{\rm HII} = \langle n_H^2\rangle/\langle n_H\rangle^2$, that usually varies with time. Hence, the general evolution of the HII region in proper coordinates is given by (Loeb, 2006)

$$\langle n_{\rm H}(t)\rangle\Big(\frac{{\rm d}V_p}{{\rm d}t} - 3H(t)V_p\Big) = \frac{{\rm d}N_\gamma}{{\rm d}t} - \alpha C_{\rm HII}\langle n_{\rm H}^2(t)\rangle V_p \ , \tag{3.2}$$

where in the left-hand side ${\rm d}V_p/{\rm d}t$ represent the total growth of the region due to both the I-front and the expansion of the universe, given by $H(t)$. The righ-hand term shows the contributions of the ionization and the recombination processes. Translating to the comoving reference frame, Eq. (3.2) becomes

$$\frac{{\rm d}V}{{\rm d}t} = \frac{1}{\langle n_{\rm H,0}\rangle}\frac{{\rm d}N_\gamma}{{\rm d}t} - \alpha\frac{C_{\rm HII}}{a^3}\langle n_{\rm H,0}\rangle V \ , \tag{3.3}$$

in which $\langle n_{\rm H,0}\rangle$ is the mean present-day density of H, i.e. $\langle n_{\rm H,0}\rangle = 1.88\times10^{-7}\Omega_{b,0}h^2/0.022$ cm^{-3}, that is a factor ~ 0.76 lower with respect to the number density of the baryons at $z = 0$. Shapiro & Giroux (1987) found the following general solution to Eq. (3.2) for a source which turns on at a given time t_i:

$$V(t) = \int_{t_i}^{t}\frac{1}{\langle n_{\rm H,0}\rangle}\frac{{\rm d}N_\gamma}{{\rm d}t'}\exp[F(t,t')]\,{\rm d}t' \ , \tag{3.4}$$

where

$$F(t,t') = -\alpha\langle n_{\rm H,0}\rangle\int_{t'}^{t}\frac{C_{\rm HII}(t'')}{a^3(t'')}\,{\rm d}t'', \tag{3.5}$$

that in case of a ΛCDM flat cosmology and assuming a constant clumping factor, becomes (Loeb, 2006)

$$F(t',t) = -\frac{2}{3}\frac{\alpha n_{\rm H,0}}{\sqrt{\Omega_m}H_0}C_{\rm HII}[f(t') - f(t)] \ , \tag{3.6}$$

setting $f(t) = \sqrt{1/a^3 + 1/\Omega_m - 1}$. Actually, the IGM recombination is for its nature related to the local density of the HI, then the equation above results to be a strong simplification. An accurate investigatation of the evolution of the HII bubbles is possible only through semi-numerical or numerical methods (Iliev et al., 2007; Lidz et al., 2007; Iliev et al., 2008b; Choudhury et al., 2008), that allow to know the actual spatial distribution of the matter density field.
At the reionization equilibrium, the maximum size of the HII bubble R_S can be obtained through Eq. (3.3) setting ${\rm d}V/{\rm d}t = 0$ and results

$$R_S = \Big(\frac{3}{4\pi}\frac{1}{\langle n_{\rm H,0}\rangle^2}\frac{{\rm d}N_\gamma}{{\rm d}t}\frac{a^3}{\alpha C_{\rm HII}}\Big)^{1/3} \ , \tag{3.7}$$

representing the comoving Strömgren radius. As already stressed, its dimension is related to the physical properties of the source responsible for the production of the I-front. In fact, the amount of the ionizing photons N_γ can be related to the escape fraction $f_{\rm esc}$, the star formation efficiency f_*, the number of ionizing photons produced per baryon in stars $N_{\gamma/b}$ and $N_{\rm rec}$ the typical number of times a hydrogen atom has recombined. Fixed the ionization efficiency of the galaxy as

$$\zeta = f_{\rm esc}f_*N_{\gamma/b}N_{\rm rec}^{-1} \ , \tag{3.8}$$

that is an estimate of the amount of ionizing photons occuring to ionize a HI atom, the total number of the ionized HI corresponds to $N_{\rm HII} = N_\gamma = \zeta M_{\rm s}/m_{\rm H}$ where $M_{\rm s}$ is the mass of the source. Assuming that the host halo of the galaxy has a mass M and a baryon fraction Ω_b/Ω_m, the total mass $M_{\rm HII}$ ionized can be written as

$$M_{\rm HI} = N_{\rm HII} m_{\rm H} = \zeta M_{\rm s} = \zeta \left(M \frac{\Omega_b}{\Omega_m} \right) , \tag{3.9}$$

where in the right-hand term $M\Omega_b/\Omega_m$ is the mass of the galaxy. The actual radius never reaches this size if the recombination time is shorter than the lifetime of the galaxy, as pointed out by Loeb (2006). Given their dependence on the parameters related to the source, Eq. (3.8) and (3.9) show that the typical size of the HII region is determined by the type of the ionizing object considered. In particular, the equilibrium scale can be analytically estimated under the assumptions of a suitable model for the IGM recombination and through the observational constraints on ζ. As an example, Loeb (2006) show that the radius R_S does not change meaningfully when a star-like and a mini-quasar-like source are considered, suggesting that the typical size may be < 10 (comoving) Mpc. Although having almost the same ionization front, a higher maximum radius has been found for the quasar-like sources, since the ionizing photons around a transient object expands at nearly the speed of light at early time, when the size of the HII region is small and the effect of the recombination is negligible. White et al. (2003) derived an analytic espression for the evolution of the comoving radius of the ionized region produced by quasars (Loeb, 2006), but the actual size can be inferred by the spectral gap between the quasar rest-frame Lyα wavelength and the beginning of Lyα absorption. Existing data from the SDSS (Mesinger & Haiman, 2004a; Wyithe & Loeb, 2004; Wyithe et al., 2005a) probe a physical $R_S \sim 6$ Mpc for QSO at $z > 6$, i.e. a comoving $R_S \gtrsim 30$ Mpc. On the other hand, the nature of the reionization front changes significantly when considering the effects of the X-ray background, for which the hard component has a typical mean free path (mfp hereafter) similar to the horizon scale and then is rarely absorbed, while the soft rays can ionize the IGM in a quite homogeneous manner.

3.2 The phases of HI reionization

This section summarizes the different phases of the HI reionization. Although in this work the IGM will be identified only with HI since it represents its main component, a brief discussion will be here treated separately to recall the reionization scenario associated to the helium (He) component, that is generally very different.
The recent numerical simulations show that reionization is an 'inside-out' process, that begins in the high-density regions of the IGM and then expands into the lower dense ones, through the following main stages (Gnedin, 2000b), illustred in Fig. 3.1.

The pre-overlap stage

This is the initial phase of reionization. The first galaxies form in the most massive halos at high redshifts, that are located in the highest density peaks of the overdensity fields and as a consequence are biased. Hence, when the galaxy turns on, the escaping ionizing photons impact the surrounding high-density neutral IGM, characterized by a high recombination rate, and are partially absorbed. The surviving photons can propagate into the low-density regions, and easily ionize it, increasing the size of the HII region. This process occurs until the emitted I-front has enough photons surviving to recombination, reaching the maximun radius and leaving inside some high-density pockets of neutral gas. Furthermore, the inner ionization intensity of a bubble is very inhomogeneous, since it is related to the luminosity and the distance of the source itself.
During this period, the IGM is a two-phase medium characterized by isolated HII bubbles lying in the neutral background sea, as shown in Fig. 3.1, bottom panel A.

The overlap stage

This central phase is expected to occur rapidly, at z lower than the initial stage, due to the growth of sufficiently near HII bubbles that could overlap, giving rise to a unique larger ionized region.

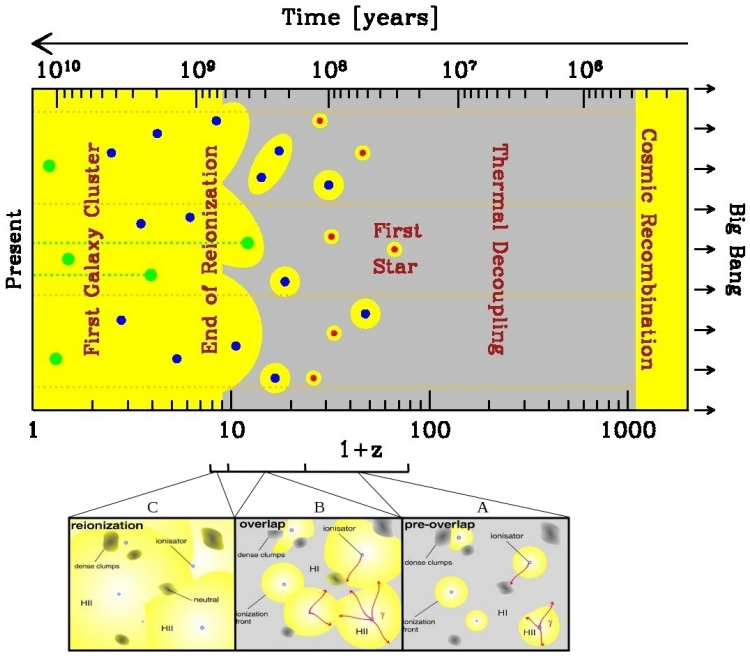

Figure 3.1: The expected time-evolution of the HI reionization process (top panel), in which a more detailed view of the bubble evolution (bottom panels) is shown. Panel A refers to the pre-overlap phase, when the bubble are mostly disjoined and can expand in the lower dense IGM, leaving pockets of high-density gas. The following stages are represented by the overlap phase illustrated in panel B, when neighboring HII regions begin to overlap and can ionize the dense IGM clumps, and the completion of reionization (panel C), in which the gas is almost fully ionized (Loeb, 2006).

When two (or more) bubbles are joined, their inner HI atoms suffer of the exposure to two (or more) different ionizing fronts, hence the inner ionizing intensity increases, allowing to the new ionized region to expand also in the high-density clumps previously recombined fast enough to stay neutral. Since the overlapping of the HII regions increases the I-fronts with a subsequent acceleration of the reionization process, this stage results just in a phase transition and is expected to occurs rapidly. Another point in favour to this rapid evolution is related to the increasing formation of the collapsed objects, that enhances the production of ionizing photons. The outcoming scenario is consistent with a much higher and homogeneous ionization intensity, allowing most regions of IGM to see several unobscured sources as shown in Fig.3.1 (bottom panel B). Anyway, some high-density self-shielded clouds still remain neutral.

The epoch of reionization

This stage marks the end of the previous phase at the moment in which the IGM reionization is complete, but its exact 'time position' depends on the 'complete' meaning. A possible definition could be related to the redshift at which the mfp of the ionization photons is comparable to the Hubble radius. A more practical assumption in observational terms corresponds to the epoch in which the ionizing filling factor $Q_i \ll 10^{-3}$. After this step, shown in Fig.3.1 (bottom panel C), most of the IGM in the universe will be ionized, but the high-density structures as the Lyman systems in absorption at low z that could prevent the visibility of galaxies in a wide range of z.

The post-overlap stage

This stage follows the complete reionization, where the high-density clumps at low z are gradually ionized due to the increase of the galaxy density and the I-front becomes more and more uniform. This phase goes on indefinitely, since the formation of the collapsed object produces neutral gas through the HI cooling even in the present universe. However, the IGM history reaches another

milestone at $z \sim 1.6$, i.e. the breakthrough redshift, the epoch in which all the galaxies are visible to each other.

The different phases of reionization can be described through a statistical analysis of the time evolution of the IGM ionized filling factor Q_i, representing the volume filled up by the ionized bubbles. In general it differs from the sum of the total number of the HII bubbles times their corresponding volume, $\bar{x}_i$, since in this case the possible overlap of the regions could overestimate the total ionized volume of the universe. Anyway, the linearity of the physics means that $\bar{x}_i$ can represent a good approximation to Q_i till the end of the overlap phase. Eq. (3.3) can lead to an analytical rough estimate of the filling factor, under the assumption that the recombination is homogeneous, i.e. C_{HII} does not depends on the topology of the sources. In this case, we can sum all the $\mathrm{d}V/\mathrm{d}t$ terms inside a large enough region of the universe, and then divide for the volume V_{tot} of such a region. Then, Eq. (3.3) that describes the individual properties of a single HII region can be converted in a more general equation describing the transition from a neutral to a fully ionized IGM:

$$\frac{\mathrm{d}Q_i}{\mathrm{d}t} = \frac{1}{\langle n_{\mathrm{H},0}\rangle}\frac{1}{V_{\mathrm{tot}}}\frac{\mathrm{d}N_\gamma}{\mathrm{d}t} - \alpha\frac{C_{\mathrm{HII}}}{a^3}\langle n_{\mathrm{H},0}\rangle Q_i \tag{3.10}$$

$$= \frac{\zeta}{x_H}\frac{\mathrm{d}F_{\mathrm{coll}}}{\mathrm{d}t} - \alpha\frac{C_{\mathrm{HII}}}{a^3}\langle n_{\mathrm{H},0}\rangle Q_i \ , \tag{3.11}$$

where $N_\gamma = \sum N_\gamma(M) = \sum \zeta(M\Omega_b/\Omega_m)$ is the total number of ionizing photons inside V_{tot}, that is the sum of the contributions of the single ionizing sources. The solution can be found analogously to Eq. (3.4):

$$Q_i(t) = \int_0^t \frac{\zeta}{x_{\mathrm{H}}}\frac{\mathrm{d}F_{\mathrm{coll}}}{\mathrm{d}t'}\exp[F(t,t')]\,\mathrm{d}t' \ , \tag{3.12}$$

in which F_{coll} is the inner total collapsed fraction, that can be easily estimated by the volume fraction occupied by the DM halos in which the HI cooling is efficient. Under the assumption that the main coolant is the atomic hydrogen, the minimum virial mass required to form a galaxy corresponds to the temperature $T = 10^4$ K. The above equation allows to investigate the time evolution of the ionized fraction of the universe once fixed the parameters related to the sources leading reionization and the IGM clumping factor, that are at the moment still unclear. The actual uncertainties about the star formation efficiency or the escape fraction could heavily affect the predictions for the reionization scenario. On the other hand, also additional phenomena like feedback or galactic winds can reduce the star formation inside the galaxy, and the photoionization due to the radiation of the first sources could prevent the growth of the low-mass halos and the mini-quasars. Another important question is related to the description of the clumpiness of the IGM, previously assumed as homogeneous. Actually, as already stressed, the clumping factor is strongly dependent on the local density of the ionized volume and the topology of the matter fluctuations. Furthermore, the ionizing source usually forms in the highest density peaks and the IGM clumping is affected by the correlation source-IGM density. The importance of considering a realistic description for the clumping factor lies in the fact that regions of lower densities will be ionized first, while the high-density regions remain neutral for more time.
These several additional aspects can be investigated in an appropriate manner only through numerical simulations, but a rough picture can be provided by the semi-analytic models, that furnish an analitycal description for the probability distribution of the gas $P(\Delta)$. In this approach, fixed Δ_i as the ionization threshold such that the gas with $\Delta \leq \Delta_i$ is ionized (Miralda-Escudé et al., 2000), the clumpig factor can be espressed as

$$C_{\mathrm{HII}} = \int_0^{\Delta_i} P(\Delta)\Delta^2\,\mathrm{d}\Delta \ , \tag{3.13}$$

that roughly introduces the inhomogeneous recombination of the IGM. Furthermore, Eq. (3.10) suffers of the lack of a suitable description for the clustering of the sources. Since the galaxies form in the highest density regions, the overlap of the bubbles and hence the morphology of the ionized regions would be determined by the clustering pattern. If the correlation between the sources is not considered, the size of the HII bubble can substantially underestimated. Anyway, to build a good

model for the clustering of the source, we need to know the physical location of the DM halos at the considered cosmological epoch, that is possible only making maps of DM halos through numerical approaches. The important result that can be drawn from such an analysis is that reionization is an inhomogeneous process, since the overlap of the bubbles located in different regions of the universe should complete at different times, following the background density inhomogeneities of such regions.

3.2.1 The He reionization

Although the main component of the universe is constitued by HI, a small ($Y \sim 0.24$) fraction is represented by He that, analogously to the neutral hydrogen, suffers of the ionization action of the first sources of light. The main difference between these two chemical species consists in the fact that He, irrespective of HI, is characterized by two level of energy and hence the complete reionization scenario is more complex.
The sources that can ionize the HI can also produce singly ionized helium (HeII) by the emission of photons with characteristic energy $E \geq 24.6$ eV. Then, since the ionization and recombination actions on HeI are similar to those for HI, the HeII reionization history roughly follows that of HI. On the other hand, the second ionization of HeI requires more energetic photons with $E \geq 54.4$ eV and its recombination rate is $\gtrapprox 5.5$ times faster that that of HII. This implies that for both stellar (Venkatesan et al., 2003) and quasar (Wyithe & Loeb, 2003; Madau et al., 2004; Ricotti & Ostriker, 2004b) sources, or for thermal emission resulting from the shocks of collapsing structures (Miniati et al., 2004), the epoch of complete reionization of HeI occurs later than that for the neutral hydrogen. It follows that the epoch in which HeI is fully ionized can be more easily probed by observational tests at low z. Then, unlike HI and HeI, the HeII reionization shall be treated separately from the other two species.
The imprinting of the He absorption is evident in the low (i.e. $2.4 < z < 3.2$) z QSO spectra (see Heap et al., 2000, for an example) corresponding to the HeII Lyα line $\lambda = 304$ Å. The HeII Lyα absorption is generally stronger than the HI absorption in the same wavelength by a factor $\eta = N(HeII)/N(HI)$, due to the difficult complete ionization of He, despite its small density with respect HI. These results are supported by theoretical investigations (Wyithe & Loeb, 2003; Gleser et al., 2005; Paschos et al., 2007; Furlanetto & Oh, 2008a,b), that predict an epoch of complete ionization at $z < 5$, after the HI reionization. In particular, the QSO population present at $z \sim 3$ is sufficient to ionize the IGM at epochs before $z_{\rm He,reion} \approx 3$, although this estimate is affected by the physics assumed for the gas. On the other hand, recent numerical simulations (Venkatesan et al., 2003; Ricotti & Ostriker, 2004b) suggest a possible double reionization scenario for HeII, in which the contribution to high energy photons can be so significant to produce a first HeII reionization at high z (toghether HI), provided by PopIII stars and high-z QSO, and a second complete ionization at lower redshifts driven by the known population of QSO.
Other indirect probes to the HeI reionization have been provided by Songaila & Cowie (1996); Songaila (1998), that found a rapid increase in the Si^4/C^4 ratio with decreasing redshift at $z = 3$, probably due to the sudden hardening below $z = 3$. Furthermore, also the IGM temperature can be a strong observational constraint in this direction. In fact, while HI reionization can heat the gas to $T \sim 10^4$K, during HeI reionization $T_{\rm IGM}$ can rise to $\approx 2 \times 10^4$K.

3.3 The sources of reionization

The nature of sources responsible for reionization is still debated. Although most theoretical scenarios assume stellar-type sources, other contributions can meaningfully affect the reionization scenario. In this section we will review the possible ionization sources and their impact on the IGM. The most common sources studied are the ones that produce UV photons, i.e. photons with energies larger than 13.6 eV but within few tens of eV. These photons can ionize and heat HI and, possibly, He. At high (i.e. > 2) z the mfp of the UV photons becomes small due to the large value of the photoionization cross section for $E = 13.6$ eV, the rapid increase of the radiation absorbers and the attenuation of the possible source at high z. The radiation is then largely "local".

3.3.1 The stellar-type sources

The most studied reionization scenario in literature is that driven by stellar sources, which needs several assumptions for the star spectra and their Initial Mass function (IMF) that should be taken in agreement with the observational tests, described in the next section. As shown by Hui & Haiman (2003), a simple reionization scenario in which the IGM becomes ionized early and remains so thereafter is ruled out by the low-z temperature of the IGM. Then, the most accepted scenario outgoing from the last simulations is that HI suffers of two different ionizations, at an earlier and a later epoch. Its first reionization should be provided by the PopIII stars, metal-free objects characterized by a high production of photons and/or escape fraction. These objects form at $z \approx 30$ in DM halos characterized by a Jeans mass $M_J < 10^5$ $M_\odot$, corresponding to a virial temperature $T < 10^4$ K and can enhance the ionization of molecular hydrogen H_2, inhibiting the growth of smaller objects. In fact, as argued by Ciardi et al. (1998), these stars can produce a soft-UV background intensity of $J_{SUV} = 10^{-30} - 10^{-26}$ erg/cm^2/s/Hz that could be able to penetrate the high density clouds and, through the photodissociation of the molecular hydrogen, prevents the formation of the collapsed structures. As pointed out by Venkatesan et al. (2003), these objects have an unusually hard spectra that could be able to ionize HI and HeII at $z \sim 9$ and 5.1 for continuous scenarios of star formation.
Actually, the contribution of the very massive metal-pure first stars is nowadays uncertain, since the metallicity of the IGM should rapidly increase due to the action of the radiation, producing an early Pop III-Pop II transition (Rozas et al., 2005; Fang & Cen, 2004). The contribution of small-mass Pop III stars can be instead important, since their formation would stop at lower z (Schneider et al., 2006). Another scenario is provided by Trenti & Stiavelli (2009), that obtain a significant contribution from Pop III stars only through a high formation of collapsed objects in a single halo.
The following metal enrichment of the IGM causes the disappearence of Pop III stars and the production of photons drops, giving rise to a partial/total recombination of the IGM. A second reionization can hence occur when more standard source appears, as Pop II stars or QSO. The Pop II transition occurs when the metallicity of the stars becomes $Z = 10^{-4} Z_\odot$ as pointed by Schneider et al. (2002), but anyway a suitable modelling of this process requires a knowledge about many physical parameters that are not yet well understood, as the time of switch-off (Venkatesan et al., 2003).

3.3.2 The quasar-like sources

Although the common reionization picture is thought to be driven by stars, a contribution to the UV background is provided also from high-z QSO (Zaroubi et al., 2007; Ripamonti et al., 2008; Thomas & Zaroubi, 2008) due to their higher luminosity and escape fraction. As an example, the mini-quasars powered by intermediate-mass black holes remnant of the first stellar sources, could produce a significant amount of ionizing photons at $z > 15$ (Madau et al., 2004). Furthermore, recent observational probes suggest that the role of QSO could be crucial for the complete He reionization, that should be occured at $z \approx 3.5$, as estimated through the quasar spectra.
Anyway, their effective contribution is still uncertain. In fact, the recombination rate of the IGM becomes higher as the redshift and the luminosity of the source increase, reducing the effective contribution to the total reionization process. Furthermore, the relatively short lifetime of the QSO should prevent the growth of their surrounding HII bubble. Another crucial point is related to their abundance. The recent observations of the Lyα forest and the quasar luminosity function at redshifts $z > 6$, suggest that quasars dominate the production rate of hydrogen ionizing photons only after the Universe has aged by 1-2 billion years. The sharp decline in the observed comoving density of bright quasars at redshifts $z \geq 3$ implies that supermassive BHs could have produced sufficient UV photons to reionize cosmic hydrogen only at low z (Loeb, 2008).
As discussed by Loeb (2006), if the quasar contribution to the ionizing intensity during reionization is considered, several phases of the IGM evolution are modified with respect to the pure stellar case. In fact, the hard photons produced by a QSO can go deeper into the surrounding neutral clumps, with the consequent easy propagation of the ionization front and the increase of the ionized filling factor. Finally, their X radiation can catalize the formation of the H_2 molecule resulting in an enhanced star formation also in small massive halos.

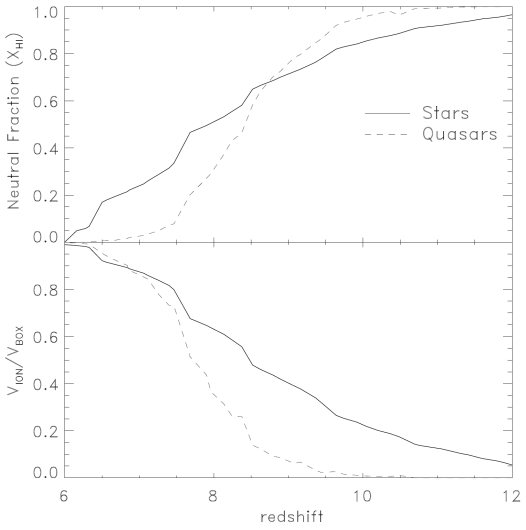

Figure 3.2: The history of reionization is here shown in terms of the volume averaged mean neutral fraction (top panel) and the ionized volume fraction (bottom panel) in the simulation box as a function of redshift, driven by stars (solid line) and quasar (dashed line) populations (Thomas & Zaroubi, 2008).

The contribution of stellar and QSO sources to the ionized fraction of the universe has been investigated by Thomas & Zaroubi (2008), in Fig. 3.2. Here, the top panel shows the mean neutral fraction left after the ionization of the source at several cosmological epochs, while the corresponding volume fraction filled by the HII regions is represented in the bottom panel. Although both the populations ionize the entire box by $z = 6$, the ionization history follows very different paths. Indeed, the star ionization starts much earlier than the quasars, but the rate at which they ionize is low. Then, the QSO population can ionize the IGM earlier than stars, but their effect can be seen only later.

3.3.3 The X-ray background radiation

This possible source of reionization could contribute in a significant way to the IGM reionization. This background radiation could come from early quasars or mini-quasars generated by the collapse of the first star population, but also by the thermal emission of the SN remnants, the inverse Compton scattering of soft photons during the supernova explosion (Oh, 2001; Madau et al., 2004; Ricotti & Ostriker, 2004b) or by starburst galaxies. As the typical mfp of X-ray is larger than the radiation of stars and their escape fraction is larger, they could be suitable candidates for reionization.
The major contribution to reionization is provided by the soft-X component, i.e. rays with energy $E < 2$ keV, that suitably redshifted can generate UV radiation able to ionize the IGM. The typical mfp of this radiation is larger than the separation between collapsed structures (Madau et al., 2004), and this has often motivated the simplifying assumption that they are able to ionize the IGM in a homogeneous manner. Anyway, these photons can only partially ionize the IGM through secondary ionizations. In fact the electron produced by the primary ionization is enough energetic (~ 1 keV) to be able to produce few ~ 10 electrons through collisional way. Indeed, this method is less effective in producing ionized atoms when compared to the UV background, then the sources of X-radiation do not dominate the reionization process, but their role is crucial for the temperature history of the IGM.
The soft X-ray background is accompanied by a hard-X component ($E \gtrsim 10$ keV) that would redshift and is observed as a present-day soft X-ray background. Its importance relies on the fact that is a good constraint for the contribution of the X-ray sources to reionization (Pritchard & Furlanetto, 2007), but its typical mfp is comparable to the Hubble scale and then is rarely absorbed.

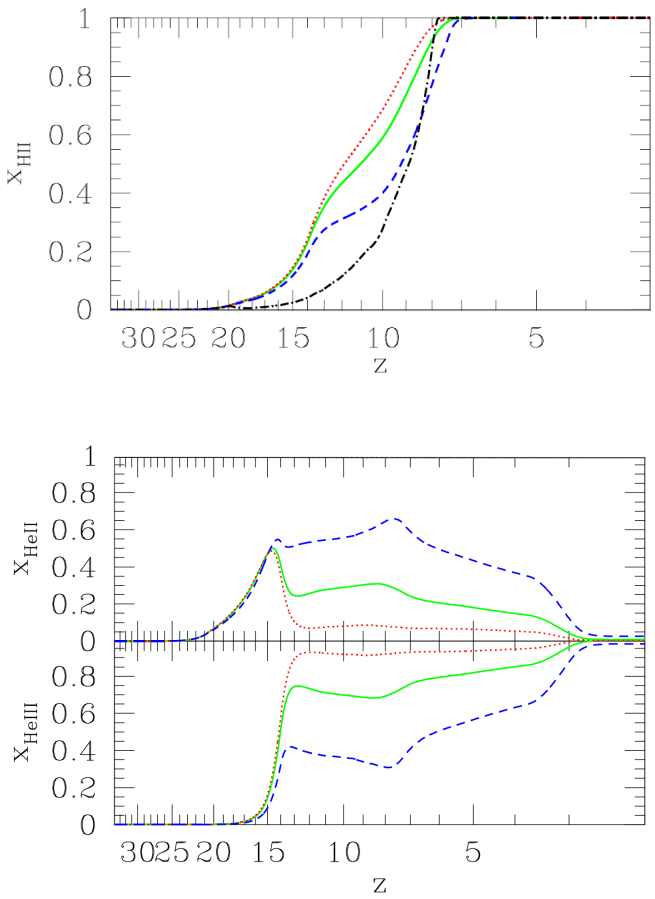

Figure 3.3: The reionization history for HI (top panel) and HeI (bottom panels). The dotted, solid and dashed lines show the ionized H and He fractions for gas overdensities $\delta = 0.1, 1, 10$ in the IGM outside the ionized regions, respectively. After overlap, when the ionising background is uniform, the lines refer to the ionised IGM. In the top panel, the dot-dashed line refers to the time-evolution of the HII volume filling factor (see Ricotti & Ostriker, 2004b, for details).

The reionization scenario driven only by the X-ray sources like mini-QSO has been investigated by Ricotti & Ostriker (2004b) and is illustrated in Fig. 3.3, under the assumption that BHs are powered mostly at $z > 15$. They pointed out that, although the predicted HI ionization history is in agreement with most of the observational tests with a later $z_{\rm reion} \sim 8$, in most of the considered models the redshifted X-ray background can fully reionize HeII at $z \sim 3$ without any additional contribution from quasars at lower redshifts. Anyway, the late preionization model shown in Fig. 3.3 should not be suitable, because it produces an electron optical depth τ_e lower than that predicted by the WMAP results available at the time of investigation. In fact, the high τ_e measured by 1-year WMAP could be consistent only with a more plausible model in which preionization starts at $z \sim 15 - 20$.

3.3.4 The decaying particles

Other possible contributions at high (> 6) z can arise from the decaying particles, but their role is still unclear. In this case, the production of high-energy particle can not be associated to any kind of collapsed source, leading to a quite homogeneous ionization action. While massive neutrinos have been excluded by the results obtained by Spergel et al. (2003), the effect of the decaying ster-

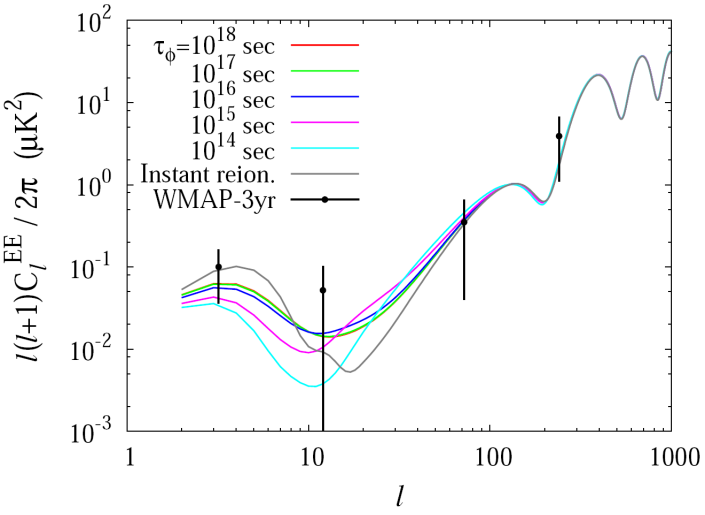

Figure 3.4: The EE power spectra of the 3-year WMAP analysis for a resulting IGM optical depth $\tau = 0.1$, assuming different lifetimes for the decaying particles. Also shown are the spectra for the (one-step) instantaneous reionization, and the three-year WMAP data (Kasuya & Kawasaki, 2007).

ile neutrinos do not violate the constraints imposed by WMAP and the GRB, in agreement with the early reionization scenario predicted by the 1-year WMAP release. Anyway, several authors like Mapelli & Ferrara (2005) conclude that they play a minor role in the ionization history of the IGM.
Actually, the main problem in this kind of investigation is given by the nature of the possible candidates, that is still unknown and has been attributed also to exotic particles as cryptons, gravitinos, DM and DE particles, axinos. Their effects have been investigated by Chen & Kamionkowski (2004), showing that they can produce the early reionization scenario paint by 1-year WMAP, but they would give rise to fluctuations on the CMB temperature-polarization (TE) spectrum which generally violate the currently expected short lifetime of the candidates. On the other hand, the recent later reionization outlined by the more recent CMB data analyses seems to be in agreement with the decay of long-lifetime elements.

A similar result has been obtained also by Kasuya & Kawasaki (2007) (Fig.3.4), showing that long lifetime for decaying particle are not rejected by the current CMB estimates, while Mapelli et al. (2006) show that light dark matter particles (1-10 MeV) and sterile neutrinos (2-8 keV) can be sources of partial early reionization ($z \leq 100$) with a small ($\tau < 0.01$) contribution to the resulting Thompson optical depth with respect the 3-year WMAP data. Their effects on reionization could be at best indirect, acting on the behaviour of the matter temperature and in a possible enhancement of the production of H_2 or HD molecules with repercussions on the following star formation. On the contrary, the contributions of heavy dark matter candidates (gravitinos and neutralinos) on reionization and heating are minimal.

3.3.5 The effect of primordial magnetic field

A possible primordial magnetic field acts on the IGM in many different ways. In the post recombination era, the primordial magnetic field can dissipate its energy into the IGM through the ambipolar diffusion and, on small scales, by generating decaying magnetohydrodynamic (MHD) turbulences, significantly modifying the thermal and ionization histories of the IGM well before the first Pop III stars appear. As pointed out by Sethi & Subramanian (2005), these dissipation effects can give rise to a Thompson optical depth $\tau > 0.1$ when the value of the magnetic field at the present time is $B_0 = 3 \times 10^{-9}$ Gauss smoothed on the magnetic Jeans scale, but not in a suitable redshift range to explain the WMAP results.
Probably, the main effect on reionization of the primordial magnetic field is indirect and related

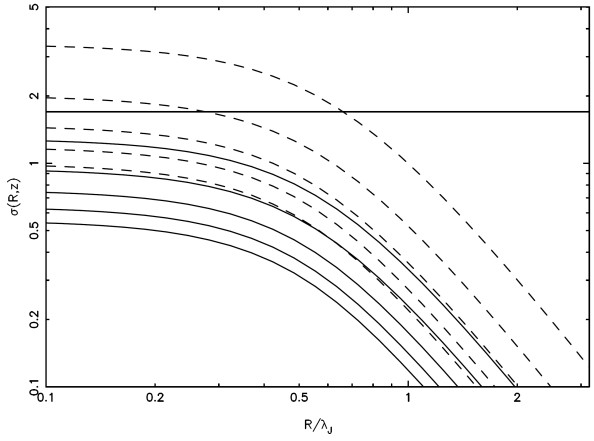

Figure 3.5: The mass dispersion $\sigma(R, z)$ is shown for two models with nearly scale free magnetic field power spectra. The solid and dashed curves correspond to $n_B = -2.9$ and -2.8, respectively. Different curves, from top to bottom, correspond to redshifts $z = 10, 15, 20, 25, 30$, respectively. The horizontal line corresponds to $\sigma = 1.68$ (Sethi & Subramanian, 2005).

to the enhanced structure formation. In fact, if the characteristic amplitude of the field is of the order of nG, it could be shown (Sethi & Subramanian, 2005; Tashiro & Sugiyama, 2006) that the Lorentz force can produce additional density fluctuations of baryons, inducing an earlier structure formation, perhaps Pop III stars, leading to the early reionization scenario outlined by the first WMAP investigations.

This picture is illustred in Fig.3.5, in which a scale-free power spectrum for the magnetic field is assumed, i.e. $P_B \propto k^{n_B}$, with $n_B \sim -3$. The formation of the collapsed structures could be favoured also at $z \sim 15$, i.e. in the redshift range suggested by WMAP. Anyway, they showed that only a small fraction of mass range close to the magnetic Jeans scale can collapse, then the typical formed objects are subgalactic and the field has a little impact on the formation of large scale structures at the present epoch.

3.4 Key observations

This section recalls the main observational tests that lead to the idea that the universe suffers a second ionization process and that can provide an estimate for the epoch in which it occurred.

3.4.1 The Gunn-Peterson test

The discovery of high-z quasars at $z \geq 6$ (Fan et al., 2003, 2004; Goto, 2006; Willott et al., 2007, 2009) allows the investigation of the ionization state of the IGM in the early phases of the IGM ionization history.

As shown in Fig. 3.6 (top panel), the typical spectrum of a high-z quasar presents a drop in the emission corresponding to the Lyα ($\lambda = 1216$ Å) redshifted line, when compared to the spectra of the low-z QSO. This feature was first predicted by Gunn & Peterson (1965), but it was observed for the first time by Becker et al. (2001) with the detection of a quasar at $z = 6.28$ in the SDSS data release. This effect can be probably due to the absorption by the neutral hydrogen placed between the source and the observer, since the high cross section of HI for wavelength near to the Lyα can enhance the optical depth of the IGM to this radiation, causing the suppression of the QSO Lyman emission. As achieved by Gunn & Peterson (1965), the optical depth in the Lyman limit is proportional to the neutral fraction of the crossed region, then these observations can be useful in probing the ionization state on the IGM and the end of the reionization epoch. The last estimate of the epoch of reionization (White et al., 2003) indicates as $z \sim 6$ the most probable

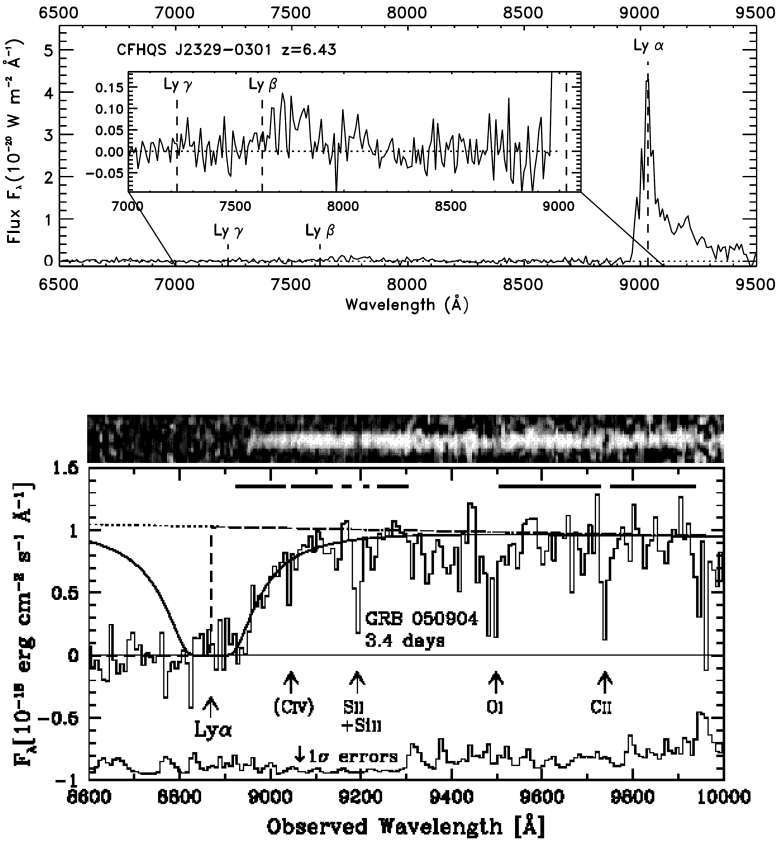

Figure 3.6: The top panel refers to the optical spectra of the farther high-z QSO found in the Canada-France High-z Quasar Survey (CFHQS). The expected locations of Lyα, Lyβ and Lyγ are marked with dashed lines. The inset panel shows the Lyα and the Lyβ forests on an expanded scale (Willott et al., 2007). In the bottom panel, the afterglow spectrum of GRB050904 taken 3.4 days after the burst is shown. The Lyα resonance and identified absorption lines are indicated with the redshift $z_{\rm metal} = 6.295$, except for the intervening CIV system at $z = 4.840$. The solid curve shows the model absorption by a damped Lyα system with $z_{\rm DLA} = 6.295$, while the dotted and the dashed curves show the original unabsorbed spectrum of the afterglow and the model absorption by an IGM with $z_{\rm IGM} = 6.295$, respectively (see Totani et al., 2006, for more details).

reionization redshift, in agreement also with the decreasing HI amount observed by Djorgovski et al. (2001). Anyway, since the theoretical optical depth distribution used to measure the state of HI does not model the observations in the most suitable manner, more accurate models for the physics of the IGM allow to obtain an increase of the HII density also without considering a late reionization at $z = 6$ (Becker et al., 2007). Theoretical estimates of the neutral fraction made on the same high-z quasars, through the typical size of their surrounding ionized bubbles, show that $x_{HI} \gtrsim 0.1$, much larger than that obtained from the observations (Wyithe & Loeb, 2004; Mesinger et al., 2004b; Wyithe et al., 2005a), but the results of Oh & Furlanetto (2005) are discordant. As already mentioned, the main uncertainties in this approaches is the overestimate of the QSO lifetime, that could lead to a physical bubble radius 30% higher than that observed. This incovenient can be avoided considering also the Lyβ and Lyγ forests to estimate the size of the ionized region (Bolton & Haehnelt, 2007b). But other complications can rise from the observation ot the QSO spectra, for example those deriving from the location of the quasars. In fact, the source could be located beyond the reionization epoch but possible residual neutral regions (the Lyman system) can suppress its emission in the Lyα wavelength. To avoid these possible source of bias, a new technique has been recently proposed by Gallerani et al. (2006, 2007); Feng et al. (2008), consisting in the analysis of the statistical distribution of the dark gap widths.

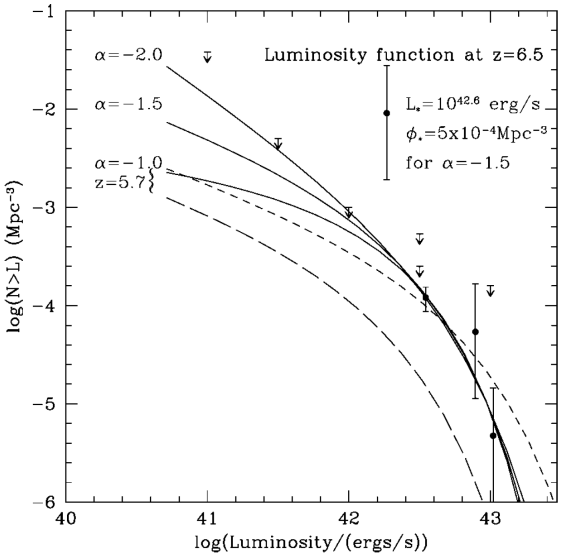

Figure 3.7: The Lyα luminosity function at redshift $z \sim 6.5$. Data points refers to the observed Lyα galaxy density obtained by a set of different samples (the Large-Area Lyman Alpha -LALA- survey, Kurk et al. 2004; Hu et al. 2002; Taniguchi et al. 2005). The three shown curves correspond to the best Schechter function fits to the data for assumed faint-end slopes $\alpha = 1, 1.5$ and 2 (from bottom to top). The $z = 5.7$ best-fit theoretical (short-dashed) curve is still consistent with the data, but a possible flux attenuation by a factor of 3 (long-dashed curve) is ruled out (Malhotra & Rhoads, 2004).

An analogous effect is seen in the spectra of the Gamma Ray Bursts (GRB), shown in Fig. 3.6 (bottom panel). Actually, these high-z sources (recent observations found the highest object GRB 080319B at $z = 6.7$) could represent a very useful tool to probe the ionization state of the IGM, since they are the brightest objects discovered up to now and are usually associated to the first formed stars, then they could allow the investigation of the highest redshifts without the contamination of other effects, like clustering. Moreover, their infrared emission is weakly dependent on their redshift and can be used to constrain the star formation history (Gallerani et al., 2008; McQuinn et al., 2008). In particular the detection of the GRB afterglow can probe the ionization history in a wide range of redshifts through its I, J, H and K emissions and moreover the distortion caused by the free electrons along the line of path could help in painting a picture of the HII topology.

3.4.2 The Lyα emitters

The Lyα radiation is important to determine the location of high-redshift galaxies (Wang et al., 2005; Willis & Courbin, 2005; Kashikawa et al., 2006), for which nowadays it has been estimated a highest limit $z = 6.96$ by Iye et al. (2006); Ota (2007) (even if Stark et al. (2007a,b) has found two possible lensed candidates at $z \approx 10$) showing their crucial role in investigating the properties of the IGM at early epoches. The power of this kind of observations relies in the fact that the HI absorption affects the profile of the Lyα line in emission in their spectra, in particular scattering out of the resonance the blue side of the feature, while the red side would be observed, with a profile strictly related to the state of the surrounding IGM. This scatter produces a compact halo of Lyα light around the source that, despite of its weak emission, can be detected because of its strong polarization. If, on the contrary, the source is surrounded by a large region, the Lyman radiation does not suffer of the HI absorption and redshifts out of the resonance before reaching the boundary of the HII bubble (Cen & Haiman, 2000; Chen et al., 2003). As discussed by Mesinger et al. (2004b), it should be possible to statistically extract important parameters as the neutral fraction of the IGM and the characteristic radius of the ionized regions in the observed spectra of distant galaxies.

The effect of the Lyα emitters has been evaluated also by Malhotra & Rhoads (2004) through the analysis of the luminosity function (LF) of the Lyα galaxies at $z = 5.7$ and 6.5. Subsequent

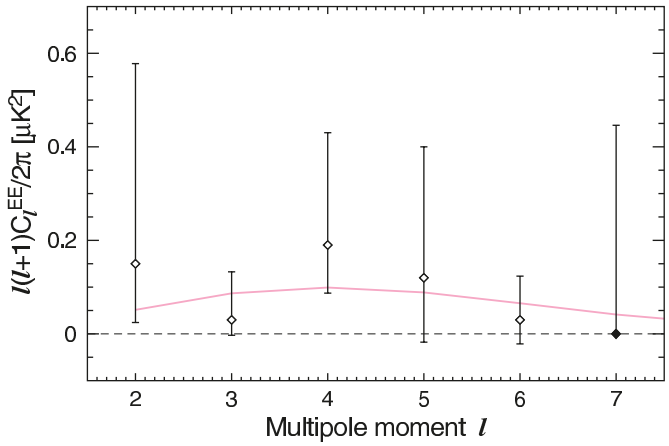

Figure 3.8: The 5-year EE power spectrum at low ℓ. The error bars are the 68% CL of the conditional likelihood of each multipole, with the other multipoles fixed at their fiducial theory values, while the point at $\ell = 7$ is the 95% CL upper limit. The diamonds mark the peak of the conditional likelihood distribution. The pink curve is the fiducial best-fit ΛCDM model (Dunkley et al., 2008).

investigations through numerical simulations have been made by McQuinn et al. (2007) and Iliev et al. (2008c). As shown in Fig. 3.7, where the observed abundance of the galaxies at $z = 6.5$ is shown together with the theoretical LF predicted at $z = 5.7$, the distribution of such galaxies at these two redshifts is similar. This apparent lack of time-evoution in the LF could be explained by the presence of ionized gas between these two epochs that allows the transmission of the Lyα flux, resulting in a complete reionization at $z = 6$.

3.4.3 The CMB footprints

A powerful method to investigate reionization through the CMB-based experiments is the analysis of the (polarization) EE spectrum. In fact, the polarization signal depends more directly on the fluctuation on the last scattering surface than the (temperature) TT spectrum, encoding a wealth of cosmological information. The typical measured polarization signal produced by the last scattering of the photons has a rms of ~ 5 μK and peaks at multipoles $\ell \sim 1000$ (corresponding to the angle subtended by the photon mfp at last scattering, $\propto 1/\ell$).
There are at least two effects on CMB TT and EE anisotropies from early reionisation. The first effect is a damping of the primary anisotropies (Sugiyama et al., 1993). The amplitude of the acoustic peaks can be reduced by reionization and the amount of the damping can be parameterized in terms of the optical depth τ. As an example, an early reionization at $z \sim 15$ can reduce the peaks by approximatively 10% in a flat ΛCDM universe. Anyway, the large-angle E-mode of polarization is more sensitive to the reionization history than the TT and TE spectra.

The second effect is the damping and the production of an additional peak in the EE spectrum (see e.g. Hu, 2000, for a review) due to the following rescattering of the radiation at $z_{\rm reion}$, providing a useful probe of the thermal history of the IGM. In particular, the height of this peak scales as the square of τ of reionization and, assuming suitable models for the IGM ionization process, its position can be a useful constraint for the reionization epoch. Since polarisation traces the last scattering of CMB photons, an early reionization is expected to involve a large angular scale, corresponding to the size of the universe at the moment of reionization. Then, the peak should be found at $\ell < 10$, as shown in Fig. 3.8.
The EE spectrum detected by the last WMAP release (Komatsu et al., 2008; Dunkley et al., 2008) measures a reionization optical depth $\tau = 0.087 \pm 0.017$, that translates into an epoch of reionization $z_{\rm reion} = 11.0 \pm 1.4$, in agreement with an early reionization scenario, if a istantaneous ionization process is assumed. Anyway, the estimates derived by CMB-based experiments suffer of some limitations, as discussed by Hansen et al. (2004). As an examples, the τ value can vary if inferred from power spectra computed separately in the northern and the southern hemispheres, and the WMAP

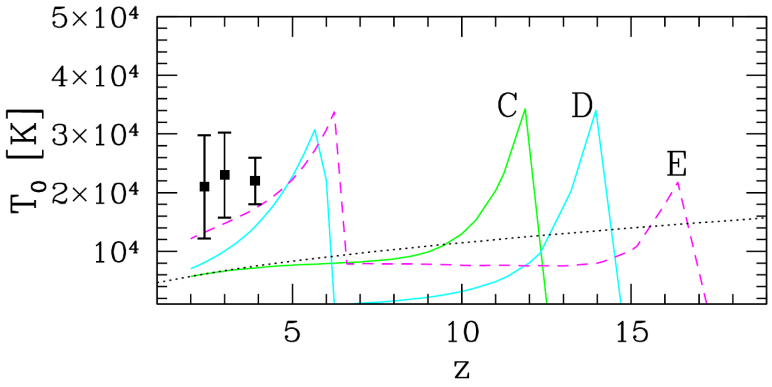

Figure 3.9: The time-evolution of the IGM temperature is here shown. The filled points refer to the observed estimates probed by $z \sim 2,3$ QSO spectra (Zaldarriaga et al., 2001), while the curves correspond to different reionization history driven by quasar-like sources. Model C (solid green line) provides a single HI early reioinization, while model D (solid cyan line) accounts for the double reionization of HI at low z. The (black) dotted line shows the asymptote in case the HeI double reionization is never reached. Finally, model E (magenta dashed line) shows the ionization scenario with an early ionization of HI and (singly) HeI, followed by a late HeII reionization (Hui & Haiman, 2003).

data comes from the southern one in a large part. Moreover, the additional peak at large scales can be explained without reionization introducing primordial magnetic fields. Another useful tool to detect reionization in the CMB spectrum is the investigation of its imprinting on small angular scales due to the secondary anisotropies created by the Thompson scattering. Preliminary studies in this direction have been made by Salvaterra et al. (2005); Zahn et al. (2005); McQuinn et al. (2006); Iliev et al. (2006b), showing the possibility that such anisotropies can probe the different sources of ionizing photons.
Future missions, like Planck, should be able to resolve with higher accuracy the large-angle polarization signal arising from the epoch of reionization, constraining both the height and the position of the peak at $\ell \sim 5$. As shown by Holder et al. (2003), WMAP is insensitive to even large differences in ionization profiles, but Planck could be able to distinguish between various reionisation histories. In fact, as discussed by Bruscoli et al. (2002), the main differences in the EE spectra produced by an istantaneous and an extended reionization scenarios are less than 10%, and as pointed out by Mukherjee & Liddle (2008), the expected sensitivity of Planck should be almost 6%, much higher than WMAP ($\sim 20\%$). However they found that this new satellite would not in general distringuish between an instantaneous and a two-parameter smooth reionization models.

3.4.4 The IGM temperature at $z < 4$

Another observational test that could allow to distinguish between different reionization scenarios, and that has been largely introduced in the previous subsection, is related to the IGM temperature at $z < 4$. In fact, as discussed in Hui & Haiman (2003), the measured IGM temperature at low z from the Lyα spectra of the QSO at $z \sim 2,3$ can retain the thermal memory of the ionization process acting on it at earlier epochs.

Fig. 3.9 shows the temperature history predicted by different reionization models assuming only quasar-like sources. The IGM measured temperature is in agreement with a double ionization scenario, in which a first reionization occurs at $z > 10$, followed by another fully ionization at $6 < z < 10$. This scenario is also supported by the last numerical simulations, as already discussed, in which an early reionization can arise by the action of the first Pop III stars while more standard sources drive the second reionization, that acts in particular on HeII ionization state. The observations show that, in any case, a single ionization phase is ruled out, in favour to a double reionization.

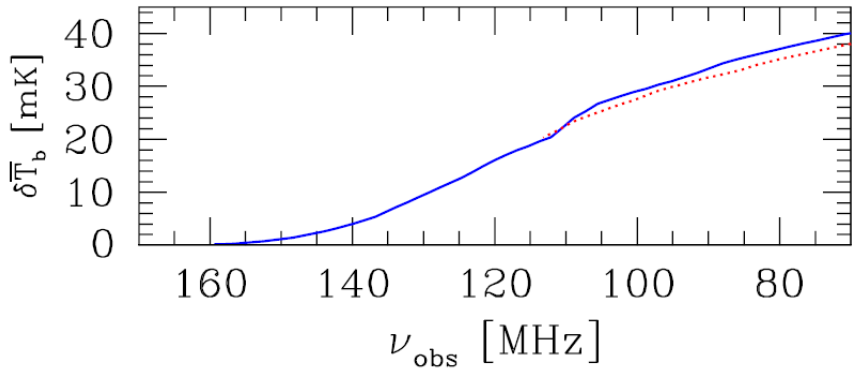

Figure 3.10: The evolution of the mean differential brightness temperature δT_b as a function of the observed frequency, as calculated from the numerical method discussed in Shapiro et al. (2008) assuming a ΛCDM universe (see Shapiro et al., 2008, for more details).

3.5 The Future: 21-cm observations

The future observations at $\lambda = 21$ cm probably represent one of the most powerful instruments to investigate the ionization state of the IGM at high-z. In fact, it has long been known that HI can be detected as an additional contribution to the CMB radiation, at a wavelength corresponding to the redshifted 21 cm, associated to the splin-flip transition from the triplet to the singlet ground states. During the post-recombination era, the small residual free electrons should coupled the temperature of the gas $T_{\rm gas}$ to that of the CMB down to $z \sim 200$ (Peebles, 1993). Later, $T_{\rm gas}$ drops adiabatically $\propto (1+z)^2$ while $T_{\rm CMB}$ remains higher, since proportional to $(1+z)$, then HI should be able to absorb the CMB flux at the redshifted $\lambda = 21$ cm until the beginning of reionization ($z \sim 20$), when the rehating of the gas makes HI visible in emission. As long as $T_{\rm gas}$ remains lower than that of CMB, the absorption of HI produces a decrease of the CMB flux and, subsequently, of its brightness temperature (Loeb & Zaldarriaga, 2004; Loeb, 2006). It results that, since the optical depth of the IGM is proportional to its local HI density, the CMB temperature spectrum shows the imprinting due to the inhomogeneities of the background density field. The 21-cm absorption is replaced by the emission when the first sources of light heat the gas and it occurs well before the complete reionization, because the heating requires a small amount of energy. Actually, for observational purposes, a signal in absorption is preferable because of its strength, but it would imply the presence of radio sources at high z that have not been observed yet. On the other hand, a signal in emission, even if weaker, is always present in the pre-reionization epochs, although it becomes as fainter as the ionization of HI is complete.

The first simulations on large physical scales showing the 21-cm signal expected by the neutral IGM has been built up by Ciardi & Madau (2003), showing that the predicted brightness temperature fluctuations on CMB should be in the range 5-20 mK on scales smaller than 5 arcmins. A similar result has been recently obtained by Shapiro et al. (2008), through high-resolution N-body simulations adopting a radiative transfer code able to resolve the formation of small collapsed objects (10^6 $M_\odot$) and to trace the ionizing radiation from galaxies with $M < 10^8$ $M_\odot$, in a cubic box with $L_{\rm box}$ between 90 and 163 comoving Mpc. They found a brightness temperature fluctuation between 5-15 mK over a 3' scale for the frequency range $\Delta\nu \approx 120 - 140$ Hz, corresponding to mass-averaged ionized fractions $x_m \approx 0.5 - 0.8$, shown in Fig. 3.10.
The future 21-cm observations allow also to constrain the physical properties of a single HII region, its formation and growth around the source (Wyithe et al., 2005b; Zaroubi & Silk, 2005; Rhook & Haehnelt, 2006; Liu et al., 2007; Thomas & Zaroubi, 2008) in particular at high redshifts, when the effect of the overlap is still negligible (Kohler et al., 2005). Moreover, other possibilities are represented by the detection of possible 21-cm radiation outside the HII bubbles, that can be considered as a new way to investigate the BHs accretion, or to probe the galaxy distribution through the effects on 21-cm maps due to the biased Lyα flux rised from the first galaxies (Wyithe & Loeb,

2007). In fact, as obtained by Di Matteo et al. (2004), the contribution to angular scales larger than 1' is dominated by the clustering of the bright sources, that should be efficiently removed to estimate the 21-cm emission of the background gas.
The HI maps predicted by the theoretical models can directly compared to the future observations of the interferometers of the new generation, like the Low Frequency Array (LOFAR). LOFAR will be able to detect the hydrogen emission in the epoch of pre-reionization, indicatively $z > 8.5$, when the global signal at $\nu \sim 150$ MHz should have a brightness temperature $T \sim 10 - 20$ mK and can be easily detected after few hundred hours of integration. The size of the core of the instrument will be optimized so that to receive information from HI regions with a typical size of $10' - 15'$. But at lower frequency, i.e. $\nu = 50$ MHz, the predicted brightness is lower than ~ 1 mK, implying more than a year of integration or an increase of the covering factor of the LOFAR core to observe it (Loeb, 2006). Other powerful instruments that would map HI but in different frequency ranges are the Mileura Wide-Field Array (MWA) and the Primeval Structure Telescope (PAST). As pointed out by Barkana (2008), the 1-year MWA observations could allow to measure the mean ionized fraction to 0.3% accuracy at the end of reionization and to few percent in the mid point, to improve until 10% at the earlier phases. The MWA core will be able to observe the neutral IGM regions with an angular resolution $\sim 3.4'$ at 200 MHz in a total collecting area of 8×10^3 m^2, less than that characteristic of LOFAR (10^4 m^2) that is expected to have a better angular resulution at the same frequency (1.7'). Features similar to MWA are planned for PAST, designed to have an angular resolution $\sim 3'$ at 150 MHz, but with a larger total collecting area of 7^4 m^2. Finally, other probes could be available in a more distant future through the observations provided by SKA, that should be able to probe reionization at $z \lesssim 13$ (Kanekar & Briggs, 2004) on smaller angular scale (~ 8') than those provided by LOFAR, for the same integration time at $\nu = 150$ MHz (Furlanetto & Briggs, 2004c).

Chapter 4

Modeling the cosmic reionization

In this chapter we will introduce the theoretical fundaments of the methods proposed in literature to describe the reionization picture, focusing our attention on the models used in this Thesis work and giving a general overview of the other alternative approaches. Generally, the primary request for a theoretical method is not only testing the agreement of a reionization scenario with the observational data already discussed in the previous section, but it should also be computationally efficient and flexible in making predictions.
Moreover, the complexity of the adopted theoretical approach should be related to the purpose of the investigation, since the analysis of the properties of a single HII region (like its maximum radius) requires a more detailed description of the physical processes acting on IGM rather than the analysis of the global features of reionization process (that are integrated quantities in which the peculiarities of single HII bubbles are lost), like the filling factor or the optical depth of the IGM.
Finally, another crucial point, mainly concerning the analytic description of the statistical properties of gas, is represented by the general validity of the basic hypotheses assumed by the model, that should be consistent with the cosmological framework in which the investigation is performed. Indeed, such tasks are not immediate because of the nature of the physical phenomena involved in the IGM ionization and in the evolution of the structures, that are still unclear at present and could require a high degree of complexity for the theoretical models. For this reason, the methods proposed in literature can be classified according to the nature of their assumptions on the structure formation and the gas physics, and are mainly divided in four families: analytic, semi-analytic, semi-numerical and numerical simulations.

4.1 Overview

As already remarked, building a suitable reionization model leads to several difficulties in giving a theoretical description for all the physical phenomena involved by the processes acting on the IGM and the structure evolution. In fact, the real problem does not concern a possible unknown physics of the gas or the sources, but it is mainly related to the difficulty in solving the relevant equations in full generality, that is a common obstacle in most aspects of large structure formation.
On the other hand, another crucial point is that the reionization modeling requires a tight coupling between the properties of the gas and the evolution of the ionizing structures. Hence, a necessary requirement is that the model assumed for the background structure formation is able to reproduce the available constraints on the luminous sources. Although the statistical and physical properties of the low-z objects have been largely investigated, a relevant uncertainty still persists on the nature of the high-z source population, in particular on the first formed structures. Strong indications from both numerical simulations and analytic investigations lead to single out the first generation of sources in massive and metal-free stars, named Pop III stars (Schaerer, 2002), with a spectrum different with respect to the stars observed at late epochs. In an analogous way, while the intermediate-z QSO spectral, evolutionary and statistical properties have been largely determined, the presence of a possible class of undetected quasars at low-luminosity powered by BHs at high-z is still debated (Ricotti & Ostriker, 2004b). Anyway, even after modeling the structure formation

in a suitable manner, other troubles can arise, for example, from the uncertainties on the photons escape fraction and the feedback, that could prevent the growth of the sources.
These uncertainties can be introduced in the models as adjustable parameters (like the efficiency or the star formation, the escape fraction, etc ...), to calculate the resulting ionization and thermal properties of the IGM under suitable assumptions for their values. Although this approach can lead to a good qualitative description for the global reionization scenario, it is in general unable to provide the details concerning, as an example, the evolution and the morphology of a single HII region, especially in the pre-overlap phase in which the bubbles are almost completely isolated. In fact, the shape of the HII bubble around a source and the overlap of neighboring HII regions can be addressed just in an approximate way, or just through global averages. It is thus clear that not all the complex processes involved in the IGM ionization can be in general associated to a parametric description, then alternative ways of investigations are needed, in order to solve the relevant equations numerically and to follow the ionization history.
However, in order to exploit the full power of the observational data presently available, the model should be able to connect different time and space scales. In fact, at the same time it is necessary to resolve the IGM fluctuations (sub-kpc scales), to follow the formation of the structures (kpc-Mpc), the propagation of the I-front (tens of kpc) and the effect of the ionizing background (Mpc), the quasars and the HII regions (tens of Mpc). Anyway, since the present-day computational limits do not allow to simultaneously consider in an appropriate manner all the above mentioned scales, the current simulations usually try to take into account for, at best, few of these observational constraints, making difficult to understand the limits in which their predictions conflict with the other observational data sets.

4.2 The analytic approaches

There are three main pillars that should be adressed in order to build a reionization model: the structure formation paradigm, the ionization action of the galaxies on the IGM and the re-action of the gas to come back to the neutral state. Then, the purpose of this class of models is to assume suitable assumptions in which these main ingredients can be provided analytically. In most of these models, the structure formation paradigm is provided by the PS74 formalism and its improvements discussed in Chapter 2, while the ionization and recombination of the IGM are introduced through free parameters in an analogous manner to that described in Section 3.1. As an example, the density of the ionizing photons produced by the galaxy can be assumed to be proportional to the fraction of gas within collapsed halos through the ionization efficiency. Furthermore, the analytic nature of these models can allow to consider the effects of the IGM recombination in an homogeneous manner, setting its clumping factor to a constant value, in agreement with the numerical simulations. The resulting reionization scenario is then strictly dependent on the assumed values for ζ and $C_{\rm HII}$ and can be used to just predict in an approximative way the detailed properties of the HII regions. On the other hand, this approach is useful to give a rough picture of the global reionization through integrated quantities as the ionized filling factor or the IGM optical depth, in which the contribution from the single HII bubbles is averaged.
In the following, we will look in detail the model of Furlanetto et al. (2004a) (F04) and its further improvements, that has been assumed in this work, but other methods have been proposed by Haiman & Loeb (1997) and Cojazzi et al. (2000). Actually, a semi-analytic modeling of reionization, that will be described in the next section and allows more realistic description for the IGM recombination, is today the preferred way for building the theoretical models proposed so far in literature, and the pure analytic approach is now obsolete.

4.2.1 The F04 model

In this model, the global reionization scenario is based on the assumption that IGM is a neutral sea in which there are some fully ionized regions. In this picture, every single HII bubble is associated to just a galaxy so that the bubble distribution follows directly that of DM halos, through the following simple assumption:

$$M = \zeta M_{\rm gal} \ , \tag{4.1}$$

where M is the total mass ionized by a collapsed object of mass $M_{\rm gal}$ and ζ is the ionization efficiency introduced in Chapter 3. We should notice that, although similar, the ionization efficiencies involved in Eq. (4.1) and Eq. (3.8) have not the same meaning. In fact, in the previous chapter the masses of the host DM halo and the galaxy are distinguished and related through the amount of baryonic matter in the halo, while in this formalism the ionizing galaxy is identified with the host halo.
Since the mass function (MF) of the collapsed objects is peaked for small mass halos at high z, Eq. (4.1) leads to the formation of small HII regions, conflicting with the picture painted by numerical simulations in which an isolated HII bubble can extend also for several Mpcs beyond its Strömgren radius. The reason is that the HII bubbles of nearby protogalaxies placed in the largest clusters can add, and this renders more complicated the building of a suitable analytic formalism. Moreover, this analytic model assumes the ionization efficiency to be a constant, independent on time and on the mass of the source. Actually, several effects due to the feedback can affect the star formation, possibly resulting in a not constant ζ parameter.
The Eq. (4.1) leads to the ionization condition. In fact, since the region is isolated, it should contain enough collapsed mass to ionize the inner HI atoms, then

$$\zeta f_{\rm coll} \geq 1 \ , \tag{4.2}$$

where $f_{\rm coll}$ is the inner collapsed fraction. In the extended PS74 formalism, assuming that the primordial overdensity field is Gaussian, it is related to the inner overdensity $\delta(M)$ of the region as

$$f_{\rm coll}(M) = {\rm erfc}\left[\frac{\delta_c(z) - \delta(M)}{\sqrt{2[\sigma^2_{\rm min} - \sigma^2(M)]}}\right] \ , \tag{4.3}$$

where $\sigma^2(M)$ is the variance of density fluctuations on the scale M, $\sigma^2_{\rm min} = \sigma^2(M_{\rm min})$, $\delta_c(z)$ is the critical density for collapse, and $M_{\rm min}$ is the minimum mass of an ionizing source. In this work, $M_{\rm min}$ is assumed to be the mass of a DM halo having the virial temperature $T = 10^4$K, at which the HI cooling becomes efficient. Actually, the different feedback phenomena possibly suffered by the source can decrease the star formation in the potential wells, producing a higher $M_{\rm min}$. The above equation leads to rewrite the ionization condition in the following form:

$$\delta(M) \geq \delta_x(M,z) \equiv \delta_c(z) - \sqrt{2}K(\zeta)[\sigma^2_{min} - \sigma^2(M)]^{1/2} \ , \tag{4.4}$$

where $K(\zeta) = {\rm erf}^{-1}(1-\zeta^{-1})$. In the excursion-set formalism, δ_x represents a sort of barrier for a space point having $\delta(M)$ on the smoothing scale M to belong to a ionized region. Then the statistical properties of the HII bubbles can be investigated through the excursion-set formalism analogously to the collapsed objects, but with the main difference that the ionization barrier depends on the mass scale. As stressed by Furlanetto et al. (2004a), in the redshift range of interest and as long as $M \gtrsim M_{\rm HII,min} = \zeta M_{\rm min}$, the δ_x threshold can be espressed as a linear function of the variance $B(M,z) = B_0 + B_1\sigma^2(M)$ in which

$$B_0 \equiv \delta_c(z) - \sqrt{2}K(\zeta)\sigma_{\rm min} \tag{4.5}$$

$$B_1 \equiv \frac{\partial \delta_x}{\partial \sigma^2}\Big|_{\sigma^2=0} = \frac{K(\zeta)}{\sqrt{2\sigma^2_{\rm min}}} \ . \tag{4.6}$$

Since this approximation renders the ionization barrier linearly dependent on variance, the excursion-set formalism is still valid (Sheth, 1998) and allows to find an analytic espression for the distribution of the HII regions:

$$n_b(M,z) = \sqrt{\frac{2}{\pi}}\frac{\bar{\rho}}{M^2}\left|\frac{{\rm d}\ln\sigma}{{\rm d}\ln M}\right|\frac{B_0}{\sigma(M)}\exp\left[-\frac{B^2(M,z)}{2\sigma^2(M)}\right] \ , \tag{4.7}$$

that represents the comoving number density of the HII bubbles in the mass range $[M - {\rm d}M, M + {\rm d}M]$. Through Eq. (4.7), the global reionization properties can be inferred by the time-evolution of the volume filled by the HII regions Q_i:

$$Q_i(z) = \int_{M_{\rm HII,min}}^{\infty} n_b(M,z)V(M)\,{\rm d}M \ , \tag{4.8}$$

that, as already discussed in the previous chapter, is just an approximate form of the real ionized filling factor of the universe. The 'true' value of the ionized fraction is given by $\bar{x}_i(z) = \zeta f_{\rm coll,g}(z)$, where $f_{\rm coll,g}(z)$ is the global collapsed fraction achievable from the PS74 approach, and as shown by the authors can become higher than $Q_i(z)$ at early cosmological epochs. This difference arises from Eq. (4.3), that breaks down on sufficiently small scales, and from the linear approximation to the ionization barrier, that does not properly fit δ_x on the smaller mass scales. Anyway, this difference is relevant only when $Q_i \gtrsim 0.1$, i.e. when the ionized bubbles have a small effect.
The excursion-set formalism allows the description of the HII bubble evolution through their progenitor distribution, that could be achieved following the Lacey & Cole (1993) approach but assuming the linear threshold $B(M, z)$. The conditional probability distribution of the HII regions has been discussed by the authors in a later paper (Furlanetto & Oh, 2005, hereafter F05) in the same analytic way of F04. Assuming that a fixed point corresponds to a HII region of size M_b at z_b, i.e. $\delta(M) = B(M_b, z_b)$, the conditional mass function representing the progenitor distribution at $z > z_b$ is

$$n_b(M, z|M_b, z_b) = \sqrt{\frac{2}{\pi}} \frac{\bar{\rho}}{M^2} \left| \frac{{\rm d}\ln\sigma}{{\rm d}\ln M} \right| \frac{\sigma^2[B(M_b, z) - B(M_b, z_b)]}{(\sigma^2 - \sigma_b^2)^{3/2}} \tag{4.9}$$

$$\exp\left[- \frac{[B(M, z) - B(M_b, z_b)]^2}{2(\sigma^2 - \sigma_b^2)} \right] . \tag{4.10}$$

As a consequence, the integration of the above equation allows the investigation of the ionized fraction inside the bubbles, that is simply proportional to their global collapsed fraction. In the linear approximation

$$x_i(z|M_b, z_b) = \zeta {\rm erfc}\left[\frac{\delta_c(z) - B(M_b, z_b)}{\sqrt{2(\sigma_{\rm min}^2 - \sigma_b^2)}} \right] , \tag{4.11}$$

but in reality, as already remarked, the reionization picture derived from Eq. (4.11) is strongly affected by the possible feedback of the source, that cannot be introduced in an appropriate manner in this model due to its analytic nature.
Through the same procedure in Lacey & Cole (1993), the progenitor size distribution leads to an analytic espression for the merging rate of the HII bubbles, that results

$$\frac{{\rm d}^2 p(M_1, M_T, t)}{{\rm d}M_2 {\rm d}t} = \sqrt{\frac{2}{\pi}} \frac{1}{t} \left| \frac{{\rm d}\ln B(M_T, t)}{{\rm d}\ln t} \right| \left| \frac{{\rm d}\ln\sigma_T}{{\rm d}\ln M_T} \right| \frac{1}{M_T} \frac{B(M_T, t)}{\sigma_T (1 - \sigma_T^2/\sigma_1^2)^{3/2}} \times \tag{4.12}$$

$$\exp\left[- \frac{B_0^2(t)}{2} \left(\frac{1}{\sigma_T^2} - \frac{1}{\sigma_1^2} \right) \right] \tag{4.13}$$

and represents the probability that a HII region of mass M_1 merges with another region of mass $M_2 = M_T - M_1$ per unit time. It is useful to define a merger kernel as follows

$$Q(M_1, M_2, t) \equiv \frac{1}{n_b(M_2, t)} \frac{{\rm d}^2 p(M_1, M_T, t)}{{\rm d}M_2 {\rm d}t} , \tag{4.14}$$

so that the total rate at which bubbles with M_1 merge with those of mass M_2 (per unit volume) is $n_b(M_1) n_b(M_2) Q(M_1, M_2)$. Actually, the above quantity suffers of the same limitations than the DM halo merger rate. In fact, as discussed by Benson et al. (2005), the merger rate does not properly conserve the mass. Moreover, another defect is the asymmetry of Q with respect to its arguments, that becomes important for large mass ratio mergers. Anyway, as pointed by F05, its effect should be reduced for the HII bubble merger rate thanks to their small mass cut-off and, on the oher hand, can be corrected by using the symmetrized version $2Q_{sym}(M_1, M_2) = Q(M_1, M_2) + Q(M_2, M_1)$. The merger rate can also be espressed in terms of the fractional volume accretion rate by which bubbles with mass M_1 grow through merger with bubbles of mass M_2, i.e.

$$V(M_1) \frac{{\rm d}V}{{\rm d}z} \equiv \frac{V(M_2)}{V(M_1)} M_2 n_b(M_2, z) Q_{sym}(M_1, M_2, t) \left| \frac{{\rm d}t}{{\rm d}z} \right| . \tag{4.15}$$

As a final remark, we should stress that the theoretical formalism described above does not take into account the IGM recombination, that has been introduced by the authors in the more recent version of the model proposed by F05. Then, in the following investigation of reionization in alternative cosmological scenarios we will assume the F05 method, that will be described in the next section.

4.3 The semi-analytic approaches

The previous family of theoretical approaches to reionization suffers of strong limitations due to the approximate way in which the gas physics is introduced. In fact, recombination is determined by the IGM local density, that is usually assumed to be the same at every point of the universe by setting a constant clumping factor. Actually, the IGM topology is affected by the action of the gravity, that depends on the local DM field and can introduce non-negligible deviations from the pure homogeneous state. The gas distribution hence results inhomogeneous, with lower-dense and higher-dense regions determined by the degree of the inner gas clumpiness and strictly related to the DM overdensity topology. Then, in a theoretical paradigm in which the recombination is linearly related to the local gas density, the effects of the IGM inhomogeneities are expected to give a more realistic description of the ionization history of the universe.
The aim of the semi-analytic approaches is then to improve the rough assumption for the gas recombination made by the analityc models introducing an analytic formalism for the IGM physics and, in particular, for its density distribution, that should be in agreement with the numerical simulations. The importance of these methods lies in the fact that the lower-dense regions can be ionized first than the higher dense clouds, that can remain neutral for a longer time. This affects not only the detailed properties of the HII bubbles but also the time-evolution of reionization and the distribution of the Lyman Limit Systems (LLS), the high density regions responsible for the absorption in the QSO spectra.
Although providing a suitable description for the gas physics, a strong limitation of the semi-analytic models consists of the lack of a good formalism describing the clustering of the sources. In fact, since the host DM halos are placed in the higher dense regions, the morphology of the HII bubbles can be determined by the galaxy clustering pattern. Neglecting the correlation among the sources can lead to an underestimate of the typical size of the bubbles, and as a consequence to a different reionization topology. For that concerning this issue, the semi-analytic approaches suffers of the same limitations of the analytic methods, since they are mostly based on the extended PS74 formalism that can take into account for the clustering just in an approximative way.
At present, many semi-analityc models have been proposed in literature (see e.g. Chiu & Ostriker, 2000; Miralda-Escudé et al., 2000; Wyithe & Loeb, 2003; Cen, 2003; Furlanetto & Oh, 2005; Avelino & Liddle, 2006; Benson et al., 2006; Choudhury & Ferrara, 2006; Cohn & Chang, 2007), but in the following we will illustrate the fundamental basis of the F05 and the Avelino & Liddle (2006) (hereafter AL06) models, that will be used in our work.

4.3.1 The F05 model

The aim of this model is to improve the previous F04 analytic approach introducing a suitable description for the IGM recombination, whose effects on the bubble topology have been up to now neglected. Here, we will review only the main features of this approach, referring to Furlanetto & Oh (2005) for more details.
The recombination properties of IGM can be implemented following the approach of Miralda-Escudé et al. (2000) (MHR00) that, using hydrodynamic numerical simulations at intermediate redshifts ($2 < z < 4$), found a simple analytic fit to the IGM density distribution, resulting in good agreement with the observations of the Lyα forest in the QSO's spectra (Rauch et al., 1997). Assuming Gaussian initial conditions and a ΛCDM cosmological framework, the volume-weighted density distribution for the IGM reads as

$$P_V(\Delta)\mathrm{d}\Delta = A_0\Delta^{-\beta}\exp\left[-\frac{(\Delta^{-2/3}-C_0)^2}{2(2\delta_0/3)^2}\right]\mathrm{d}\Delta\ , \tag{4.16}$$

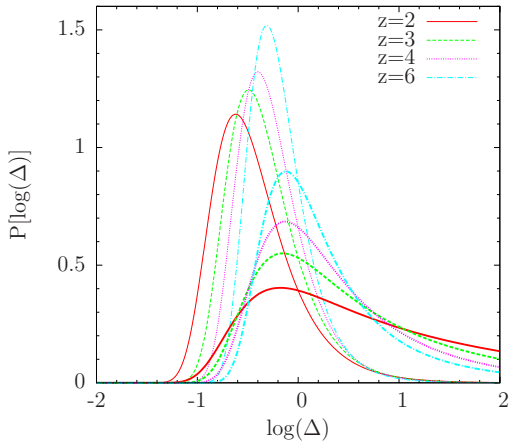

Figure 4.1: The mass-weighted (thick line) and volume-weighted (thin line) differential density distributions of the IGM at different redshifts, computed assuming analytic formula of MHR00 assuming the fit parameters of Table 1 in Miralda-Escudé et al. (2000).

where δ_0 essentially represents the variance of density fluctuations smoothed on the Jeans scale for an ionized medium, and can be extrapolated as $\delta_0 = 7.61/(1+z)$, while A_0, C_0 and β are fitting parameters, generally dependent on z. In particular, the power law exponent β determines the behaviour at large redshifts and has been set by F05 to the value corresponding to an isothermal sphere, $\beta = 2.5$, in reasonable agreement with the simulations. The other parameters A_0 and C_0 are then fixed by requiring that the total volume and mass are normalized to unity.
The resulting gas density distribution is illustrated in Fig. 4.1, for a ΛCDM cosmology consistent to MHR00 and $z = 2, 3, 4, 6$, assuming their best fit parameters. The two functions shown at each redshift are $\Delta P_V(\Delta)$ and $\Delta^2 P_V(\Delta)$, which are respectively the volume-weighted and the mass-weighted probability density of Δ per unit $\log \Delta$. Indeed, the behaviour of the obtained IGM distribution is peaked up at higher values for Δ as the redshift increases and, as discussed also by Rauch et al. (1997), it should be mostly related to the amplitude of the initial density fluctuations smoothed on the Jeans scale of the photoionized gas. As remarked by the authors, a possible significant fraction of all the baryons is contained in minihalos with virial temperatures $T \sim 10^4$ K, which collapsed to high densities before reionization, when the Jeans mass was very small. These halos has not been resolved in this simulation and could survive for a long time after the reionization epoch if other physical processes as star formation or merging do not destroy them. In this case, the density distribution would be wider at high redshift, with a larger fraction of the baryons at very high densities. F05 provided a rough treatment for the effects of minihalos on the IGM ionization, anyway since a suitable formalism describing the action on the I-front due to these small DM halos is still not avalaible from the simulations, this possibility will not be considered in this Thesis work.
In order to describe the ionization state of the gas, MHR00 introduce a density threshold Δ_i such that all the gas with $\Delta < \Delta_i$ is ionized, while the IGM remains neutral when $\Delta > \Delta_i$. As remarked by these authors, this approximation cannot indeed be a real description of the IGM ionization state, that should depend on the local ionizing background and on the local self-shielding degree, but as pointed by F05 it could be reasonable if these LLSs can be considered as isolated clumps in which the density increases inwards. The radiation can just ionize, hence, the edge of such regions, in which $\Delta \sim \Delta_i$. Then, the recombination rate is

$$A(\Delta_i) = A_u \int_0^{\Delta_i} \mathrm{d}\Delta \, P_V(\Delta)\Delta^2 \equiv A_u C(\Delta_i) \ , \tag{4.17}$$

where C is the effective clumping factor and A_u is the recombination rate per hydrogen atom in gas at the mean density, $A_u = \alpha_A(T)\bar{n}_e$. Following MHR00, α_A is set in agreement with the case-A recombination (see also Miralda-Escudé, 2003), in which the LLS regions are painted as sinks of ionizing photons, then $\alpha_A = 4 \times 10^{-13}$ at $T = 10^4$ K and $\bar{n}_e = \bar{n}_b(z)(1 - 3/4Y)$ is the mean density

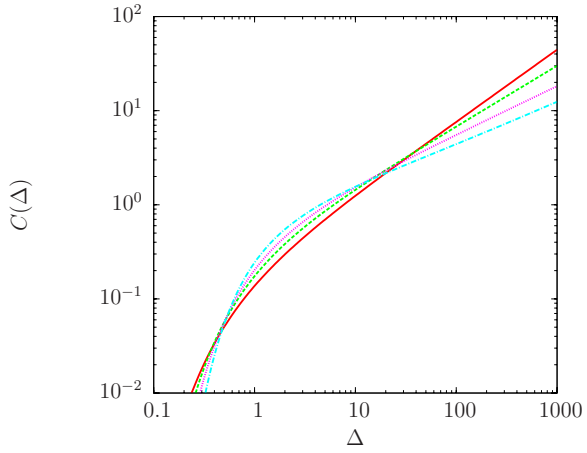

Figure 4.2: The evolution of the effective clumping factor C with the density threshold Δ. The different lines correspond to the redshifts $z = 2, 3, 4, 6$, analogously to Fig. 4.1.

of free electrons. The resulting recombination rate per HI atom is

$$A_u(z) \sim 4.3 \times 10^{-18} h^2 \Omega_{0,b} \left(1 - \frac{3}{4}Y\right)(1+z)^3 \quad [1/\mathrm{s}] \ . \tag{4.18}$$

Fig. 4.2 shows the effective clumping factor C calculated for different values of the density threshold here named Δ. As discussed also by MHR00, as long as $P_V(\Delta)$ is less steep than Δ^{-3} at large Δ, the IGM clumpiness increases monotonically with the threshold. This property is in agreement with the 'inside-out' nature of reionization. In fact the high-density regions must have a larger IGM overdensity and, as a consequence, a higher clumping factor than the low-density regions, then they will be ionized only at the later stages, under the assumption of a balance between the global recombination and the emissivity.
In this threshold approximation, where all the gas with $\Delta < \Delta_i$ is ionized, the mfp of the ionizing photons is the distance between subsequent contours at Δ_i, that is the mean length of underdense regions along random lines of sight. Actually the estimate of the mfp is affected by several factors as, for example, a milder transition between the ionized and neutral states near the edge of the HII region and, moreover, possible high-density clumps inside the region that could inhibit the grow of the HII bubble. Anyway, since most of recombination occurs at $\Delta = \Delta_i$, the mfp can be reasonably approximated to the typical size of the HII regions, which is

$$\lambda_i = \lambda_0 [1 - F_V(\Delta_i)]^{-2/3} \ , \tag{4.19}$$

where $F_V(\Delta_i)$ is the volume fraction with $\Delta < \Delta_i$ and λ_0 is a redshift-dependent normalization constant. Although in the limit of high densities Eq. (4.19) is valid if the number density and the shape of absorbers is independent of Δ_i, that is indeed generally not true for the cosmic web, MHR00 found that this relation is still aproximatively obeyed in the results of the numerical simulations of photoionized gas. The physical scale λ_0 is set through numerical simulations on the Lyα forest at intermediate redshifts, and is generally dependent on z and on the cosmological model. Anyway, as discussed by MHR00, the quantity $\lambda_0 H(z)$ stays roughly constant in the simulation and results equal to 60 km/s, that has been extrapolated also at higher redshifts by F05.

The resulting evolution of the mfp for different values of the density threshold is steeper at higher redshifts, as shown in Fig. 4.3, involving a generally larger λ_i as z increases. A general warning concerning the redshift range of validity for this model should be mentioned, since its application to higher redshifts indeed involves several simplifications and limitations as an overestimated mfp of the ionizing photons, that could strongly affect the reionization scenario predicted by this model and that have been deeply discussed by F05.
Through this semi-analytic model for the gas physics, the F04 approach has been improved introducing the treatment for the IGM recombination. In fact, in order for a bubble to grow, the

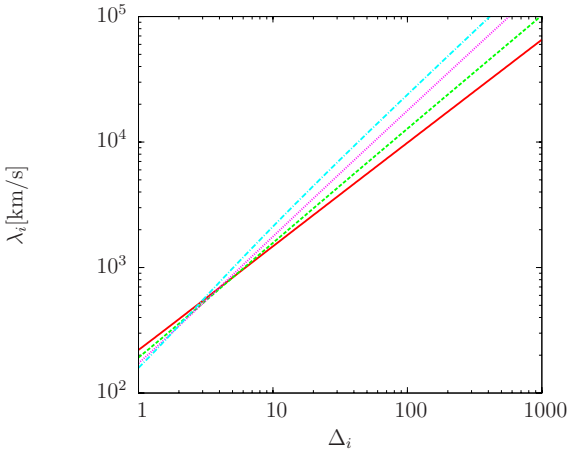

Figure 4.3: The mean free path of ionizing photons as a function of the overdensity up to which the gas is ionized, computed according to Eq. (4.19). The curves refers to the same redshifts shown in Fig. 4.1

ionizing photons should be able to reach its edge and the ionization rate should be higher than the recombination rate. But, since the recombination rate increases as the bubble expands, at the given distance from the galaxy $R = \lambda_i(\Delta_i)$ the ionization equilibrium condition is reached:

$$\zeta \frac{\mathrm{d}f_{coll}(R,\delta)}{\mathrm{d}t} = A_u C'[\Delta_i(R),\delta] \ , \tag{4.20}$$

where $C' = C(\Delta_i(R))(1+\delta)$ and δ is the inner smoothed overdensity of the region. This last term takes into account not only the 'inside-out' nature of the reionization process, since the HII regions correspond to the overdense regions of the universe, but also the depencence of the gas recombination on the local density. Moreover, Eq. (4.20) describes the HII bubbles as not fully ionized regions, due to the inner high-density clumps, and as a consequence the ionized volume fraction as calculated by F04 is just a rough approximation of the effective fraction of ionized HII atoms in the universe.
Eq. (4.20) can be solved numerically to find the overdensity equilibrium δ_r as a function of the typical size of the HII bubbles R, in the excursion set formalism this introduces a recombination barrier so that a trajectory should cross $\delta = \max(\delta_x, \delta_r)$ in order to be a part of an ionized region. This added barrier fixes an upper limit for the possible mass of the HII bubbles, corresponding to the value R_{max} at which $\delta_x = \delta_r$, hence recombination prevents their growth on scales larger than R_{max} and the resulting bubble distribution is expected to pile up around the maximum allowed radius. An analytic expression for the mass function of the HII region on scales $R \leq R_{max}$ can be found under the assumption that, in the excursion-set formalism, recombination is a vertical barrier at $R = R_{max}$ beginning at $B(R_{max})$, beyond which there is no further barriers at all. Then the probability distribution at R_{max} is Gaussian and reads

$$p(\delta|R_{max}) = \frac{1}{\sqrt{2\pi}\sigma_{max}} \exp\left(-\frac{\delta^2}{2\sigma^2_{max}}\right) \ , \tag{4.21}$$

where $\sigma_{max} = \sigma(R_{max})$, and as a consequence the resulting comoving density of such bubbles is

$$N_{rec}(M_{max}) = \frac{\bar{\rho}}{2M_{max}} \mathrm{erfc}\left[\frac{B(R_{max})}{\sqrt{2}\sigma_{max}}\right] \ . \tag{4.22}$$

On the other hand, trajectories with $\delta(R_{max}) < B(R_{max})$ cross the ionization barrier on smaller scales, and the resulting mass function is

$$n_{rec}(M,z) = \int_{-\infty}^{B(R_{max})} \mathrm{d}\delta \, p(\delta|R_{max}) n_b(M,z|\delta,M_{max},z) \ , \tag{4.23}$$

where $n_b(M, z|\delta, M_{max}, z)$ is the conditional mass function for a trajectory starting at (σ^2_{max}, δ) that can be achieved through Eq. (4.19) by replacing $B(M_b, z_b)$ with δ. The above equation represents the weighted average of the conditional mass function evaluated over all densities smoothed on R_{max} and can be calculated analitically. After reaching the equilibrium state, the bubble can grow only by overlap with other neighbouring bubbles. Since the ionization regime on scales higher than R_{max} is regulated only by the ionization barrier, the size distribution of such regions is essentially provided by Eq. (4.7) and their total volume fraction can be calculated following Eq. (4.8) in which, in this case, the minimum mass of the HII regions is M_{max}.
This semi-analytic model allows also to investigate the absorption of the radiation by the intergalactic gas. A rough picture of the effects of the inhomogeneous distribution of the IGM can be provided by the global recombination rate of the HII regions, that in this formalism is an averaged mean of the recombination rate of each HII bubbles:

$$\bar{A}_{bub} = \int \mathrm{d}M\, A(M) V(M) n_b(M)[1 + \delta_x(z)] \;, \tag{4.24}$$

where $A(M)$ is the clumping factor of the ionized region with mass M and the last factor represents the inner mean physical overdensity. The recombination limit can then strongly affect the way in which the bubbles overlap and their general absorption properties, with consequences on the transmission of the Lyα flux in particular at the late phases of reionization, when the typical size of the HII regions is larger. Extending the Furlanetto et al. (2004b) approach through this more realistic treatment for the gas physics, the probability that a fixed point of the IGM has an optical depth τ for the $i-$th transition smaller than τ_i is

$$P(< \tau_i, z) = \int \mathrm{d}M\, n(M, z) \frac{M}{\bar{\rho}} \int_0^{\Delta_{max}} \mathrm{d}\Delta\, P_V(\Delta) \;, \tag{4.25}$$

for which Δ_{max} is the maximum density for which $\tau < \tau_i$. This quantity can be calculated under the assumption of the ionization equilibrium for the HII region, that reads

$$x_{\rm HI} = \frac{\chi_e \bar{n}_{\rm H} \alpha_A(T)}{\Gamma} \Delta \;, \tag{4.26}$$

where χ_e is the correction for HeII and Γ is the ionizing rate per hydrogen atom. It mainly depends on the total photons' emissivity ϵ_T and on the mean free path λ_i as

$$\Gamma \propto \lambda_i \epsilon_T \left(\frac{\eta}{3 + \eta} \right) . \tag{4.27}$$

At the end of reionization $\epsilon_T \propto \zeta \mathrm{d}f_{\rm coll,g}/\mathrm{d}t$, $\eta = 3/2$ if a starburst spectrum is assumed and λ_i is set to the minimum value between the bubble radius and $R_{\rm max}$. Finally, $P_V(\Delta)$ is thought to be independent of the bubble morphology, that can be a good approximation at the end of reionization although high-resolution simulations are required to test it. On the other hand, the IGM recombination can be described by assuming $\alpha_A \propto T^{-0.7}$ and the IGM $T - \delta$ relation as $T = T_0 \Delta^\gamma$, with $T_0 = 10^4$ K and γ consistent with a polytropic model for the IGM, that is in good agreement with the numerical simulations. Hence, the relation between the local overdensity and the IGM optical depth is:

$$\Delta(\tau_i) = \left\{ 170 \frac{\eta}{3 + \eta} \frac{\alpha_A(10^4 \mathrm{K})}{\alpha_A(T_0)} h(z) \left(\frac{\lambda_i}{\mathrm{Mpc}} \right) \zeta \left| \frac{\mathrm{d}f_{\rm coll}}{\mathrm{d}z} \right| \left(\frac{\tau_i}{\tau_{GP,i}} \right) \right\}^{1/(2-0.7\gamma)} , \tag{4.28}$$

where $\tau_{GP,i}$ is the Gunn & Peterson optical depth for the i-th transition. Finally, the probability for the inhomogeneous IGM to have a given optical depth τ is obtained by substituting $\Delta_{\rm max}$ in equation (4.25).

4.3.2 The AL06 approach

We now briefly review the main assumptions underlying the analytic model adopted to describe the process of cosmic reionization. This model is based on the approach proposed by Avelino & Liddle

(2006) [see also Haiman & Holder (2003); Chen et al. (2003) for further details]; our implementation, however, differs in some aspects which will be discussed later on. We finally should stress on the simplyfing nature of this model: in fact, unlike the F04 approach and its further improvements, the AL06 method does not allow a deep investigation of the detailed features of the single HII regions. This is not only due to the difficult extension of the ionization treatment proposed by F04 to cases of a non-Gaussian overdensity field, but also to the lack of a suitable theoretical model describing the IGM recombination in a non-Gaussian framework, since the MHR00 simulations are based on Gaussian initial conditions. For those regions, this approach can just roughly predict the global features of reionization.
In this model, the statistical properties of the ionized regions are related to the hierarchical growth of the ionizing sources through simple assumptions on how the galaxies ionize the IGM and on how the IGM recombines. A one-to-one correspondence between the distribution of galaxies and HII regions is established, such that a single galaxy of mass $M_{\rm gal}$ can ionize a region of mass $M_{\rm HII} = \zeta M_{\rm gal}$. Here ζ represents the ionization efficiency of the galaxy, and it is strictly dependent on the nature of the ionizing sources. Following the Haiman & Bryan (2006) approach, the original model proposed three different class of possible reionization sources, according to their virial temperature T:

- $4{\times}10^2$ K $\lesssim$ T $\lesssim 10^4$ K (Type II);
- 10^4 K $\lesssim$ T $\lesssim 9 \times 10^4$ K (Type Ia);
- $T \gtrsim 9 \times 10^4$ K (Type Ib);

however, since at high z the cooling of the gas becomes efficient in halos having a virial temperature $T \geq 10^4$ K, unlike in AL06, in our analysis we consider only type Ia (10^4 K $\leq T \leq 9 \times 10^4$ K) and type Ib ($T > 9 \times 10^4$ K) sources, neglecting the contribution of the type II sources. We recall that the distinction between the halo types is related to the way in which they impact the IGM: type Ia sources can grow only in neutral regions, while type Ib haloes can appear also in ionized regions, independently of the H_2 abundance. On the other hand, type II halos form only in the neutral regions, provided there is a sufficient abundance of H_2 molecules. Consequently they differently affect the ionization phases of IGM.
The total collapsed fraction $F_{\rm coll}(z)$ at different redshifts can be computed through the mass function of the collapsed halos as follows

$$F_{\rm coll}(z) = \frac{1}{\bar{\rho}_0} \int_{M_{\rm min}(z)}^{\infty} {\rm d}M \, n(M,z) \ ,$$

where $M_{\rm min}(z)$ is the minimum mass corresponding to the virial temperature T, which can be computed by inverting the relation proposed by Barkana & Loeb (2001), namely:

$$T = 1.98 \times 10^4 \left(\frac{1+z}{10}\right) \left(\frac{M}{10^8 M_\odot h^{-1}}\right)^{2/3} \left(\frac{\Omega_{\rm m0}}{\Omega_{\rm m}^z} \frac{\Delta_c}{18\pi^2}\right)^{1/3} {\rm K} \ . \tag{4.29}$$

In the previous equation, $\Delta_{\rm c}$ represents the virial overdensity at redshift z and $\Omega_{\rm m}^z$ is the matter density parameter at redshift z. Consequently, the collapsed fractions in Ia and Ib haloes are given by

$$\begin{aligned} F_{{\rm coll},Ib}(z) &= \frac{1}{\bar{\rho}_0} \int_{M_{{\rm min},Ib}(z)}^{\infty} {\rm d}M \, n(M,z) \\ F_{{\rm coll},Ia}(z) &= \frac{1}{\bar{\rho}_0} \int_{M_{{\rm min},Ia}(z)}^{\infty} {\rm d}M \, n(M,z) - F_{{\rm coll},Ib}(z) \ , \end{aligned} \tag{4.30}$$

where $M_{{\rm min},Ib}$ and $M_{{\rm min},Ia}$ are the minimum masses for Ib and Ia sources, obtained using in eq.(4.29) $T = 9 \times 10^4$ and 10^4 K, respectively.
The action of the ionizing sources is smoothed down by the recombination of the IGM, here

considered as a homogeneous gas. In this case, as already mentioned, the recombination rate is linearly dependent on the IGM clumping factor $C_{\rm HII} =< n^2_{\rm HII} > / < n_{\rm HII} >^2$, for which Haiman & Bryan (2006) proposed the following redshift evolution:

$$C_{\rm HII}(z) = 1 + 9\left(\frac{1+z}{7}\right)^{-\beta} , \tag{4.31}$$

being β a free parameter. As shown by AL06, the predicted reionization history of the universe has significant uncertainties introduced by the poor knowledge of the z-dependence of the clumping factor, which cannot be robustly constrained even considering the 3-year WMAP results for the reionization optical depth. As discussed by AL06, a good consistency between predicted and observed optical depths can be found setting $0 < \beta < 2$. When $\beta = 0$, the z-dependence of $C_{\rm HII}$ is neglected and $C_{\rm HII} = 10$ in agreement with the MHR00 simulations.
Under the assumption of a constant clumping factor, the probability that a photon emitted at a given cosmological epoch $z_{\rm i}(t_{\rm i})$ is still ionizing at $z < z_{\rm i}$ can be written as

$$P(t_{\rm i}, t) = \exp\left(\frac{t_{\rm r}}{t} - \frac{t_{\rm r}}{t_{\rm i}}\right) , \tag{4.32}$$

with $t_{\rm r} = \alpha_{\rm B} C_{\rm HII} n_{\rm HI}(t_{\rm i}) t_{\rm i}^2$, being $\alpha_{\rm B}$ the recombination coefficient of HI ($= 2.6 \times 10^{-13}$ cm^3/s at $T = 10^4$ K) and $n_{\rm HI}(z) = 1.88\Omega_{0,b}h^2/0.022(1+z)^3/{\rm cm}^3$ the hydrogen density at redshift z. Then, the filling factor $F_{\rm HII}(z)$ at a given cosmological epoch is

$$F_{\rm HII}(z) = \int_{\infty}^{z} {\rm d}z' \, \zeta \left\{ \frac{{\rm d}F_{{\rm coll},Ib}}{{\rm d}z'}(z') + [1 - F_{\rm HII}(z')] \times \times \frac{{\rm d}F_{{\rm coll},Ia}}{{\rm d}z'}(z') \right\} P(z', z) \ ,$$

where the ionizing efficiency is assumed to be the same for the different types of haloes. We notice that the different nature of type Ib and Ia sources appears in the right-hand side of eq.(4.33), where the $(1 - F_{\rm HII})$ factor explicitly considers that type Ia haloes form only in neutral regions.
Finally, the HII filling factor allows us to estimate the reionization optical depth as follows:

$$\begin{aligned} \tau(z) &= c\sigma_{\rm T} \int_{\rm t}^{t_0} {\rm d}t' \, n_{\rm e}(t') \\ &= 1.08 \, c \, \sigma_{\rm T} \int_{\rm z}^{0} \frac{{\rm d}t}{{\rm d}z'} {\rm d}z' \left(1 - \frac{3}{4}Y\right) \frac{\rho_{\rm b}(z')}{m_{\rm p}} F_{\rm HII}(z') \ ; \end{aligned} \tag{4.33}$$

here $\sigma_{\rm T}$ represents the cross-section of the Thompson scattering, $n_{\rm e}$ is the free-electron density, c is the speed of light, Y is the He mass fraction, $\rho_{\rm b}(z)$ is the baryon density at redshift z and the factor 1.08 approximately accounts for the contribution of the HeI reionization, assuming that the HII and HeII fractions are equal and neglecting the effects of the HeII to HeIII phase transition.

4.4 The semi-numerical (or perturbative) approaches

The purpose of this class of models is to investigate reionization in an analogous manner to simulations, but introducing some simplyfications to avoid too high computational cost of the numerical methods.
The main challenging requirement that should be addressed in order to build suitable reionization simulations is the large computational box, necessary to probe the largest coherently ionized regions in the final stages of reionization. In fact, the ionized regions are expected to have typical sizes of tens of Mpc (Furlanetto et al., 2004b; Furlanetto & Oh, 2005), requiring a simulation box of hundreds of Mpc.
At the same time, the resolution of the box should be high to resolve most of the ionizing sources that, since the IGM ionization begins at early epochs, have a characteristic mass $< 10^8$ M$_\odot$. This is generally addressed through N-body simulation codes that are, however, very time-consuming.
On the other hand, also a more precise treatment for the propagation of the I-front, generally

introduced by radiative transfer codes, is necessary to suitably investigate the different phases of reionization. But, despite several improvements have been made in the last year in this direction, the computationally-expensive nature of these models still limits the investigation of dynamical ranges larger than tens of Mpc and many of the possible assumptions on the ionizing sources, because of the typical low speed of run. This computational cost becomes even higher when hydrodynamical simulations are included for a self-consistent modeling of the galaxy formation.
For these reasons, a variety of semi-numerical formalisms have been recently proposed (Zhang et al., 2007; Mesinger & Furlanetto, 2007; Choudhury et al., 2008; Geil & Wyithe, 2008), to avoid the computational limits of the numerical simulations through approximate but efficient methods. In fact, the fundamental hypothesis of this class of models is to utilize the structure formation paradigm provided by the escursion-set formalism and/or the propagation of the I-front described by the radiative transfer through a first-order perturbation theory, allowing to build ionization maps for representative volumes of the universe with a modest computational effort.
Following these approaches, the first step to model the source distribution is to build a realization of the primordial Gaussian overdensity field at $z = 0$, that is fully determined by the cosmological scenario and the specifications for the power spectrum of density field. The host DM halos can be then identified according to the excursion-set formalism described in Section 2.3 (Mesinger & Furlanetto, 2007), then the DM particle position and velocities can be obtained by the displacement of the equal-mass particles from a uniform Cartesian lattice using the Zel'dovich approximation. Indeed, the accuracy of this tecnique is strongly dependent on the range of wavenumbers present in the IC grid, that determine the initial power spectrum sampling.
Other alternative ways have been implemented by Choudhury et al. (2008), displacing the Lagrangian overdensity field to the redshift of interest through the Zel'dovich approximation and making use of Friends-of-friends (FoF) algorithms to find the collapsed objects. This method is widely used in numerical simulations to identify all pairs of particles having a characteristic separation b or less, designated as friends; the DM halos are sets of particles that are connected by one or more friendship relationship, i.e. friends-of-friends. The linking length is usefully parameterized as a density,

$$\rho_{min} = \frac{3\bar{M}_p}{2\pi b^3} \ , \tag{4.34}$$

where $\bar{M}$ is the average mass of a particle in the simulation. Hence, the above equation represents the density of a sphere of radius b containing two particles of average mass. In the regions where the density is higher that ρ_{min}, the particles will be closer than b and will be linked toghether by the FoF algorithm. Then, the effect of this method is to identify all the peaks in which the density is greater than the threshold ρ_{min}. Another parameter required by this approach is the minimum number of particles in a halo, N_{min}, introduced in order to reject spurious objects, that would not be persistent in the simulation, and should be usually set to large suitable values to avoid this inconvenient. Anyway, this approach could introduce some uncertainties, primarly due to the inability of the code to distinguish between single DM halos and clusters of halos, since a region in which $\rho > \rho_{min}$ is classified as a unique collapsed object. Moreover, the arbitrariness and the ineffectiveness of the N_{min} parameter do not allow a good distinction of small halos from noise. Although a fixed linking lenght $b \approx 0.2$ (in units of mean inter-particle separation) is found to give a good match of the theoretical mass function of the small mass halos (Springel et al., 2005), the use of an adaptive linking length, depending on the redshift of interest, is more suitable, when the IC are created through the Zel'dovich approximation (see Choudhury et al., 2008, for more details).
Once determined the structure formation paradigm, another fundamental point is to address the ionization and the recombination of the IGM. In most of the proposed models (Mesinger & Furlanetto, 2007; Choudhury et al., 2008), the IGM ionization is introduced analogously to the analytic and semi-analytic approaches, assuming a linear relation between the masses of the ionized region and the inner DM halo fixing the ionization efficiency ζ such that the reionization epoch is in agreement with the observations. On the other hand, the recombination effects in high density regions can be modeled by the self-shielding criterion. In fact, in order to be ionized, a point should satisfy the following condition

$$\tau(\mathbf{x}) = n_{\rm HI}(\mathbf{x}) L_J(\mathbf{x}) \sigma_{\rm HI} \leq 1 \ , \tag{4.35}$$

being $L_J(\mathbf{x})$ the local Jeans length, in physical units, that determines the local HI column density and $\sigma_{\rm HI}$ the photoionization cross section of HI. The local HI density $n_{\rm HI}(\mathbf{x})$ (in physical units) can be estimated assuming the ionization equilibrium, $n_{\rm HI} = (\alpha_r/\Gamma)n_{\rm H}^2$ where α_r is the recombination factor and Γ the photoionization rate, that depends on the local mfp of the photons and the emissivity of the source.
An alternative method has been implemented by Geil & Wyithe (2008) following the approach proposed by Wyithe & Loeb (2007) and Wyithe & Loeb (2007). The fundamental idea of these methods is to express the ionized fraction $Q_{\delta,R}$ of a given region of size R as a function of its inner overdensity δ as follows

$$\frac{{\rm d}Q_{\delta,R}}{{\rm d}t} \propto Q_{\delta,R}\frac{\partial F_{coll}(\delta,R,z,M_{ion})}{\partial t} + (1-Q_{\delta,R})\frac{\partial F_{coll}(\delta,R,z,M_{min})}{\partial t} \tag{4.36}$$

$$- \alpha_r C n_{\rm H}\left[1+\delta\frac{D(z)}{D(z_{obs})}\right]Q_{\delta,R}\ . \tag{4.37}$$

In the above equation, the production rate of ionizing photons in neutral regions is assumed to be proportional to the collapsed fraction F_{coll} of mass in halos above the minimum threshold mass for star formation (M_{min}), while in ionized regions the minimum halo mass is limited by the Jeans mass in an ionized IGM (M_{ion}). Under the PS74 framework, this equation can be integrated as a function of δ, leading to the ionized volume fraction inside the regions of size R at the considered cosmological epoch.
Although applied to a analytic model, Zhang et al. (2007) implemented a formalism for the inhomogeneous IGM ionization on large scales by solving the equation of the ionization balance and the radiative transfer to first order in perturbation, that allows to investigate the ionization topology for sources with different spectral hardness and clustering properties. In this model, all the relevant processes have been included, from the photoionization and the recombination, that can be also described in a proper manner by the semi-analytic methods, to the diffusion of photons, the peculiar velocity of the baryons and the redshifting of the radiation, that are generally missing in other formalisms. The ionization equilibrium then results

$$\frac{\partial n_{\rm HII}}{\partial\tau} + \vec{\nabla}\cdot(n_{\rm HII}\mathbf{u}) = (n_{\rm H}-n_{\rm HII})\int_0^\infty {\rm d}\mu \int {\rm d}^2\mathbf{\Omega}\, n_\gamma \frac{\sigma(\mu)}{a^2(\tau)}k(\mu,n_{\rm HII,n_H}) - \frac{\alpha_r n_{\rm HII}^2}{a^2(\tau)}\ . \tag{4.38}$$

Here, $n_{\rm HII}(\mathbf{x},\tau)$ and $n_{\rm H}(\mathbf{x},\tau)$ are the local number densities of HII and H (i.e. HII+HI), respectively, that depends on the comoving coordinate $\mathbf{x}$ and the conformal time τ. The HII comoving velocity is represented by $\mathbf{u}$, while $n_\gamma(\mathbf{x},\tau,\mu,\mathbf{\Omega})$ refers to the comoving photon number density per unit solid angle ${\rm d}^2\mathbf{\Omega}$ around the propagation direction $\mathbf{\Omega}$ per unit frequency parameter μ. Finally, the factor k accounts for possible multiple ionizations. The evolution of the radiation background is affected by the sources, the photoionization process, the diffuse of photons and the redshifting, all included in the following radiation transfer equation:

$$\frac{\partial n_\gamma}{\partial\tau} + \mathbf{\Omega}\cdot\vec{\nabla}n_\gamma - H(\tau)a(\tau)\frac{\partial n_\gamma}{\partial\mu} = \frac{S}{4\pi} - (n_{\rm H}-n_{\rm HII})n_\gamma\frac{\sigma(\mu)}{a^2(\tau)}\ , \tag{4.39}$$

where $S(\mathbf{x},\tau,\mu,\mathbf{\Omega})/4/\pi$ is the differential ionizing emissivity of the sources. Taking the spatial (and angular) average of Eqs. (4.38) and (4.39), and expressing all the quantities involved by these two equations as the sum of their mean values and the first-order perturbation theory, under suitable assumptions it is possible to achieve the mean number of ionizing photons per baryon $\bar{n}_\gamma$ and the mean HII density $n_{\bar{\rm HII}}$. Moreover, their first-order perturbations can be found through the Fourier transforms of Eqs. (4.38) and (4.39). In this method, all the mentioned quantities depends on the mean value and on the first-order perturbation of S, usually related to the collapsed fraction of the region. In an analytic formalism such as PS74, it can be expandend in Taylor series, allowing to investigate the evolution of the IGM ionization (see Zhang et al., 2007, for details).

4.5 The numerical approaches

The previously mentioned methods have the big advantage to allow a picture of the reionization scenario in relatively short computational times. Anyway, they represent approximate ways to

investigate the detailed features of reionization, such as the typical radius of the HII regions. Moreover, they cannot allow a theoretical description for further and more complicated processes as, for example, the feedback or other mechanisms typically related to the still unknown nature of the sources. As a consequence, the numerical simulations, despite the required computational efforts, still represent the best methods to investigate the morphology and the evolution of reionization, and are widely used in literature (Gnedin, 2000a; Ciardi & Loeb, 2000; Sokasian et al., 2003; Ricotti & Ostriker, 2004a; Iliev et al., 2006a; Trac & Cen, 2007; Santos et al., 2008; Croft & Altay, 2008; Iliev et al., 2008a; Baek et al., 2009; Thomas et al., 2009).
In this approach, the ionizing sources distribution is generally provided by N-body simulations of structure formation, that follow the trajectories of many massive particles under the effect of physical forces, that is gravity in this case. These computations are in general performed in comoving coordinates and under the assumption of periodic boundary conditions, so that a finite, expanding volume is embedded in an appropriately perturbed background spacetime.
The DM is represented as particles sampling the phase space distribution, which evolve in time following the well known Newton's laws in comoving coordinates:

$$\frac{\mathrm{d}\mathbf{x}}{\mathrm{d}t} = \frac{\mathbf{v}}{a} \tag{4.40}$$

$$\frac{\mathrm{d}\mathbf{v}}{\mathrm{d}t} + H\mathbf{v} = \mathbf{g} \tag{4.41}$$

$$\nabla \cdot \mathbf{g} = -4\pi G a[\rho(\mathbf{x}, t) - \bar{\rho}(t)] \ , \tag{4.42}$$

from which the trajectory of the particle can be achived through second-order integration schemes. Although higher-order methods can be used, the precision on the trajectory of the particles is usually reduced in favour of a more accuracy on the mass resolution. The art of N-body simulations relies on the computational algorithm used to find the gravitational force, in principle calculated as the force between two particles of finite size in order to prevent the formation of unphysical tight binaries and is an inverse square law of their distance. Actually, evaluating the forces through a direct sum over all particle pairs has computational prohibitive costs, in particular when the number of the particle is high, since N^2 operations would be required. For these reasons, several optimization have been implemented in order to compute the gravitational field reducing the number of needed operations. A first attempt has been made by Barnes & Hut (1986) through the so called Barnes-Hut tree algorithm, dividing the space recursively into a hierarchy of cells, each containing one or more particles. These cells can be eventually treated as pseudo-particles located at the center of mass. In this way, the number of the requested operation is $0(N \log N)$, the same provided by the alternative way of the Particle-Mesh (PM) algorithms. This is based on the representation of the gravitational potential on a Cartesian grid, which is then used to solve the Poisson's equation. In this method, the mass density field is first computed on such mesh, providing the Poisson's equation solution for the gravity field (or its potential, that can be differenced to obtain the gravity field), that is finally interpolated back to the particles. Anyway, its force resolution is limited by spatial grid. This limitation can be removed by supplementing the forces with a direct sum over pairs separated by less than two, or more grid spacings, resulting in a particle-particle/particle-mesh ($\mathrm{P^3M}$) or adaptive $\mathrm{P^3M}$ algorithms. An alternative is represented by the multiresolution mesh methods, that allow to place the desired levels of mesh refinements where required so that to directly solve the Poisson's equations on multiple grids. Indeed, in order to build a reliable simulation, such numerical models should be characterized by an accurate mass (i.e. high number of particles) and spatial (force-softening length comparable to the box size) resolutions, with a subsequent increase of the computing time and a possible limitation of the allowed dynamic range.
Another great difficulty related to the numerical approaches is the computing of the I-front evolution, described by the radiative transfer equation

$$\frac{\partial I_\nu}{\partial t} + \frac{\mathbf{n} \cdot \nabla I_\nu}{\bar{a}} - H(t)\left(\nu \frac{\partial I_\nu}{\partial \nu} - 3I_\nu\right) = \eta_\nu - \chi_\nu I_\nu \ , \tag{4.43}$$

where $I_\nu(t, \mathbf{x}, \mathbf{n}, \nu)$ is the monochromatic specific intensity of the radiation field, $\mathbf{n}$ is a unit vector representing the direction of propagation and $\bar{a}$ is the ratio of cosmic scale factors between photon

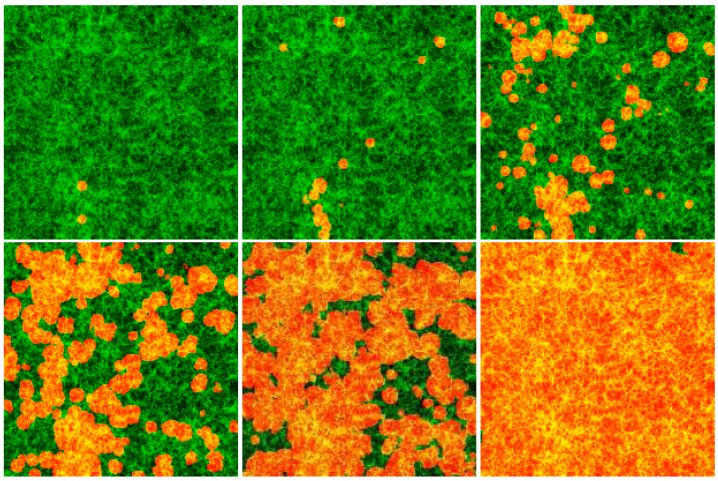

Figure 4.4: Slices through the simulation volume at $z = 18.5, 16.1, 14.5, 13.6, 12.6$ and 11.3. Green and yellow shares refer to the density field in neutral and ionized regions, the red bubbles are the HII regions (see Iliev et al., 2006a, for details).

emission at frequency ν and the time t. The parameters η_ν and χ_ν represent the emission and absorption coefficients, respectively, and, in principle, fully determine the solution of the equation. Actually, the high dimensionality of the problem and the lack of particular symmetries joined to the required accurate resolution render the above equation solvable only using numerical schemes and approximations like ray-tracing (Cen, 2002; Shapiro et al., 2004; Bolton et al., 2004; Iliev et al., 2005), Monte-Carlo methods (Ciardi et al., 2001), local depth approximations (Gnedin & Ostriker, 1997) and others.
As already stressed, other limitations rise from the difficulty to reconcile the high resolution and the large simulation box needed to accurately implement both the source and the gas physics. Most of investigation efforts have been made on small regions of space ($\sim 10 - 50$ comoving Mpc), since at the early phases the IGM ionization is driven by the smaller collapsed objects given their higher density distribution. As a consequence, the ability of a simulation in the treatment of such small DM halos is strongly related to its resolution but, on the other hand, the produced HII regions are expected to grow on larger scales due to their overlap, reaching tens of Mpc and requiring a large simulation box. Moreover, for most of the radiative transfer schemes, the computational cost grows proportionally to the number of the involved sources, reducing the possible effective volume accessible by the simulation. On the other hand, given their high accuracy, these methods can be useful tools in the investigation of the HII bubble around single sources.
Finally, a closely related problem that could be suitably addressed, in particular in the hydrodynamical simulations, is the inhomogeneous structure of the IGM, that can be implemented using sophisticated tools to generate the gas distribution over large ranges of spatial and density scales. When combined to the radiative transfer schemes, these methods can describe the propagation of the I-front in an inhomogeneous IGM, which is otherwise a very difficult problem.

The power of the semi-numerical and the numerical simulations lies in the possibility to paint 'reionization maps', spatially locating the HI and HII regions over a given realization of the universe at a choosen redshift. Through these maps, it is possible to investigate in details the morphology of the ionized regions, estimating their typical size at the fixed z, and to determine their evolution throughout the recombination epoch. An example of the possible spatial distribution of the ionized regions is shown in Fig. 4.4, predicted by the numerical simulations of Iliev et al. (2006a). In the initial neutral universe (green regions), the HII regions (red bubbles) arise in the high-density peaks with a small characteristic size. But, as reionization proceeds, their overlap allows the formation of larger bubbles and their typical radius increases until the universe is fully ionized. A similar analysis can be made also for the HeI reionization, predicting its spatial distribution at low redshifts, as shown in Fig. 4.5.

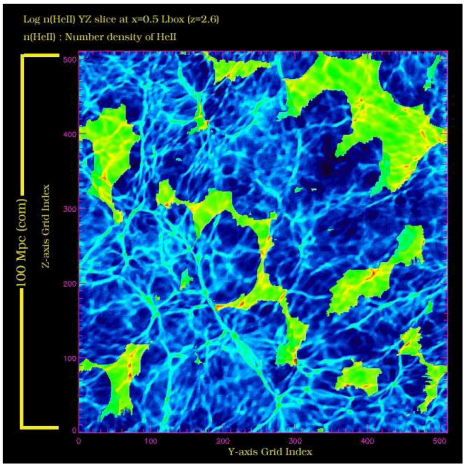

Figure 4.5: A slice showing the He III (darkened regions) and He II 3D mass distribution at z=2.6 (Paschos et al., 2007).

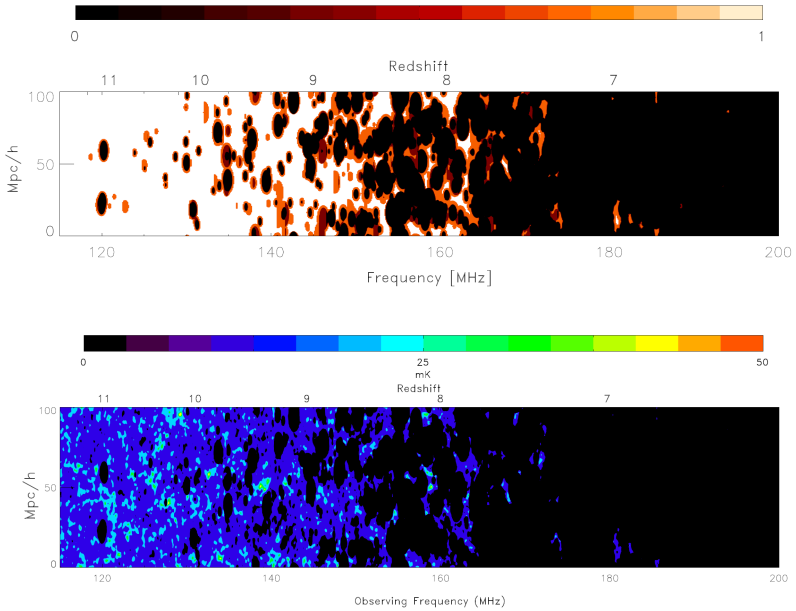

Figure 4.6: A slice along the frequency direction for the HI fraction, computed assuming quasar-like sources, is shown in the top panel. Here, the (white) HI regions abundance is reduced by the QSO ionization until $z \sim 6$, when all the IGM is ionized (black). The bottom panel shows the corresponding δT_b fluctuations on the CMB temperature due to the HI emission at the 21-cm wavelength (Thomas & Zaroubi, 2008).

These maps allow to reconstruct the IGM ionization history, for which an example is shown in the top panel of Fig. 4.6, where the ionized (black) regions become larger and larger as the redshift increases until the end of reionization. These information could be achieved from the future observations of the new interferometers through the detections of the temperature fluctuations on the CMB due to the 21-cm emission, that can be directly compared to the predictions of the theoretical models, shown in the bottom panel of Fig. 4.6 for several cosmological epochs. These future observational constraints will be powerful tools to deeply investigate the reionization evolution, and as a consequence the structure formation scenario.

Chapter 5

The reionization evolution in quintessence universes

This chapter discusses the resulting reionization evolution in alternative cosmological scenarios probed by quintessence. In the following discussion, the DDE (dynamic dark energy) component has been associated to a self-interacting scalar field evolving under the action of the potential V, for which in this work we assume the behaviour provided by the two different models, RP and SUGRA, introduced in Chapter 1. The evolution of the quintessence has been computed setting $w(z = 0) = -0.83$ and -0.85 for the RP and SUGRA models, respectively, still in agreement with the last observational tests on the SNIa.
Finally, the DDE models have been introduced in the theoretical approaches of F04 and F05 to make predictions on the morphology of the HII bubbles and to investigate the global evolution of reionization. We will present the outcoming history of the IGM ionization moving in the footsteps of the F05 analysis, but showing just the most relevant results to outline how reionization goes on in the quintessence cases and comparing our predictions to the 'concordance' ΛCDM universe, that will represent our reference case.

5.1 The IGM ionization

The aim of this section is a first investigation of the evolution of the HII regions neglecting the recombination contribution. As already stressed in the previous chapter, the statistical properties of the bubbles can be described through the analytic method proposed by F04, whose fundamental basis is the linear relation between the masses of the ionizing source and the ionized regions (Eq. 4.1). Through this assumption it is possible to derive the ionization state of the IGM and the detailed features of the HII regions from the DM halos statistical properties. Hence, the first step is to compute the minimum collapsed mass at each cosmological epoch, that can be achieved from the $M - T$ relation proposed by Barkana & Loeb (2001):

$$T_{\rm vir} = 1.98 \times 10^4 \Big(\frac{\mu}{0.6}\Big)\Big(\frac{M}{10^8 h^{-1} M_\odot}\Big)^{2/3}\Big[\frac{\Omega_{\rm m}}{\Omega_{\rm m}^z}\frac{\Delta_v}{18\pi^2}\Big]^{1/3}\Big(\frac{1+z}{10}\Big){\rm K}\ . \tag{5.1}$$

In the above equation, $T_{\rm vir}$ is the virial temperature of a halo having mass M and μ is the mean molecular weight of its gas. In order to take into account the fact that the IGM inside a HII region is not totally ionized because of the ionization equilibrium assumption, here we prefer to set μ to the mean of the values discussed in Barkana & Loeb (2001). Anyway, we checked that fixing the molecular weight to the value corresponding to a fully ionized IGM ($\mu = 0.6$) does not significantly affect the model predictions on the observables discussed in this chapter. For example, using $\mu = 0.6$ changes the Ly-α flux transmission by $\sim 1\%$ only, irrespectively of the considered cosmological model. The values for Δ_v and for the redshift evolution of $\Omega_{\rm m}(z)$ are computed consistently for the different cosmologies, setting $\Delta_v(z) = 18\pi^2 + 82d - 39d^2$ with $d = \Omega_m(z) - 1$ (Bryan & Norman, 1998) and $\Omega_m(z)$ through Eq. (1.36) of Chapter 1 and computing $H(z)$ according to the quintessence model.

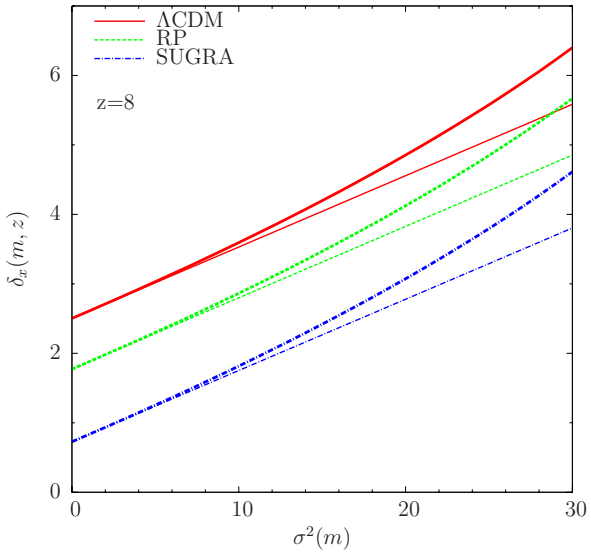

Figure 5.1: The ionization barrier is here shown at $z = 8$, assuming an ionization efficiency $\zeta = 6$. For each cosmological model, the thick line represents δ_x as defined in equation (1.15), while the thin line is its linear approximation. The curves refer to the ΛCDM model (solid line), RP model (dashed line) and SUGRA model (dotted-dashed line).

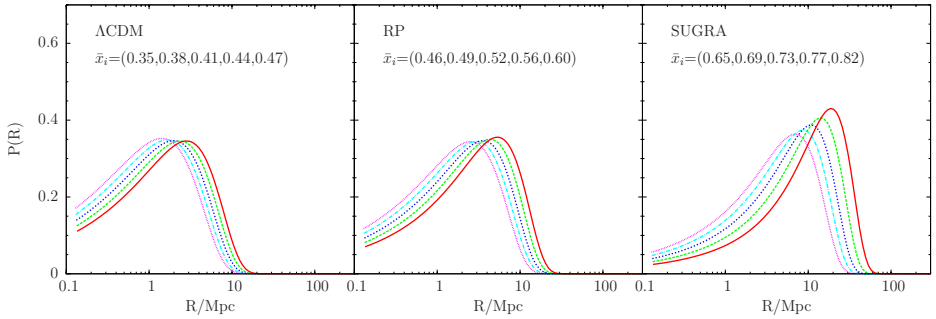

Figure 5.2: The morphology of the HII regions. The probability distribution of the bubble sizes is computed here neglecting recombination. In each panel (corresponding to different cosmological models), the curves refer to different epochs: $z = 8.8$ (dotted line), 8.6 (dotted-dashed line), 8.4 (short-dashed line), 8.2 (long-dashed line) and 8 (solid line). The corresponding values for the ionized volume fraction $\bar{x}_i$, computed assuming a ionization efficiency $\zeta = 6$, are also reported.

Eq. (5.1) then shows that the presence of a dynamic quintessence component affects the hierarchic evolution of the ionized regions, since the minimum collapsed mass is higher in the DDE universes because of the earlier growth of matter perturbations. As a consequence, the formation of larger ionized regions is enhanced, when the same ionization efficiency is fixed in all the considered cosmological cases.

This trend can be seen also through the analysis of the ionization barrier. In fact, even if the assumption of a linear ionization barrier is still correct, this is lower than in the ΛCDM universe. This is evident in Fig. 5.1, where we show the behaviour of the ionization barrier in the three different cosmological models, computed at $z = 8$ assuming $\zeta = 6$.
This implies a higher probability that matter fluctuations go beyond the ionization threshold. Consequently the density of bubbles increases, resulting in a different morphology of HII regions in the three cosmologies considered, as shown in Fig. 5.2. The earlier growth of the matter fluctuations in the quintessence models causes a faster evolution of the mass function with respect to the ΛCDM universe and a remarkable increase of the density of the largest regions. As a consequence, at the same cosmological epoch, we obtain a higher ionized fraction $\bar{x}_i$ in the quintessence cases.

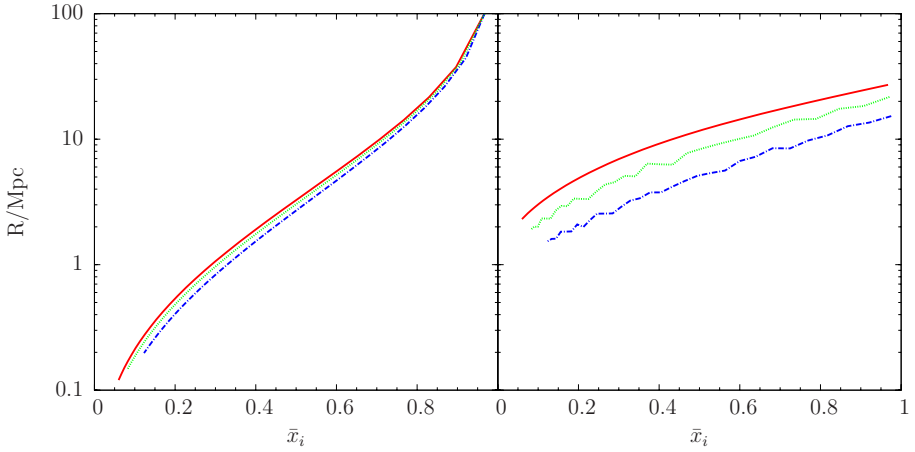

Figure 5.3: The bubble morphology. The evolution of the bubble radius as a function of $\bar{x}_i$ is shown here neglecting recombination (left panel) and in the recombination limit (right panel). Solid, dotted and dotted-dashed lines are for ΛCDM, RP and SUGRA models, respectively. A complete reionization at $z = 6$ is assumed here.

As an illustrative example, we observe that at $z = 8.8$, reionization is at its initial phases in the 'standard' universe ($\bar{x}_i = 0.35$) while for the SUGRA cosmology this epoch corresponds to its late stages, $\bar{x}_i = 0.65$. This is almost a factor ~ 2 larger than in the 'standard' case. Similarly, at $z = 8$ reionization is at the final stage in the SUGRA universe, $\bar{x}_i = 0.82$, while $\bar{x}_i = 0.47$ for the 'concordance' model.

The evolution of the characteristic radius of the ionized regions $R_{\rm char}$ is shown in Fig. 5.3, for the different phases of the reionization, as obtained by fixing ζ such that reionization ends at $z = 6$ (note that ζ is not the same for the three models). Neglecting the recombination limit, the effects of the quintessence are obvious at the early stages of reionization, since $R_{\rm char}$ (representing the radius for which the bubbles distribution is maximum) is larger in the standard universe than in RP and SUGRA models. For example, at $x_i \simeq 0.2$ $R_{\rm char} = 0.4, 0.6$ Mpc for ΛCDM and SUGRA, respectively. But the difference becomes increasingly smaller as reionization proceeds. This is caused by the different saturation regime of the IGM in the quintessence cosmologies. Ionized regions are smaller in the RP and SUGRA models at the beginning of reionization and their sizes evolve faster than in the ΛCDM universe due to the presence of large neutral voids around them, reaching the characteristic radius of the standard model in the final stages of reionization.

The F04 model and its further improvements in F05 allows the investigation of the hierarchic history of the HII regions. In fact, as already stressed, linear barrier approximation can be easily extended to the Lacey & Cole (1993) formalism to obtain the progenitor distribution, that estimates the fraction of the universe inside a bubble of a given radius. The predicted $n_b(M, z|M_b, z_b)$ at $z = 10$ in bubbles with $M_b = 10^{11}, 10^{12}$ and 10^{15} $M_\odot$ at $z_b = 8$ is shown in the left panel of Fig. 5.4 for the three different cosmological models, normalized to the mean total ionized fraction at $z = 10$ (corresponding to $\bar{x}_i = 0.22, 0.30$ and 0.45 for ΛCDM, RP and SUGRA respectively). In all the considered cases, we can see that larger objects contain large ionized regions at early times, while the opposite is true for the HII bubbles at low mass value, since the progenitors should be smaller than the final region. Moreover, the size distribution for the quintessence cosmologies is peaked at a typical radius that becomes higher and higher than the standard ΛCDM universe as the final mass M_b increases. This is a consequence of the enhanced production of larger HII regions due to the quintessence, that increases the characteristic size of the bubbles. On the other hand, fixed the final mass of the object, if the radius of its progenitors becomes higher in RP and SUGRA models, the probability that such regions merge in M_b is reduced. This can depend not only on the progenitor distribution at $z = 10$, but also on their merging probability.

Another way to investigate the progenitor distribution is to estimate the ionized fraction inside

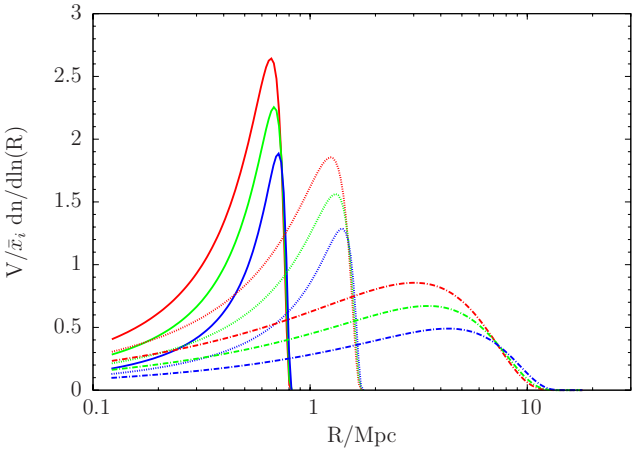

Figure 5.4: The hierarchic history of the HII regions. The progenitor distribution has been shown here for the ΛCDM (red line), RP (green line) and SUGRA (blue line) cosmologies, assuming the final mass $M = 10^{11} M_\odot$ (solid line), $10^{12} M_\odot$ (dotted line) and $10^{15} M_\odot$ (dot-dashed line) at $z_b = 8$. The results, computed at $z = 10$, are obtained assuming $\zeta = 6$.

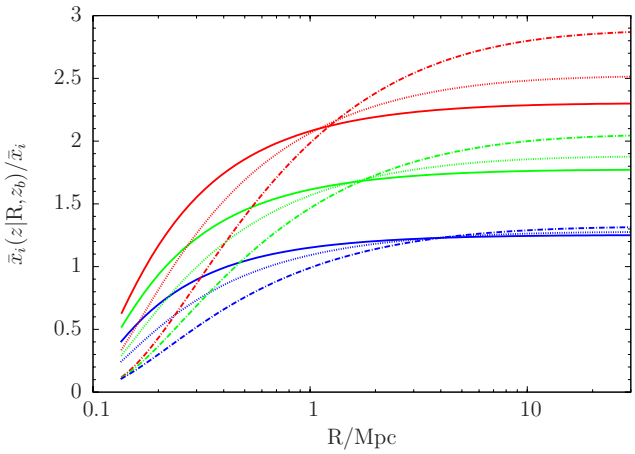

Figure 5.5: The history of the ionized fraction within bubbles relative to the global mean. The red, green and blue sets of curves refer to the ΛCDM, RP and SUGRA cosmologies, respectively. For each case, the ionized fraction inside the final bubbles, at $z_b = 8$, having the radius in the ordinate R has been computed for $z = 10$ (solid line), 12 (dotted line) and 15 (dot-dashed line).

the HII regions. This is shown in Fig. 5.5, when the different sets of curves for every considered cosmology refers to the inner $\bar{x}_i$ of a bubble at z_b with radius R produced by the progenitors at $z = 10, 12$ and 15, normalized to the mean ionized fraction $\bar{x}_i(z)$. It is evident that large bubbles are ionized earlier than average, while while the opposite is true for the smaller regions. This trend is a further indication of the 'inside-out' nature of reionization, since bubbles much smaller than the characteristic size appear only in underdense regions, which contain few ionizing sources. Anyway, the reduction of the HII amount in such bubbles is milder in the quintessence cases, since at a fixed epoch the production of DM halos is enhanced and as a consequence the I-front can easily propagate inside the low-dense regions, with a resulting acceleration of the reionization process. Another difference with respect to the standard reference universe consists in the time-evolution of the inner HII fraction in a given bubble. In fact, although for lower radius $\bar{x}_(z|R, z_b)/\bar{x}_i$ increases for all the considered cosmologies, its decreasing at the higher R values is less enhanced in the RP and SUGRA models. This is due to the larger characteristic size of the HII regions in the quintessence universes, since to form the same large bubble at z_b the required HII amount is roughly the total ionized fraction at z in the SUGRA case, implying that the bubbles are more

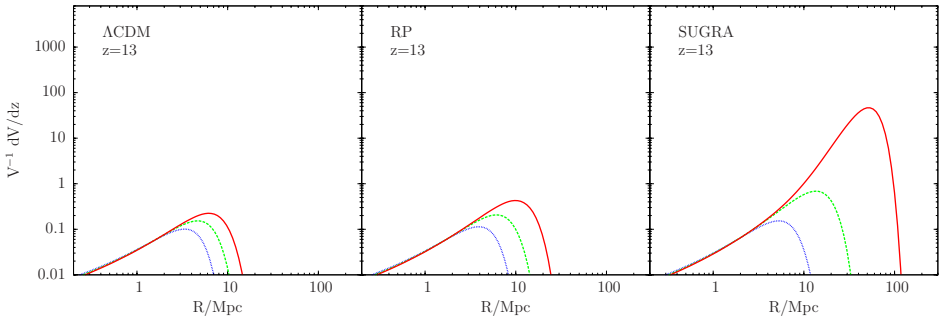

Figure 5.6: The hierarchic growth of bubbles. In each panel (corresponding to different cosmological models), we show the fractional volume accretion rate of an HII region having mass $M_1 = 10^{14} M_\odot$ that merges with a mass corresponding to a given radius R. The results, computed at $z = 13$, are obtained assuming different ionization efficiencies: $\zeta = 10$ (dotted line), $\zeta = 20$ (dashed line) and $\zeta = 30$ (solid line).

overlapped at z than in the ΛCDM framework, for which the inner $\bar{x}_i$ at z_b could be almost 3 times higher.

With the analysis of the progenitor distribution, the investigation of the bubble merger rate is also possible. As already mentioned, the merging with neighbouring HII regions is one of the fundamental factors allowing the growth of the bubble after reaching the ionization equilibrium, then it is interesting to investigate how the DDE component affects the bubbles' merger rates. As an example, Fig. 5.6 shows the merger probability of a region with mass $M = 10^{14} M_\odot$ at $z = 13$ for the ΛCDM, RP and SUGRA universes. Similarly to the ΛCDM case, also for the quintessence cosmologies the evolution of the bubbles is dominated by merging events between large systems, in particular in the late stages of the reionization process. The main difference is given by the size of the involved regions. For the RP and SUGRA models the merger probability is higher with bubbles that are even one order of magnitude larger than in the standard universe.

5.2 The recombination limit

5.2.1 The HII morphology

We can now investigate how the recombination limit due to the IGM clumpiness affects the geometry and the evolution of the ionized regions in the quintessence universes. In doing this, we should first recall that we will use the F05 model extended for the treatment of the inhomogeneous gas distribution, implemented through the MHR00 semi-analytic approach.
As discussed above, the DDE component causes the matter fluctuations to grow earlier. Hence, since the clumping of the gas depends on the inner overdensity of the bubbles, recombination is stronger already at smaller scales in the quintessence universe, compared to the ΛCDM case. Thus, the HII regions reach the ionization equilibrium on scales smaller than in the standard model.
This is clear in Fig. 5.5, where we present three different stages of reionization. While the ionization threshold does not significantly change between ΛCDM and SUGRA models, the recombination barrier $\delta_{\rm rec}$ extends to smaller scales in the quintessence universes. This effect is more prominent at the late stages of reionization process, since the bubbles reach the equilibrium on scale of the order of $20 - 30$ Mpc in the ΛCDM universe instead of the ~ 10 Mpc predicted for SUGRA. In dynamic dark energy universes, the 'earlier' (in term of comoving scales) recombination barrier involves a smaller value for $R_{\rm max}$, computed as the cross-point of δ_x and $\delta_{\rm rec}$. The same trend was already evident in Fig. 5.7, where the assumed values for ζ were such that $\bar{x}_i(z = 6) = 1$. A peculiarity with respect to the standard model is the discontinuous recombination barrier found for the SUGRA cosmology, that crosses the ionization threshold more than once. To avoid further complications to the model, we choose to set $R_{\rm max}$ to the mean value of those achieved at the cross-points (which are in any case very close to each other).

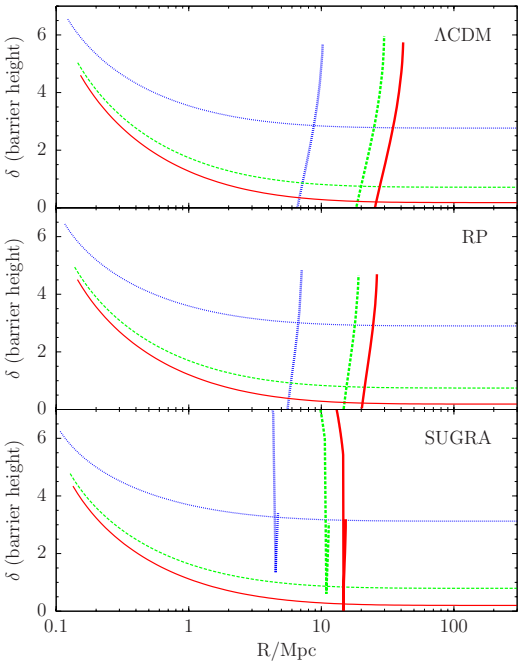

Figure 5.7: The recombination limit. In each panel (corresponding to different cosmological models), we show the ionization barrier, computed as in F04 (thin curves), and the recombination barrier, computed as in F05 (thick curves). The results are shown at three different stages of reionization: $\bar{x}_i = 0.49$ (dotted lines), $\bar{x}_i = 0.82$ (dashed lines) and $\bar{x}_i = 0.95$ (solid lines) at $z = 6$.

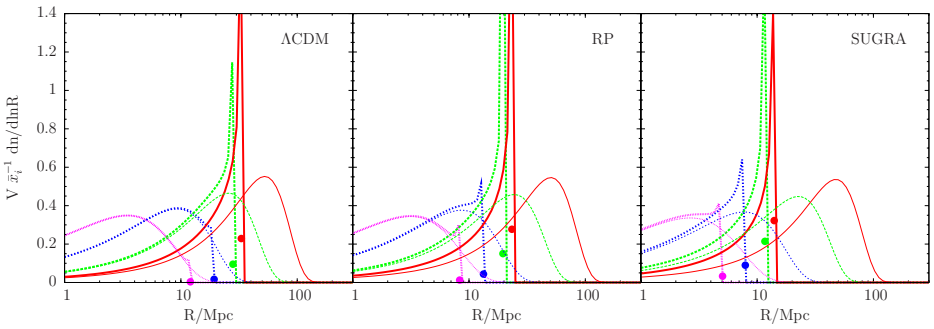

Figure 5.8: The bubble size distribution considering the recombination process. The mass distributions show that in the recombination limit (thick curves) bubbles pile up at $R = R_{\rm max}$, while neglecting recombination (thin curves) they can reach sizes larger than $R_{\rm max}$. In each panel (corresponding to different cosmological models), the different curves refer to the HII regions distribution at different stages of reionization: $\bar{x}_i = 0.51$ (dotted line), $\bar{x}_i = 0.68$ (short-dashed line), $\bar{x}_i = 0.84$ (long-dashed line), $\bar{x}_i = 0.92$ (solid line) assumed for $z = 8$. The filled points represent the volume fraction in bubbles with $R = R_{\rm max}$ in the recombination limit.

As expected, the effects of the recombination limit are enhanced on the distribution of the bubbles, that is shown in Fig. 5.8 for $z = 8$ at different stages of reionization. As a result, the HII regions with $M < M_{\rm max}$ tend to pile up on < 10 Mpc scales in the SUGRA universe, in particular at the end of reionization, while they remain quite large, $R \sim 30$ Mpc in the standard universe. Furthermore, the drop of the ionization threshold causes an increase of the volume fraction contained in the recombination-limited regions.

Moreover, since it determines the typical size of the HII bubbles, the gas recombination can affect also the time-scale in which the overlap phase occurs. In fact, for a random point in the IGM, the reionization process can be considered complete when the point joins a sphere with $M = M_{\rm max}$. Then, since $R_{\rm max}$ is smaller in the quintessence cosmologies, the density of the points belonging

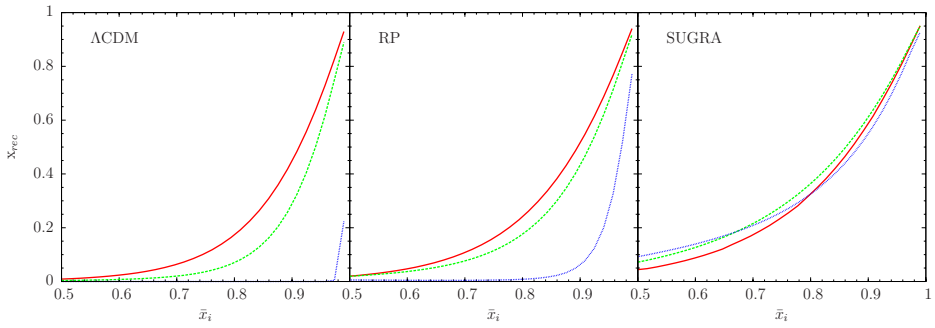

Figure 5.9: The ionized volume fraction. In each panel (corresponding to different cosmological models), the curves refer to the volume fraction contained in recombination-limited bubbles during the overlap phase at different redshifts: $z = 6$ (solid line), $z = 9$ (dashed line) and $z = 12$ (dotted line). The results are computed assuming the MHR00 model with $\lambda_0 = 60$ kms^{-1}.

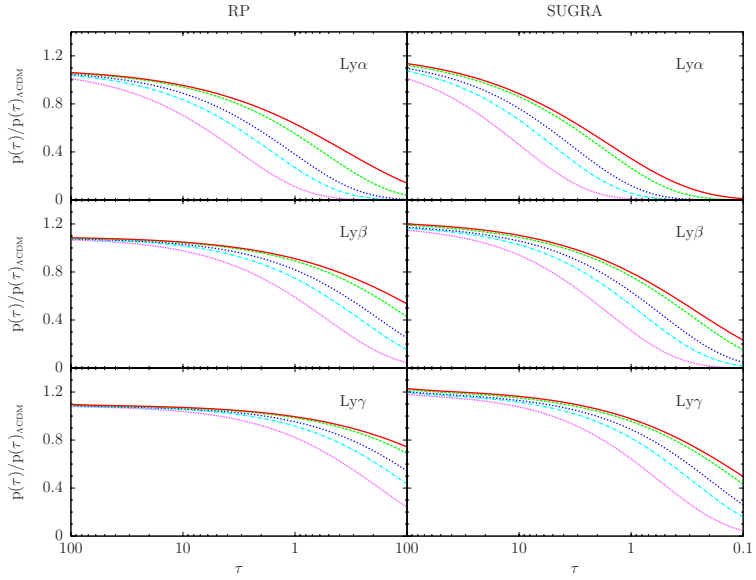

Figure 5.10: The Lyman transitions. The probability distribution of the IGM optical depth $p(\tau)$ for the quintessence models is compared to that in the 'standard' universe ($p(\tau)_{\Lambda CDM}$). Results for the RP and SUGRA models are shown in the panels in the left and right columns, respectively, and refer to Lymanα, Lymanβ and Lymanγ, in the different panels, from top to bottom. The curves are computed in the case of complete reionization ($\bar{x}_i = 0.95$) at $z = 6$ for different values of $R_{\rm max}$: 10 Mpc (dotted line), 20 Mpc (dotted-dashed line), 30 Mpc (short-dashed line), 60 Mpc (long-dashed line) and 600 Mpc (solid line).

to a region with $M > M_{\rm max}$ increases and the volume fraction inside bubbles larger than $M_{\rm max}$ becomes larger. As shown in Fig. 5.9, $x_{\rm rec}$ increases moving from the ΛCDM to the SUGRA models as reionization proceeds involving different 'epochs of overlapping'. In this case, $x_{\rm rec} \sim 0.5$ is reached earlier in the quintessence models than in the standard universe. This effect is analogous to that discussed by F05 for a small mean free path of the ionizing photons.

5.2.2 The Lyman flux transmission

As discussed in Chapter 4, the bubble morphology and the IGM ionization state affect the IGM optical depth τ and consequently the transmission of the Lyman-α flux. To investigate how the IGM optical depth distribution depends on $R_{\rm max}$ in the quintessence models, we compute the probability distribution $p(\tau)$ of the IGM optical depth for the Lyα, β, γ transmission following Eq. (4.25).
In Fig. 5.10 we compare $p(\tau)$ for the RP and SUGRA scenarios to that obtained considering the

ΛCDM model, $p(\tau)_{\Lambda\mathrm{CDM}}$, for different values of R_{max}. The transmission is lower for small values of τ. We find that the trends with R_{max} for the Lyman-β (central panels) and Lyman-γ (lower panels) are analogous to that for the Lyman-α one (upper panels).

5.3 Possible sources of bias

Given their analytic nature, the F04 and the F05 models suffers of some theoretical limitations that can introduce strong deviations on the reionization picture shown above.
The main effect on the observational results can be provided by the clustering of the source. In fact, the model we adopt is based on the extended PS74 formalism and can account only in a very approximate way, most often in the linear limit, for the source clustering, which is expected to have important effects on the morphology of the HII regions. Since the clustering amplitude depends on the source abundances, which are different in the models considered here, our results could be affected by this bias. The only suitable way to properly address this problem is to improve this semi-analytic model through the analysis of the 'reionization maps' that, as already discussed, allow to locate the ionizing source in a given realization of the universe. This investigation can be made through semi-numerical or numerical methods.
Another possible source of bias is related to the use of the semi-analytic model of MHR00 in alternative cosmological scenarios. In fact, this method is based on hydrodynamical simulations provided for 'standard' universes only, then in principle its validity could be compromised in quintessence universes. Anyway, we do not expect large differences for the IGM volume-weighted density distribution computed in the DDE cases, then we have assumed that the results of the MHR00 simulations obtained for a standard cosmology are still valid for a quintessence-dominated universe.

5.4 Conclusions

The purpose of this chapter is to give a picture of the reionization epoch in the universes dominated by a DDE component at late epochs, tracing the HII regions evolution using a semi-analytic approach based on the hierarchic growth of matter fluctuations. In doing this, we consider two cosmological models in which the dark energy density varies with time driven by the Peebles & Ratra (2003) and Brax & Martin (2000) potentials. Then, we used the theoretical approaches proposed by F04 and F05 to outline the main differences between the evolution of bubbles in the quintessence models and in the standard ΛCDM cosmology. Our main results can be summarized as follows.

1. The growth of density fluctuations occurs earlier and the ionization barrier δ_x is lower in the RP and SUGRA universes compared to the ΛCDM one. This causes a strong increase of the high-density regions with respect to the ΛCDM case at the same epoch.

2. Neglecting the recombination limit, the characteristic size of the HII regions is smaller in the RP and SUGRA cases at the early stage of reionization, but the difference is weakened as reionization proceeds.

3. In the recombination limit, the early growth of the matter fluctuations causes the increase of the IGM clumpiness and the inner recombination of the bubbles becomes more efficient. As a consequence, the HII regions reach the ionization equilibrium on slightly smaller scales and the bubble abundance tends to increase. The IGM volume fraction contained in bubbles larger than R_{max} increases requiring an earlier 'epoch of overlap' in the quintessence universe compared to ΛCDM.

4. The main effect on the high-z QSO radiation transmission due to the different evolution of the HII regions is the lower Lyman flux absorption at small optical depths in RP and SUGRA cosmologies compared to the ΛCDM model.

Chapter 6

Reionization in universes with non-Gaussian initial conditions

This chapter is dedicated to the discussion of the main results obtained from the application of the AL06 model under the assumption that the structure formation history started from a primordial non-Gaussian density field. In the following discussion, the evolution scenario of the ionizing sources has been assumed according to the Matarrese et al. (2000) formalism, that has been introduced in the AL06 model to probe predictions for the global features of reionization. In this chapter, we have made estimates for some observational quantities as the evolution of the IGM filling factor and the optical depth at the different cosmological epochs, assuming both the local and the equilateral NG cases constrained by the 5-year WMAP data. The outcoming picture has been compared to the reionization scenario obtained for the Gaussian 'reference' case. We finally discuss the possibility of constraining the degree of primordial NG through the reionization probes related to CMB-based esperiments.
A general warning should be remarked in the following discussion, concerning the NG parameter used for our predictions that, as already mentioned also in Chapter 2, we set accordingly to the last WMAP results. As pointed out by Grossi et al. (2009), the value estimated at the physical scale of CMB cannot be used to make predictions for the large scale structures, because of (although tiny) time-evolution of the gravitational potential Φ. Then, the $f_{\rm NL}$ parameter should be rescaled using the normalized growth factor of the density fluctuations, namely $f_{\rm NL} = g(z=\infty)/g(z=0) f_{\rm NL}^{CMB} \sim 1.3 f_{\rm NL}^{CMB}$, where $f_{\rm NL}^{CMB}$ is the value obtained by the CMB experiments. Anyway, the purpose of this work is just to use the AL06 model as a 'toy-model' to investigate the possible differences on the reionization picture painted in case of a non-Gassian overdensity field and the standard Gaussian universe, without making exactly predictions and focusing on the details of the different phases. Then, for such an analysis, it is not necessary to set the $f_{\rm NL}$ parameter to its effective value.

6.1 The reionization scenario

In an analogous way as that already shown for the F05 model, the AL06 approach relates the reionization observables, as the IGM filling factor and the IGM optical depth, to the statistical properties of the DM halos hosting the ionizing sources. These quantities, as shown in Chapter 4, are related to the total collapse fraction, that can be computed through the halo distribution $n_{NG}(M,z)$ once M_{min} of a given class of sources and the correspondig virial temperature are known. Then, through the same relation of Barkana & Loeb (2001) used also for the F05 model, we can compute the total collapsed fractions for the different kinds of sources here considered, following Eq. (4.30).
The resulting $F_{\rm coll}$ are presented in Fig. 6.1, where we show the collapsed fractions of Ia and Ib haloes for the local and the equilateral cases here considered and their redshift evolution compared to the predictions for the Gaussian scenario. We can notice that for both the local and the equilateral models, positive values for $f_{\rm NL}$ produce an enhancement of the collapsed fraction at a fixed

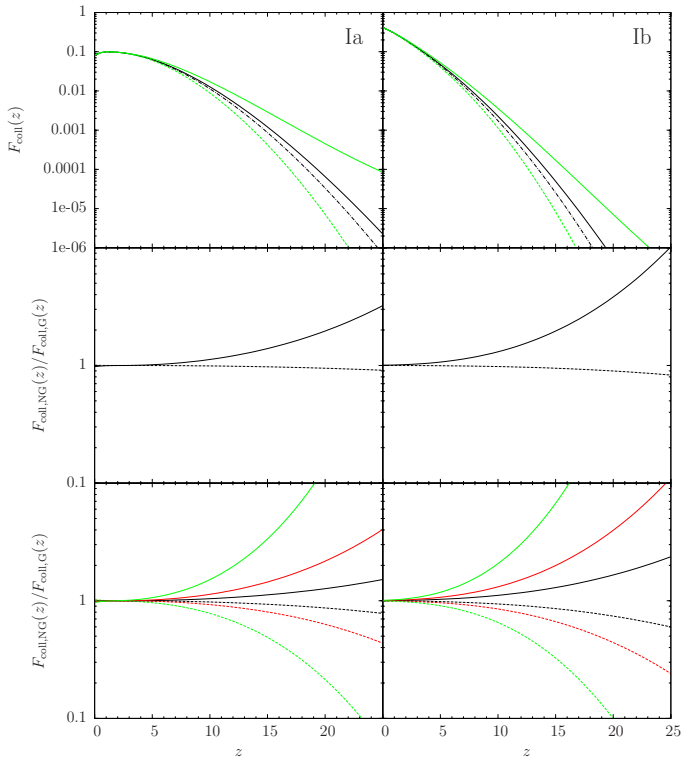

Figure 6.1: The collapsed fraction of Ia and Ib ionizing sources. The top panels show the resulting $F_{\rm coll}$ for the Gaussian reference case (dot-dashed line) and two extreme non-Gaussian models here considered, which adopt $f_{\rm NL} = 111$ with the local shape (solid line) and $f_{\rm NL} = -151, 253$ with $\alpha = -0.2$ for the equilateral shape (green dotted and solid surves, respectively). The other panels show the ratio between the collapsed fractions of Ia (left panels) and Ib (right panels) ionizing sources for non-Gaussian and Gaussian models as a function of redshift. In the middle panels the results for non-Gaussian models with local shape are shown, where $f_{\rm NL} = -9$ (dashed lines) and $f_{\rm NL} = 111$ (solid lines) are assumed. In the bottom panels, which refer to non-Gaussian models with equilateral shape, dashed and solid lines correspond to $f_{\rm NL} = -151, 253$, respectively; black, red and green lines refer to $\alpha = 0$ (i.e. no scale-dependence), $\alpha = -0.1$ and $\alpha = -0.2$, respectively.

redshift, given the larger probability for high-mass haloes in the primordial distribution. When scale-dependent non-Gaussianity is considered, this effect becomes higher as the power-law parameter α decreases. The opposite trend is observed when negative $f_{\rm NL}$ values are assumed: in this case we obtain a reduction of the non-Gaussian collapsed fraction, due to the smaller probability for high-mass haloes at high z.

As already seen in Chapter 2, the probability of the enhancement (or the reduction) of the structure formation is higher at the early phases of the evolution of the universe, i.e. when reionization begins. Then, it is expected that the different collapsed fraction due to NG could strongly affect the amount of ionized IGM at different cosmological epochs. In order to estimate the time-evolution of the IGM filling factor, we set ζ as a constant, fixed in such a way that reionization ends at $z = 6.5$. Moreover, $F_{\rm HII}$ depends on the recombination rate, that is a function of the free parameter β. Since AL06 found good consistency between the predicted and the observed τ irrespectively of the amount of primordial NG in the models they consider, we decide to set $\beta = 0$. As already mentioned, in this case the z-dependence of $C_{\rm HII}$ is neglected and $C_{\rm HII} = 10$. Anyway, the impact of the assumption of a constant clumping factor will be discussed later.
The $F_{\rm HII}$ evolution is shown in Fig. 6.2, both for local and equilateral models. As expected, a generally positive primordial NG produces an increase of the ionized IGM density, in particular the effect is evident if a scale-dependent $f_{\rm NL}$ parameter is assumed, for which $F_{\rm HII}$ can become 5 times higher than that predicted in the Gaussian case. The IGM reionization results slower when negative values are considered, since the smaller collapsed fraction produces a mild evolution of the filling factor, that is smaller compared to the Gaussian case, at every cosmological epoch.

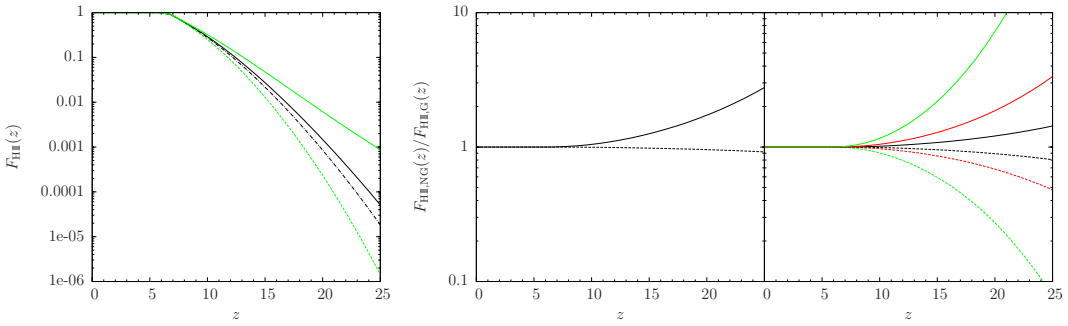

Figure 6.2: The left panel shows the evolution of the ionized fraction $F_{\rm HII}$ for the Gaussian and two different non-Gaussian models here considered, as in the top panels of Fig. 6.1. The two panels on the right show the ratio between the ionized fraction $F_{\rm HII}$ for non-Gaussian and Gaussian models as a function of redshift. In the left panel, the results for non-Gaussian models with local shape is shown, where $f_{\rm NL} = -9$ (dashed lines) and $f_{\rm NL} = 111$ (solid lines) are assumed. In the right panel, which refers to non-Gaussian models with equilateral shape, dashed and solid lines correspond to $f_{\rm NL} = -151, 253$, respectively; black, red and green lines refer to $\alpha = 0$ (i.e. no scale-dependence), $\alpha = -0.1$ and $\alpha = -0.2$, respectively.

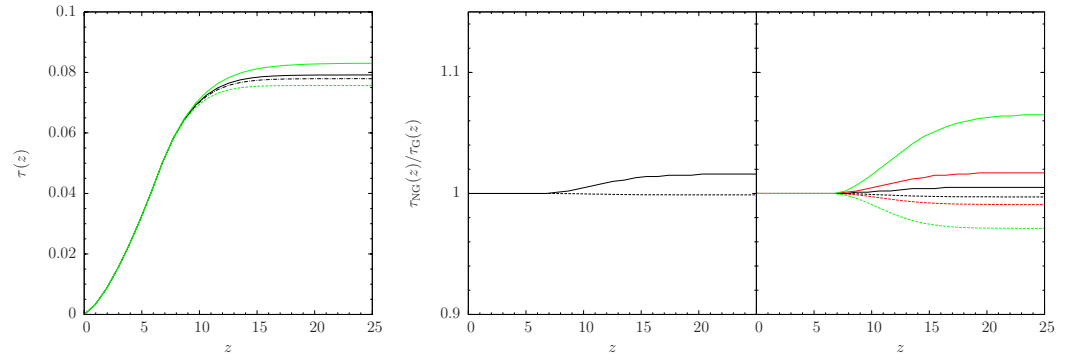

Figure 6.3: The left panel shows the evolution of the IGM optical depth τ for the Gaussian and two different non-Gaussian models here considered, as in the top panels of Fig. 6.1. The two panels on the right show the ratio between the reionization optical depth τ for non-Gaussian and Gaussian models as a function of redshift. In the left panel the results for non-Gaussian models with local shape is shown, where $f_{\rm NL} = -9$ (dashed lines) and $f_{\rm NL} = 111$ (solid lines) are assumed. In the right panel, which refers to non-Gaussian models with equilateral shape, dashed and solid lines correspond to $f_{\rm NL} = -151, 253$, respectively; black, red and green lines refer to $\alpha = 0$ (i.e. no scale-dependence), $\alpha = -0.1$ and $\alpha = -0.2$, respectively.

Finally in Fig. 6.3 we show the effects of the primordial NG on the reionization optical depth τ assuming both local and equilateral models. As a consequence of the evolution of the ionized fraction, in the initial phases of reionization the values of τ for the models with positive $f_{\rm NL}$ are higher than those predicted for the Gaussian case. In particular, when a scale-dependent NG is assumed, the change in τ is higher than 10 per cent for $\alpha < -0.2$. In this case, the non-Gaussian optical depth would be $\tau \sim 0.083$ at $z \sim 30$, that is still consistent with the last WMAP observations ($\tau = 0.084 \pm 0.016$). Assuming a local shape with largest positive $f_{\rm NL}$ here considered we find $\tau \sim 0.079$. Notice that for the Gaussian model we predict a reionization optical depth at $z = 30$ $\tau = 0.078$.

We notice that our results are in qualitative agreement with the reionisation picture resulting from the analysis performed by Chen et al. (2003). However, a direct comparison cannot be done because of the differences in the considered cosmological parameters: in particular they assume the ones suggested by the first-year WMAP analysis, with a significantly higher power spectrum normalization ($\sigma_8 = 0.9$). Furthermore, they parametrize the degree of non-Gaussianity using the expectation value of the considered modified Poisson distribution λ, that is inversely proportional to the $f_{\rm NL}$ parameter here used: $\lambda \propto 1/f_{\rm NL}$. Their results show that a high amount of primordial non-Gaussianity (small λ, i.e. high $f_{\rm NL}$) produces large deviations with respect to the Gaussian

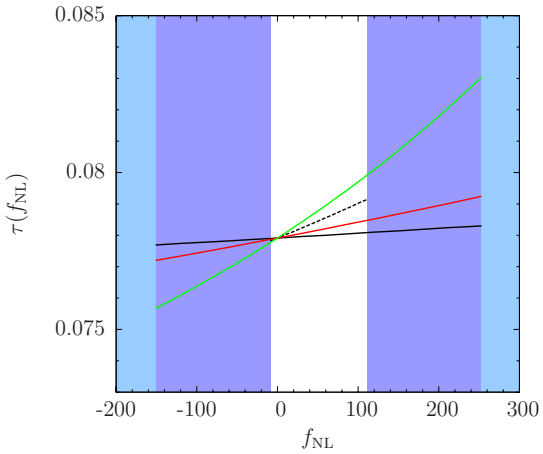

Figure 6.4: The reionization optical depth τ at redshift $z = 30$ as predicted in different non-Gaussian scenarios is shown as a function of $f_{\rm NL}$. The dashed black curve refers to the local case, while the solid black, red and green lines correspond to the equilateral case with $\alpha = 0$, $\alpha = -0.1$ and $\alpha = -0.2$, respectively. The blue and cyan rectangles represent the areas currently excluded by the WMAP observations for the local and equilateral cases, respectively.

case in the ionized fraction and the IGM optical depth, in agreement with our results. We should, however, notice that for the Gaussian reference model the estimate of τ in Chen et al. (2003) differs by 20 per cent with respect the value we predict using the 5-year WMAP cosmology.

6.2 The NG probes from reionization observables

In this section we investigate the possibility to constrain the NG deviations through the reionization observables probes at present by the last WMAP data release. For this purpose, we computed the IGM optical depth at high z predicted by the AL06 in different non-Gaussian scenarios, i.e. with different $f_{\rm NL}$ parameters set to possible values inside the ranges allowed for both the local and the equilateral cases by the 5-year WMAP data.
The predicted reionization optical depth (at $z = 30$) is shown in Fig. 6.4. Indeed, the standard deviation on the current estimate of τ from the last WMAP results ($\sim$ 20 per cent) does not allow us to strictly constrain the scale dependence of NG and, as shown by Liguori & Riotto (2008), should affect the $f_{\rm NL}$ value by a $\sim$ 3 per cent and $\sim$ 5 per cent uncertainty for the local and equilateral shapes, respectively. We estimate that in order to distinguish among the different scale dependences, a precision between $\sim$ 1 per cent ($f_{\rm NL} < 0$) and $\sim$ 8 per cent ($f_{\rm NL} > 0$) on the τ measurement is required, using CMB-like experiments. In this sense, the smaller standard deviations expected by Planck ($\sim$ 6 per cent) (Mukherjee & Liddle, 2008) could better probe the reionization optical depth and would possibly constrain the NG parameter with an uncertainty of $\sim$ 1 per cent and $\sim$ 2 per cent in the local and equilaterals models, respectively. We should, however, keep in mind that the current WMAP estimate of τ cited in this paper is affected by cosmic variance, since it is based on the bispectrum of the CMB. Recent works investigate alternative methods to avoid this problem (see, e.g. Seljak, 2009).

6.3 Possible sources of bias

The AL06 method, given its semi-analitycally nature, suffers of several theoretical limitations that can introduce strong deviations from the reionization picture described above. First of all, we stress that the description of the recombination process in the analytic model here adopted relies on some simplifying assumptions which can affect the way in which reionization occurs. A deeper investigation of the IGM statistical distribution would require the analysis of suitable numerical simulations having non-Gaussian initial conditions.
As an example of possible biases introduced by the model uncertainties, in Fig. 6.5 we show how

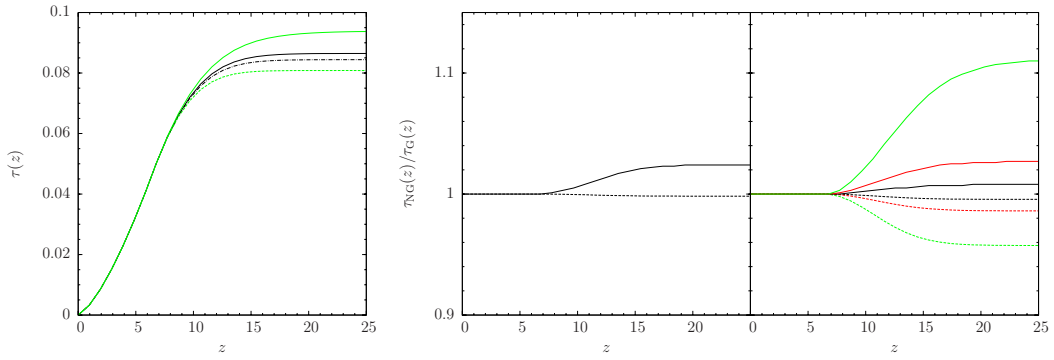

Figure 6.5: As in Fig. 6.3, but assuming $\beta = 2$ in the redshift dependence of the clumping factor.

a time-evolving clumping factor impacts the reionization optical depth. The results have been obtained by setting $\beta = 2$ in Eq. (4.31), as suggested by Avelino & Liddle (2006), for which the reionization optical depth is in agreement with the 3-year WMAP results for many NG degrees. In order to estimate the relative importance of the details of the analytic modelling of the reionization process here adopted, we can compare the IGM optical depths predicted assuming $\beta = 0$ (Fig. 6.3) and $\beta = 2$ (Fig. 6.5). As shown by the corresponding left panels, for the Gaussian model the effect on τ due to the change in β and then to the unknown IGM physics is approximately of 10 per cent. Viceversa, considering the non-Gaussian to Gaussian ratios (shown in the right panels of Figs. 6.3 and 6.5), changing β from 0 to 2 produces negligible effects on the results. In fact we find that at high z the ratios obtained with $\beta = 0$ and $\beta = 2$ differ by less than 1 per cent for the mildly non-Gaussian models and by ~ 4 per cent for the non-Gaussian models with the most extreme scale-dependence ($f_{\rm NL} = 253$). By looking at the right panel of Fig. 6.5, we notice that for this last model the effect of introducing a primordial NG can rise up to 10 per cent. This shows that the non-Gaussian to Gaussian ratios are only mildly affected by the choice of the recombination model: this justifies the fact that in this paper we preferred to show most of the results in terms of ratios in spite of absolute values.
Finally, we remark that our approach, which is based on the PS74 formalism and its extensions, cannot fully account for the source clustering, that could indeed have relevant effects on the morphology of the HII regions. Since the source distribution depends on the clustering amplitude through the bias parameter, that is different if a primordial NG is considered (see, e.g. Matarrese & Verde, 2008; Dalal et al., 2008; Carbone et al., 2008), we expect that our results could be affected by this approximation, which can be improved only with suitable numerical simulations.

6.4 Conclusions

The aim of this work was to investigate how primordial NG may alter the reionization history when compared to the standard scenario based on Gaussian statistics. We have chosen a simple analytic method to describe the physical processes acting on the IGM to make predictions on the evolution of the ionized fraction and the reionization optical depth. Our work extends previous analyses (Chen et al., 2003; Avelino & Liddle, 2006) based on simplified ways to introduce primordial non-Gaussianity, considering models motivated by inflation. In particular we assume two different hierarchical evolution scenarios for the ionizing sources, characterized by scale-independent and scale-dependent NG. All scenarios here considered are not violating the constraints coming from the recent analysis of the 5-year WMAP data. Our main conclusions can be summarized as follows:

1. NG affects the abundance of the dark matter haloes, since the formation of high-mass collapsed objects is enhanced (reduced) when positive (negative) values for the $f_{\rm NL}$ parameter are assumed. This effect is more evident at earlier cosmological epochs, exactly when reionization begins.

2. As a consequence, for positive primordial NG, the collapsed fraction in type Ia and Ib sources

is higher than for the Gaussian case at the same epoch, and the difference increases with z. The opposite result applies when $f_{\rm NL} < 0$ is assumed.

3. The IGM filling factor is higher and its evolution is faster than in the Gaussian scenario if a positive $f_{\rm NL}$ is assumed. This effect is enhanced for a scale-dependent NG, that can produce a 5 times higher $F_{\rm HII}$ with respect to the Gaussian case, at early cosmological epochs. Viceversa the filling factor is smaller and has a mild redshift evolution for negative $f_{\rm NL}$.

4. Both local and equilateral NG have a small (less than 10 per cent) impact on the reionization optical depth, but the effect is enhanced assuming a scale-dependent $f_{\rm NL}$ parameter.

We finally remark that our predictions of the reionization optical depth in non-Gaussian cosmologies are in agreement with that estimated by 5-year WMAP analysis within 1σ error bars and a precision higher than that of WMAP is required to constrain NG and its scale dependence. Ideally one would simulate reionization in non-Gaussian cosmological models using hydrodynamical simulations that incorporate all the relevant physical processes in a consistent framework (most importantly radiative transfer effects in the IGM). However, such approach is very time consuming due to the large box size and the high resolution required to simulate large volumes and, at the same time, the physics of the sources of radiation. For this reason, some approximate semi-analytic schemes such as the one presentend here are still useful especially when calibrated on the more robust results of the hydrodynamical runs.

Chapter 7

Future prospects

The aim of this chapter is to illustrate the future prospects of this Thesis work. In the previous discussion, the analysis of the reionization process in alternative cosmological scenarios has been carried out through semi-analytic approaches, basically providing the global properties of reionization and the HII regions in an approximate way. On the other hand, the future observations probed by the new interferometers will be able to investigate the IGM ionization state in a wide range of redshifts, i.e. $z \leq 9$, allowing to obtain 'reionization maps' of HI that can help us to estimate the effects due to the 21-cm emission on the CMB temperature.
For these reasons, our next step consists in building a suitable semi-numerical model for reionization, allowing us to make predictions for the HI topology that can be directly compared to future observations. In doing this, we adopt the theoretical model proposed in literature by Mesinger & Furlanetto (2007) and we will improve it by introducing a suitable treatment for the recombination of the gas.

7.1 The Mesinger & Furlanetto (2007) approach

In this section, the main bases of the semi-analytic model proposed by Mesinger & Furlanetto (2007) will be reviewed. We recall that a brief introduction to this method have been already introduced in Chapter 4. Anyway in the following discussion we will illustrate its fundamental assumptions in a deeper manner, focusing our attention on the innovative aspects concerning the IGM ionization.
The first step consists in building the ICs through which the ionizing sources involved in the reionization process can be identified. In doing this, the algorithm generates a discrete realization of the linear overdensity field at $z = 0$ inside a square box of size L and N grid points per dimension. The initial matter fluctuations are computed through a 3D Monte-Carlo simulation, assuming a Gaussian statistics, for which the Fourier components have been calculated as

$$\hat{\delta}(\mathbf{k}) = \sqrt{\frac{\sigma^2(k)}{2}}(a_{\mathbf{k}} + ib_{\mathbf{k}}) \ , \tag{7.1}$$

where $a_{\mathbf{k}}$ and $b_{\mathbf{k}}$ are consistent with a Gaussian distribution having zero-mean and unit variance. The corresponding overdensity field $\delta\mathbf{x}$ is computed through the discrete Fast Fourier Transform, in an analogous manner to that described in Chapter 2 that, hence, will not be reviewed here. Once obtained $\delta\mathbf{x}$, the Zel'dovich approximation allows to estimate the corresponding initial comoving velocity field (see Eq. 2.31, that is expressed in proper units) and its Fourier modes at a fixed redshift,

$$\dot{\mathbf{r}}(\mathbf{k}, z) = \frac{i\mathbf{k}}{k^2}\dot{D}(z)\delta(\mathbf{k}) \ . \tag{7.2}$$

As already seen in Chapter 2 and as shown by the above equation, the velocity field can be decomposed in a spatial and a time component, $\dot{\mathbf{r}}(\mathbf{x}, z) = \dot{D}(z)\mathbf{p}(\mathbf{x})$, where $\mathbf{p}(\mathbf{x})$ is the Fourier Transform of the $i\mathbf{k}\delta(\mathbf{k})/k^2$ term in Eq. 7.2. Then, the effectiveness of the Zel'dovich approximation lies in the opportunity to easily compute the velocity field at the redshifts of interest, once (and

for all) performed the spatial component calculation.
From Eq. 7.2, it is possible to estimate the integrated linear displacement at a fixed z, starting from a sufficiently high redshift z_0:

$$\mathbf{\Psi}(\mathbf{x}, z) = [D(z) - D(z_0)]\mathrm{d}\mathbf{p}(\mathbf{x}) \approx D(z)\mathrm{d}\mathbf{p}(\mathbf{x}) \ , \tag{7.3}$$

that can be used to locate the ionizing sources.
Once built the initial overdensity field, the DM halos can be identified making use of the excursion-set formalism introduced in Chapter 2. The matter fluctuation at a fixed grid point $\mathbf{x}$ can be smoothed on progressively small physical scales R_f according to Eq. 2.19 starting from L to $\mathrm{d}L = L/N$, that is the characteristic size of a pixel. Fixed a filter scale R_f, at every point of the box we check if the corresponding overdensity is higher than the collapse threshold, i.e.

$$\delta_f(\mathbf{x}, R_f) \geq \delta_c(M, z) \ , \tag{7.4}$$

in which $\delta_c(M, z)$ is set according to the improvements made by J01, already introduced in Chapter 2. Actually, filter scales large enough that $\delta(M, z) > 7\sigma$ are extremely unlike, then they have been discarded (Mesinger & Furlanetto, 2007). If the collapse criterion is satisfied, the grid point $\mathbf{x}$ is marked as the center of a DM halo having radius R_f, and will not be reconsidered in the following filter steps at smaller scales. Moreover, since a pixel is considered here as the center of the found halo, the mass contained in the spherical region of radius R_f must be assigned only to such a pixel. Then, the possible neighbouring grid points satisfying the collapse criterion that lie inside that region should be discarded. For these reasons, once identified a DM halo, we mark all the inner pixels in order to not consider them in the next filter steps. This is similar to the 'full-exclusion' criterion introduced by Bond & Myers (1996) to prevent the halo overlap.
Once the DM halos have been identified on the IC box, they can be moved to their actual position at the choosen redshift by using Eq. 7.3. For computational convenience, this step is made smoothing the velocity field onto a lower resolution grid having N', a reduced number of points per dimension. We note that the resulting halo field is now not placed on a regular grid that, for computational reasons, can be extremely inconvenient. Then, it can be an advantage to re-assign the halo masses to a regular grid, having the same resolution of the smoothed velocity field, through the usual interpolation algorithms adopted also by the N-body simulations, as the Nearest Grid Point (NGP), the Cloud In Cell (CIC) and the Triangular Shaped Cloud (TSC) methods.
The updated halo field $\delta_{hh}(\mathbf{x}, z)$ can now be used to identify the HII regions. In fact, $\delta_{hh}(\mathbf{x}, z)$ can be smoothed on progressively smaller physical scales R_f in a similar way to the filtering of the initial overdensity field and, assuming a prescription for the ionization criterion equivalent to Eq. 3.9 with a constant ionization efficiency ζ, every pixel such that

$$f_{coll}(\mathbf{x}, R_f, z) \geq \zeta^{-1} \tag{7.5}$$

is considered as ionized. In the above equation, f_{coll} is the local collapsed fraction inside a region of radius R_f at redshift z computed in the grid point $\mathbf{x}$ (note that $\mathbf{x}$ is now an Eulerian position). As already remarked, the filtering procedure is analogous to that performed to find the DM halos, but in this case R_f refers to the size of the HII region. Moreover, the HII bubble are allowed to overlap, then no 'full-exclusion' criterion has to be applied. The left-hand-side term of Eq. 7.5 can be estimated as the ratio between the collapsed mass residing in the pixels and the mass inside the sphere having the radius filter $M = 4/3\pi R_f^3 \bar{\rho}[1 + \delta_{nl}(\mathbf{x}, z)]$, where $\delta_{nl}(\mathbf{x}, z)$ is the mean overdensity at the coordinate $\mathbf{x}$ smoothed on the scale R_f. Note that in this prescription, the ionizing source is identified with its host DM halo.
The overdensity field $\delta_{nl}(\mathbf{x}, z)$ is calculated through the application of the Zel'dovich approximation on the initial matter fluctuations $\delta(\mathbf{x})$, moving the mass corresponding to the pixels ($M = M(\mathrm{d}L)$) according to Eq. 7.3 and smoothing the resulting field on the lower resolution box. We are now able, hence, to locate the HI regions inside a box representing a realization of the universe, obtaining the 'reionization maps'.
These results can be used for several kinds of investigation. As an example, through the analysis of the HI topology, we can obtain information concerning the statistical properties of the HII regions (see Mesinger & Furlanetto, 2007, for details), or the amount of HI at a fixed cosmological

epoch. But, maybe, the major opportunity consists in the estimate of the fluctuations on CMB temperature due to the 21-cm emission that reads as follows:

$$\delta T_{\rm CMB}(\mathbf{x},z) \approx 9(1+z)^{1/2} x_{\rm HI}(\mathbf{x},z)(1+\delta_{nl}(\mathbf{x},z)) \frac{H(z)}{dv_r/dr + H(z)} \ , \tag{7.6}$$

where dv_r/dr is the comoving gradient of the line of sight component of the comoving velocity at z and $x_{\rm HI}$ is the local HI fraction in the considered pixel. Hence, through the reionization maps we are able to achieve the additional contribution, produced by the HI emission, to the CMB temperature at a fixed z that can be detected by the next observations.
This semi-analytic model have been later improved by Mesinger & Dijkstra (2008), introducing a treatment for computing the ionization contribution produced by each DM halo. This allows to obtain the ionization field acting on the IGM at a fixed epoch. In particular, the total flux (measured in units of ionizing photons per second per proper square cm) in a given grid point $\mathbf{x}$ at z is

$$f(\mathbf{x},z) = \frac{(1+z)^2}{4\pi} \sum_i \frac{M_i \times \epsilon_{ion}(z)}{|\mathbf{x}-\mathbf{x}_i|^2} \exp(-|\mathbf{x}-\mathbf{x}_i|/L_{mfp}) \ , \tag{7.7}$$

where $\mathbf{x}$ and $\mathbf{x}_i$ are the locations of the cell of interest and the halo, respectively, M_i is the mass of the halo, L_{mfp} is the mfp of the photons and represents a free parameter of the model. Finally, ϵ_{ion} represents the rate at which the ionizing photons are released in the IGM per unit mass and depends on the features of the source. It can be written as

$$\epsilon_{ion}(z) = 3.8 \times 10^{58} \epsilon_{fid} \left[\frac{\Omega_{0,b}}{\Omega_{0,m}} \frac{1}{t_H(z)} \right] \ , \tag{7.8}$$

where $t_H(z)$ is the Hubble time and ϵ_{fid} is a fiducial normalization value calibrated on the physical properties of the source.
Although this formalism provides a suitable way to investigate the effects of ionization on the IGM state, the gas is modelled as a two-phases medium, composed by fully ionized and fully neutral region, and as a consequence the recombination is taken into account in an homogeneous manner. As pointed out by Mesinger & Dijkstra (2008), it can be a fairly accurate assumption at the early stages of reionization, but, as already discussed in Chapter 4, the effects of an inhomogeneous gas distribution can strongly affect the transmission of the flux.

7.2 The introduction of recombination: a preliminary approach

As already remarked, the next step of our work is the investigation of the IGM ionization history through reionization maps, that can be directly compared to the future observations on the new interferometers. In doing this, we will build a suitable semi-numerical approach, assuming the original model of (Mesinger & Furlanetto, 2007). But, given its limitations due to the approximate description of the IGM morphology, we will improve it, introducing a more accurate formalism for the inhomogeneous recombination, whose fundamental bases will be illustrated in this section.
As already shown for the semi-analytic approaches, the inhomogeneity of the IGM can affect the properties of the HII regions. In fact the inner high-density clumps of gas can absorb the ionizing radiation, preventing the growth of the ionized bubble. The capability of a HII region to absorb the ionizing photons can be described in terms of its optical depth τ. In fact, if $\tau \gtrsim 1$, the inner gas is clumpy enough to prevent the transmission of the flux, while the opposite is true for $\tau < 1$. In the Mesinger & Furlanetto (2007) formalism, this 'self-shielding' criterion can be introduced as follows. Once built a realization of the universe at a given z in which we locate the HII region and having estimated the flux field f through the Mesinger & Dijkstra (2008) model, for every ionized pixel we can estimate its inner neutral fraction as

$$x_{\rm HI}(\mathbf{x},z) = \rho_b(z)(1+\delta_n l(\mathbf{x},z)\alpha/\Gamma(\mathbf{x},z) \ , \tag{7.9}$$

where $\Gamma = f(\mathbf{x}, z)\sigma_{\rm HI}$ is the photoionization rate, ρ_b is the mean density of baryon at z and α is the recombination coefficient. Then, the optical depth results

$$\tau(\mathbf{x}, z) \equiv x_{\rm HI}(\mathbf{x}, z)\rho_b(z)(1 + \delta_n l(\mathbf{x}, z))\frac{L}{N'} \ , \tag{7.10}$$

in which we recall that L/N' is the grid spacing of the lower resolution box.
We now have the possibility to identify the high-density pixels inside the ionized regions through the self-shielding criterion. In fact, fixed a grid point $\mathbf{x}$ belonging to a HII bubble, if

$$\tau(\mathbf{x}, z) \geq 1 \tag{7.11}$$

the cell will be considered as a self-shielded pixel and will be re-marked as neutral in the reionization map.

7.3 The introduction of recombination: preliminary results

In this section, we will show the first results obtained by introducing the inhomogeneous recombination in the semi-analytic model of Mesinger & Furlanetto (2007). In the following discussion, we have adopted a cosmological framework according to the flat ΛCDM universe probed by the 5-year WMAP investigations.
As a first step, we build a realization of the overdensity field at $z = 0$ in a cubic box of $L = 100$ (comoving) Mpc, setting $N = 1600$ grid points per dimension. Then, we smooth it on progressively small scales, starting from L to $\mathrm{d}L$, so that we can identify the DM halos through the excursion-set formalism, according to the Mesinger & Furlanetto (2007) method. After the displacement of the collapsed halos to their Eulerian positions, we build several realizations of the ionization field, obtained by assuming different values for the free parameter ζ, on a low-resolution mesh characterized by $N' = 200$ grid points per dimension. We then calculate the corresponding flux fields, setting $\epsilon_{fid} = 1$.
Since the absorption due to the self-shielded region affects the transmission of the flux, we first test the reliability of the self-shielding criterion by comparing our assumed mfp L_{mfp} to that predicted by the total amount of such regions. We make our analisys at $z = 10$, assuming a proportionality parameter A for the total neutral fraction of the box, that can allow us to vary the amount of the self-shielded regions, and two different values for the theoretical mfp, i.e. $L_{mfp} = 10, 20$ (comoving) Mpc. These values are consistent with the extrapolation from the observed LLSs systems at $z < 4$. Then, according to Eq. 7.9, we compute the neutral fraction of each pixels. The resulting $x_{\rm HI}(\mathbf{x}, z)$ is multiplied by the A parameter, so that to assign an hypothetical neutral fraction $x'_{\rm HI} = Ax_{\rm HI}$ to all the pixels of the box. Finally, the application of Eq. 7.11 allows us to achieve the total density of neutral pixels $n_{\rm HI}$ corresponding to the fixed A, and the optical depth responsible for the flux absorption can be calculated according to the mfp l definition:

$$l = \frac{1}{\sqrt{2}n_{\rm HI}\mathrm{d}L'} \ , \tag{7.12}$$

in which $\mathrm{d}L' = L/N'$ is the grid spacing of the lower resolution box. Making it for a wide suitable range for the proportionality parameter, we can investigate the evolution of the expected mfp with respect to the amount of self-shielded regions predicted by our criterion. The comparison between the calculated l and the assumed mfp L_{mfp} will allow us to obtain the best-fit value of A that, in case of validity of our self-shielding prescription, is expected to be of the order of unity.
The resulting value for A of best fit are shown in Fig. 7.1, for the two values of L_{mfp} assumed in our analysis and different reionization phases at $z = 10$. Although its value increases at the early stages, A is of the order of unity for both the considered mfps, involving that the assumed self-shielding prescription is a suitable criterion to investigate the effects of recombination. In order to match the observed mfp, the following analysis will be made taking into account the correction on the neutral fraction estimate provided by the best-fit value of A.
An example of the effect of the absorption due to the inner recombination is illustrated in Fig. 7.2. Here, the white and black points represent the HII and the HI regions, respectively, after the

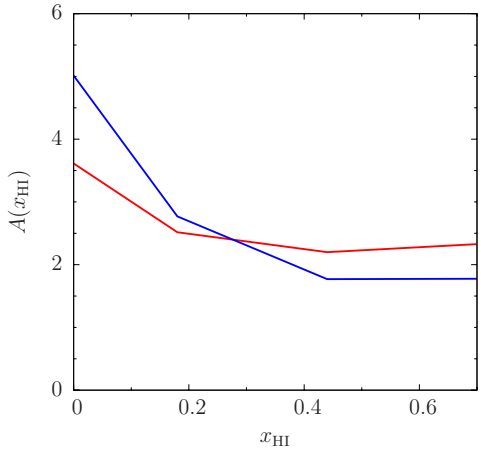

Figure 7.1: The resulting A of best fit calculated for a realization of the universe at $z = 10$ assuming $L_{mfp} = 10$ Mpc (red line) and 20 Mpc (blue line), for different ionization fractions x_{rmHI}.

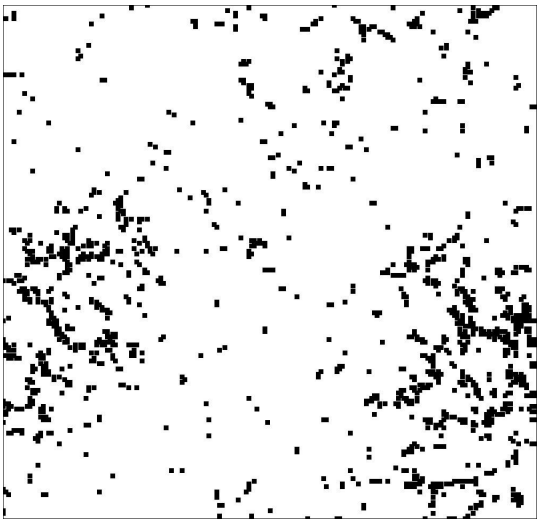

Figure 7.2: The effect of the inner recombination of the bubble provided by our self-shielding criterion, computed for a fully ionized universe at $z = 10$ assuming $L_{mfp} = 20$ Mpc. The white and the black points represents the ionized and the neutral cells, respectively.

application of the self-shieding criterion to a fully ionized universe at $z = 10$. Indeed, the resulting neutral fraction of the universe is increased, although by few ($\lesssim 3\%$) per cent. As shown in Fig. 7.3, we notice that the same trend is observed also for the other considered initial neutral fractions.
Another information that can be achieved by the reionization maps is the possible correlation of the self-shielded regions. In fact, as shown in Fig. 7.2, the distribution of the neutral pixels is not spatially homogeneous but is concentrated in some particular regions. A preliminary result of the correlation function $\xi(R)$ of the self-shielded pixels, computed assuming $L_{mfp} = 20$ Mpc and $z = 10$ for a fully ionized universe, is shown in Fig. 7.4. It is evident that $\xi(R)$ descreases at larger physical scales, anyway this result should be deeply investigated in a future work.

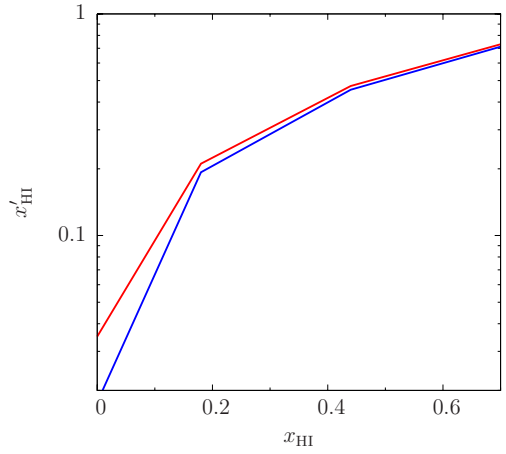

Figure 7.3: The resulting neutral fraction $x'_{\rm HI}$ calculated at $z = 10$ assuming the best-fit A values, for the initial ionization fraction $x_{\rm HI}$. The red and the blue lines correspond to $L_{mfp} = 10$ Mpc and 20 Mpc, respectively.

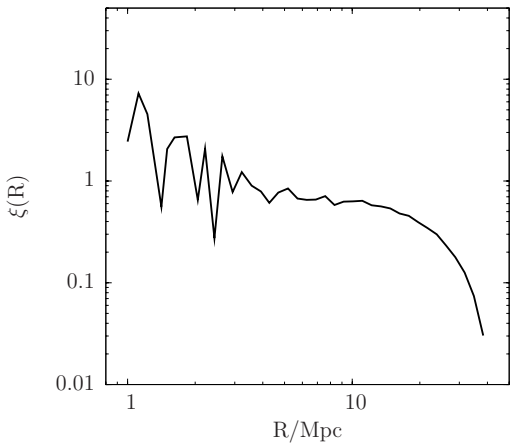

Figure 7.4: The resulting correlation function ξ of the self-shielded regions, calculated at $z = 10$ assuming $L_{mfp} = 20$ Mpc. The curve has been predicted for a fully ionized universe, i.e. $x_{\rm HI} = 0$.

Conclusions

The aim of this Thesis is to investigate the possibility that the observations related to the epoch of reionization can probe not only the evolution of the IGM state, but also the cosmological background in which this process occurs. In fact, the history of the IGM ionization is indeed affected by the evolution of the sources of ionizing photons that, under the assumption of a structure formation paradigm determined by the hierarchic growth of the matter fluctuations, results strongly dependent on the characteristics of the background universe.
For the purpose of our investigation, we have analysed the reionization history in innovative cosmological frameworks, still in agreement with the recent observational tests related to the SNIa and the CMB probes, comparing our results with the reionization scenario predicted by the commonly used ΛCDM cosmology. In particular, in this Thesis we have considered two different alternative universes. The first one is a flat universe dominated at late epochs by a dynamic dark energy component, characterized by an equation of state evolving in time. Our attention has been focused on the peculiar cosmological cases because they allow to avoid the theoretical troubles introduced by the cosmological constant and also because they do not conflict with the recent observations probed by SNIa. The second cosmological framework we have assumed is a ΛCDM characterized by a primordial overdensity field having a non-Gaussian probability distribution. Although the standard inflationary scenario predicts the rise of almost Gaussian matter fluctuations, actually a tiny deviation from the Gaussian statistics can arise from the self-interaction of the scalar field driving the expansion of the universe. We focused our attention on this particular cosmological background later on the last observations probed by the Local Large Scale Structures and the 5-year WMAP mission, that predict a small degree of non-Gaussianity.
The reionization scenario have been investigated, in this Thesis, through semi-analytic approaches based on the hierarichic growth of the matter fluctuations and on suitable assumptions concerning the ionization and the recombination of the IGM. Our choice has been directed towards these methods since our purpose is primarly the comparison between the global reionization scenarios predicted for the standard cosmology and the alternative universes, without focusing on a detailed investigation of the peculiarities of the HII regions. Moreover, a treatment concerning some aspects of reionization, as the recombination of the gas, has not been suitably developed yet through numerical simulations in the alternative cosmologies.
The main results of the application of the semi-analytic methods considered in this Thesis on the previous alternative cosmological frameworks have been summarized in the following topics.

Reionization in a quintessence universe

In investigating the reionization scenario predicted by these alternative universes, we introduce the dynamical dark energy component in a flat cosmological framework accordingly with the the Peebles & Ratra (2003) (RP) and Brax & Martin (2000) (SUGRA) models for the potential of the quintessence scalar field. Then, we used the analytic approach proposed by Furlanetto & Oh (2005) to outline the main differences between the evolution of bubbles in the quintessence models and in the standard ΛCDM cosmology. The main properties of the resulting reionization picture can be resumed as follows:

1. The dynamic dark energy component affects the evolution of the overdensity field. In fact, at the same redshift, the growth factor of the density fluctuations predicted in the quintessence scenario is larger than that expected in the standard universe. Then, the growth of the matter perturbations is anticipated in the SUGRA and RP cosmologies and the collapse of

the DM halos occurs early. Another important consequence is the decrease of the ionization barrier δ_x, that is lower in the RP and SUGRA universes compared to the ΛCDM one. This causes a strong increase of the high-density regions with respect to the ΛCDM case at the same epoch.

2. Neglecting the recombination limit and assuming the same ionization efficiency for all the three considered cosmologies, the distribution of the ionized bubbles in the quintessence cases is peaked at higher physical scales. The opposite is true setting the ionization efficiency such that reionization ends at $z \sim 6$, but the difference is weakened as reionization proceeds.

3. The hierarchical history of the HII regions in the quintessence cases is determined by the merging of more massive bubbles than in the standard framework. Moreover, the probability distribution of the bubble progenitors decreases in the SUGRA and RP models, since the merging bubbles are larger than the typical radius characterizing most of the HII regions.

4. In the recombination limit, the early growth of the matter fluctuations causes the increase of the IGM clumpiness and the inner recombination of the bubbles becomes more efficient. As a consequence, the HII regions reach the ionization equilibrium on slightly smaller scales and the bubble abundance increases. The IGM volume fraction contained in bubbles larger than $R_{\rm max}$ increases involving an earlier 'epoch of overlap' in the quintessence universe compared to ΛCDM.

5. The different evolution of the ionized regions affects the properties of IGM to allow the transmission of the Lyman flux coming from the high-z QSO. In fact, the probability distribution of the optical depth of the gas is lower for small values of τ in RP and SUGRA cosmologies compared to the ΛCDM model.

Reionization in a ΛCDM universe characterized by a non-Gaussian overdensity field

To describe the effects of a possible non-Gaussianity in the primordial overdensity field, we have adopted the simple analytic method introduced by Matarrese et al. (2000) based on the extension of the PS74 formalism to describe the evolution of the ionizing sources. We then apply the resulting structure formation paradigm to a semi-analytic model consistent with the Chen et al. (2003) and Avelino & Liddle (2006) approaches to make predictions on the evolution of the ionized fraction and the reionization optical depth. Our work extends previous analyses based on simplified ways to introduce primordial non-Gaussianity, considering models motivated by inflation. In particular we assume two different hierarchical evolution scenarios for the ionizing sources, characterized by scale-independent and scale-dependent non-Gaussianity. All scenarios here considered are in agreement with the constraints coming from the recent analysis of the 5-year WMAP data. The outlined reionization picture can be resumed as follows:

1. non-Gaussianity affects the abundance of the dark matter haloes, since the formation of high-mass collapsed objects is enhanced (reduced) when positive (negative) values for the $f_{\rm NL}$ parameter are assumed. This effect is stronger at earlier cosmological epochs, i.e. when reionization begins.

2. As a consequence, for positive primordial non-Gaussianity, the collapsed fraction in type Ia and Ib sources is higher than for the Gaussian case at the same epoch, and the difference increases with z. The opposite result applies for negative $f_{\rm NL}$ parameters.

3. The IGM filling factor is higher and its evolution is faster than in the Gaussian scenario if a positive $f_{\rm NL}$ is assumed. This effect is enhanced for a scale-dependent non-Gaussianity, that can produce a 5 times higher $F_{\rm HII}$ with respect to the Gaussian case, at early cosmological epochs. Viceversa the filling factor is smaller and has a mild redshift evolution for negative $f_{\rm NL}$.

4. Both local and equilateral non-Gaussianity have a small (less than 10 per cent) impact on the reionization optical depth, but the effect is enhanced assuming a scale-dependent $f_{\rm NL}$ parameter.

5. Our predictions of the reionization optical depth in non-Gaussian cosmologies are in agreement with that estimated by 5-year WMAP analysis within 1σ error bars, but a precision higher than that of WMAP is required to constrain non-Gaussianity and its scale dependence.

As already discussed, the semi-analytic methods used in this Thesis suffer of several limitations due to their approximate way to describe some fundamental aspects, as the clustering of the sources and the inhomogeneous nature of the IGM recombination, that can indeed affect the physical properties of the ionized regions and the global evolution of the reionization process. Then, the next step of our investigation will be to make numerical simulations to predict the ionization state of the IGM at different redshifts that can be compared to the future observations of the new interferometers. Works are in progress to build a suitable theoretical model for reionization.

Bibliography

Adler R. J., 1981, The Geometry of Random Fields. The Geometry of Random Fields, Chichester: Wiley, 1981

Albrecht A., Steinhardt P. J., 1982, Physical Review Letters, 48, 1220

Avelino P. P., Liddle A. R., 2006, MNRAS, 371, 1755

Baek S., di Matteo P., Semelin B., Combes F., Revaz Y., 2009, A&A, 495, 389

Bardeen J. M., Bond J. R., Kaiser N., Szalay A. S., 1986, ApJ, 304, 15

Barkana R., 2008, preprint, arXiv:0806.2333

Barkana R., Loeb A., 2001, Phys. Rep., 349, 125

Barnes J., Hut P., 1986, Nat, 324, 446

Bartelmann M., Doran M., Wetterich C., 2006, A&A, 454, 27

Becker G. D., Rauch M., Sargent W. L. W., 2007, ApJ, 662, 72

Becker R. H., et al., 2001, AJ, 122, 2850

Benson A. J., Sugiyama N., Nusser A., Lacey C. G., 2006, MNRAS, 369, 1055

Benson A. J., Kamionkowski M., Hassani S. H., 2005, MNRAS, 357, 847

Bolton J. S., Haehnelt M. G., 2007b, MNRAS, pp L81+

Bolton J. S., Haehnelt M. G., 2007a, MNRAS, 382, 325

Bolton J., Meiksin A., White M., 2004, MNRAS, 348, L43

Bond J. R., Myers S. T., 1996, ApJS, 103, 41

Bond J. R., Cole S., Efstathiou G., Kaiser N., 1991, ApJ, 379, 440

Brax P., Martin J., 2000, Phys. Rev. D, 61, 103502

Bruscoli M., Ferrara A., Scannapieco E., 2002, MNRAS, 330, L43

Bryan G. L., Norman M. L., 1998, ApJ, 495, 80

Carbone C., Verde L., Matarrese S., 2008, ApJ, 684, L1

Carroll S. M., Press W. H., Turner E. L., 1992, ARA&A, 30, 499

Cen R., 2003, ApJ, 591, 12

Cen R., 2002, ApJS, 141, 211

Cen R., Haiman Z., 2000, ApJ, 542, L75

Charbonnel C., Primas F., 2005, A&A, 442, 961

Chen X., Kamionkowski M., 2004, Phys. Rev. D, 70, 043502

Chen X., Cooray A., Yoshida N., Sugiyama N., 2003, MNRAS, 346, L31

Chiu W. A., Ostriker J. P., 2000, ApJ, 534, 507

Choudhury T. R., Haehnelt M. G., Regan J., 2008, preprint, arXiv:0806.1524

Choudhury T. R., Ferrara A., 2006, MNRAS, 371, L55

Ciardi B., Madau P., 2003, ApJ, 596, 1

Ciardi B., Ferrara A., Marri S., Raimondo G., 2001, MNRAS, 324, 381

Ciardi B., Loeb A., 2000, ApJ, 540, 687

Ciardi B., Ferrara A., Abel T., 1998, preprint, arXiv:astro-ph/9811137

Cohn J. D., Chang T.-C., 2007, MNRAS, 374, 72

Cojazzi P., Bressan A., Lucchin F., Pantano O., Chavez M., 2000, MNRAS, 315, L51

Creminelli P., Nicolis A., Senatore L., Tegmark M., Zaldarriaga M., 2006, Journal of Cosmology and Astro-Particle Physics, 5, 4

Croft R. A. C., Altay G., 2008, MNRAS, 388, 1501

Dalal N., Doré O., Huterer D., Shirokov A., 2008, Phys. Rev. D, 77, 123514

Desjacques V., Seljak U., Iliev I. T., 2008, preprint, arXiv:0811.2748

Desjacques V., Nusser A., 2005, MNRAS, 361, 1257

Di Matteo T., Ciardi B., Miniati F., 2004, MNRAS, 355, 1053

Djorgovski S. G., Castro S., Stern D., Mahabal A. A., 2001, ApJ, 560, L5

Dunkley J., Komatsu E., Nolta M. R., Spergel D. N., et al., 2008, preprint, arXiv:0803.0586

Einstein A., 1915a, Sitzungsberichte der Königlich Preußischen Akademie der Wissenschaften (Berlin), Seite 778-786., pp 778–786

Einstein A., 1915b, Sitzungsberichte der Königlich Preußischen Akademie der Wissenschaften (Berlin), Seite 799-801., pp 799–801

Einstein A., 1916, Annalen der Physik, 354, 769

Eisenstein D. J., Hu W., 1998, ApJ, 496, 605

Eke V. R., Cole S., Frenk C. S., 1996, MNRAS, 282, 263

Fan X., Hennawi J. F., Richards G. T., Strauss M. A., Schneider D. P., Donley J. L., Young J. E., Annis J., Lin H., Lampeitl H., et al., 2004, AJ, 128, 515

Fan X., Strauss M. A., Schneider D. P., Becker R. H., White R. L., Haiman Z., Gregg M., Pentericci L., Grebel E. K., Narayanan et al., 2003, AJ, 125, 1649

Fang T., Cen R., 2004, ApJ, 616, L87

Feng L., Bi H., Liu J., Fang L.-Z., 2008, MNRAS, 383, 1459

Furlanetto S. R., Oh S. P., 2008b, ApJ, 682, 14

Furlanetto S. R., Oh S. P., 2008a, ApJ, 681, 1

Furlanetto S. R., Oh S. P., 2005, MNRAS, 363, 1031

Furlanetto S. R., Briggs F. H., 2004c, New Astronomy Review, 48, 1039

Furlanetto S. R., Hernquist L., Zaldarriaga M., 2004b, MNRAS, 354, 695

Furlanetto S. R., Zaldarriaga M., Hernquist L., 2004a, ApJ, 613, 1

Gallerani S., Salvaterra R., Ferrara A., Choudhury T. R., 2008, MNRAS, 388, L84

Gallerani S., Ferrara A., Fan X., Choudhury T. R., Salvaterra R., 2007, Nuovo Cimento B Serie, 122, 977

Gallerani S., Choudhury T. R., Ferrara A., 2006, MNRAS, 370, 1401

Geil P. M., Wyithe J. S. B., 2008, MNRAS, 386, 1683

Gleser L., Nusser A., Benson A. J., Ohno H., Sugiyama N., 2005, MNRAS, 361, 1399

Gnedin N. Y., 2000b, ApJ, 542, 535

Gnedin N. Y., 2000a, ApJ, 535, 530

Gnedin N. Y., Ostriker J. P., 1997, ApJ, 486, 581

Gordon C., Land K., Slosar A., 2007, Physical Review Letters, 99, 081301

Goto T., 2006, MNRAS, 371, 769

Grossi M., Verde L., Carbone C., Dolag K., Branchini E., Iannuzzi F., Matarrese S., Moscardini L., 2009, preprint, arXiv:0902.2013

Grossi M., Dolag K., Branchini E., Matarrese S., Moscardini L., 2007, MNRAS, 382, 1261

Gunn J. E., Peterson B. A., 1965, ApJ, 142, 1633

Guth A. H., 1981, Phys. Rev. D, 23, 347

Haiman Z., Bryan G. L., 2006, ApJ, 650, 7

Haiman Z., Holder G. P., 2003, ApJ, 595, 1

Haiman Z., Loeb A., 1997, ApJ, 483, 21

Hansen F. K., Balbi A., Banday A. J., Górski K. M., 2004, MNRAS, 354, 905

Harrison E. R., 1970, Phys. Rev. D, 1, 2726

Heap S. R., Williger G. M., Smette A., Hubeny I., Sahu M. S., Jenkins E. B., Tripp T. M., Winkler J. N., 2000, ApJ, 534, 69

Holder G. P., Haiman Z., Kaplinghat M., Knox L., 2003, ApJ, 595, 13

Hu E. M., Cowie L. L., McMahon R. G., Capak P., Iwamuro F., Kneib J.-P., Maihara T., Motohara K., 2002, ApJ, 568, L75

Hu W., 2000, in Bulletin of the American Astronomical Society Vol. 32 of Bulletin of the American Astronomical Society, The Physics of Cosmic Microwave Background Anisotropies and their Cosmological Implications. pp 1448–+

Hui L., Haiman Z., 2003, ApJ, 596, 9

Iliev I. T., Shapiro P. R., McDonald P., Mellema G., Pen U.-L., 2008c, MNRAS, 391, 63

Iliev I. T., Pen U.-L., McDonald P., Shapiro P. R., Mellema G., Alvarez M. A., 2008b, Ap&SS, pp 145–+

Iliev I. T., Shapiro P. R., Mellema G., Merz H., Pen U.-L., 2008a, preprint, arXiv:0806.2887

Iliev I. T., Mellema G., Shapiro P. R., Pen U.-L., 2007, MNRAS, 376, 534

Iliev I. T., Pen U.-L., Richard Bond J., Mellema G., Shapiro P. R., 2006b, New Astronomy Review, 50, 909

Iliev I. T., Mellema G., Pen U.-L., Merz H., Shapiro P. R., Alvarez M. A., 2006a, MNRAS, 369, 1625

Iliev I. T., Shapiro P. R., Raga A. C., 2005, MNRAS, 361, 405

Iye M., Ota K., Kashikawa N., Furusawa H., Hashimoto T., Hattori T., Matsuda Y., Morokuma T., Ouchi M., Shimasaku K., 2006, Nat, 443, 186

Jedamzik K., 1995, ApJ, 448, 1

Jenkins A., Frenk C. S., White S. D. M., Colberg J. M., Cole S., Evrard A. E., Couchman H. M. P., Yoshida N., 2001, MNRAS, 321, 372

Kanekar N., Briggs F. H., 2004, New Astronomy Review, 48, 1259

Kashikawa N., et al., 2006, ApJ, 648, 7

Kasuya S., Kawasaki M., 2007, Journal of Cosmology and Astro-Particle Physics, 2, 10

Kim T.-S., Bolton J. S., Viel M., Haehnelt M. G., Carswell R. F., 2007, MNRAS, 382, 1657

Kohler K., Gnedin N. Y., Miralda-Escudé J., Shaver P. A., 2005, in Kassim N., Perez M., Junor W., Henning P., eds, Astronomical Society of the Pacific Conference Series Vol. 345 of Astronomical Society of the Pacific Conference Series, Redshifted 21 cm Emission from the Pre-Reionization Era. H II Regions Around Individual Quasars. pp 304–+

Komatsu E., et al., 2008, preprint, arXiv:0803.0547

Komatsu E., Spergel D. N., 2001, Phys. Rev. D, 63, 063002

Kurk J. D., Cimatti A., di Serego Alighieri S., Vernet J., Daddi E., Ferrara A., Ciardi B., 2004, A&A, 422, L13

Lacey C., Cole S., 1993, MNRAS, 262, 627

Lee J., Shandarin S. F., 1998, ApJ, 500, 14

Liddle A. R., Mukherjee P., Parkinson D., Wang Y., 2006, Phys. Rev. D, 74, 123506

Lidz A., McQuinn M., Zaldarriaga M., Hernquist L., Dutta S., 2007, ApJ, 670, 39

Liguori M., Riotto A., 2008, preprint, arXiv:0808.3255

Linde A. D., 1983, Physics Letters B, 129, 177

Linde A. D., 1982b, Physics Letters B, 116, 335

Linde A. D., 1982a, Physics Letters B, 108, 389

Liu J., Bi H., Fang L., 2007, in Bulletin of the American Astronomical Society Vol. 38 of Bulletin of the American Astronomical Society, Lyα Leaks in the Absorption Spectra of High Redshift QSOs. pp 875–+

Lo Verde M., Miller A., Shandera S., Verde L., 2008, J. Cosmology Astropart. Phys., 4, 14

Loeb A., 2008, preprint, arXiv:0812.2222

Loeb A., 2006, preprint, arXiv:astro-ph/0603360

Loeb A., Zaldarriaga M., 2004, Physical Review Letters, 92, 211301

Madau P., Rees M. J., Volonteri M., Haardt F., Oh S. P., 2004, ApJ, 604, 484

Malhotra S., Rhoads J. E., 2004, ApJ, 617, L5

Mantz A., Allen S. W., Ebeling H., Rapetti D., 2008, MNRAS, 387, 1179

Mapelli M., Ferrara A., Pierpaoli E., 2006, MNRAS, 369, 1719

Mapelli M., Ferrara A., 2005, MNRAS, 364, 2

Matarrese S., Verde L., 2008, ApJ, 677, L77

Matarrese S., Verde L., Jimenez R., 2000, ApJ, 541, 10

McDonald P., Seljak U., Cen R., Shih D., et al., 2005, ApJ, 635, 761

McQuinn M., Lidz A., Zaldarriaga M., Hernquist L., Dutta S., 2008, MNRAS, 388, 1101

McQuinn M., Hernquist L., Zaldarriaga M., Dutta S., 2007, MNRAS, 381, 75

McQuinn M., Zahn O., Zaldarriaga M., Hernquist L., Furlanetto S. R., 2006, ApJ, 653, 815

Mesinger A., Dijkstra M., 2008, MNRAS, 390, 1071

Mesinger A., Furlanetto S., 2007, ApJ, 669, 663

Mesinger A., Haiman Z., Cen R., 2004b, ApJ, 613, 23

Mesinger A., Haiman Z., 2004a, ApJ, 611, L69

Meszaros P., 1974, A&A, 37, 225

Miniati F., Ferrara A., White S. D. M., Bianchi S., 2004, MNRAS, 348, 964

Miralda-Escudé J., 2003, ApJ, 597, 66

Miralda-Escudé J., Haehnelt M., Rees M. J., 2000, ApJ, 530, 1

Mota D. F., van de Bruck C., 2004, A&A, 421, 71

Mukherjee P., Liddle A. R., 2008, MNRAS, 389, 231

Nagashima M., Gouda N., 1997, MNRAS, 287, 515

Oguri M., Inada N., Strauss M. A., Kochanek C. S., et al., 2008, AJ, 135, 512

Oh S. P., Furlanetto S. R., 2005, ApJ, 620, L9

Oh S. P., 2001, ApJ, 553, 499

O'Meara J. M., Burles S., Prochaska J. X., Prochter G. E., Bernstein R. A., Burgess K. M., 2006, ApJ, 649, L61

Ota K., 2007, Astronomical Herald, 100, 25

Padmanabhan T., 1993, Structure Formation in the Universe. Structure Formation in the Universe, by T. Padmanabhan, pp. 499. ISBN 0521424860. Cambridge, UK: Cambridge University Press, June 1993.

Paschos P., Norman M. L., Bordner J. O., Harkness R., 2007, preprint, arXiv:0711.1904

Peebles P. J., Ratra B., 2003, Reviews of Modern Physics, 75, 559

Peebles P. J., 1993, Nat, 365, 117

Percival W. J., Baugh C. M., Bland-Hawthorn J., et al., 2001, MNRAS, 327, 1297

Pillepich A., Porciani C., Hahn O., 2008, preprint, arXiv:0811.4176

Press W. H., Schechter P., 1974, ApJ, 187, 425

Pritchard J. R., Furlanetto S. R., 2007, MNRAS, 376, 1680

Ratra B., Peebles P. J. E., 1988, Phys. Rev. D, 37, 3406

Rauch M., Miralda-Escude J., Sargent W. L. W., et al., 1997, ApJ, 489, 7

Rhook K. J., Haehnelt M. G., 2006, The Universe at z > 6, 26th meeting of the IAU, Joint Discussion 7, 17-18 August 2006, Prague, Czech Republic, JD07, #43, 7

Ricotti M., Ostriker J. P., 2004b, MNRAS, 352, 547

Ricotti M., Ostriker J. P., 2004a, MNRAS, 350, 539

Ripamonti E., Mapelli M., Zaroubi S., 2008, MNRAS, 387, 158

Robertson H. P., 1935, ApJ, 82, 284

Robertson H. P., 1933, Reviews of Modern Physics, 5, 62

Rozas J. M., Miralda-Escude J., Salvador-Sole E., 2005, preprint, arXiv:astro-ph/0511489

Salvaterra R., Ciardi B., Ferrara A., Baccigalupi C., 2005, MNRAS, 360, 1063

Santos M. G., Amblard A., Pritchard J., Trac H., Cen R., Cooray A., 2008, ApJ, 689, 1

Schaerer D., 2002, A&A, 382, 28

Schneider R., Salvaterra R., Ferrara A., Ciardi B., 2006, MNRAS, 369, 825

Schneider R., Ferrara A., Natarajan P., Omukai K., 2002, ApJ, 571, 30

Seljak U., 2009, Physical Review Letters, 102, 021302

Seljak U., Makarov A., McDonald P., Anderson S. F., et al., 2005, Phys. Rev. D, 71, 103515

Sethi S. K., Subramanian K., 2005, MNRAS, 356, 778

Shapiro P. R., Iliev I. T., Mellema G., Pen U.-L., Merz H., 2008, in Minchin R., Momjian E., eds, The Evolution of Galaxies Through the Neutral Hydrogen Window Vol. 1035 of American Institute of Physics Conference Series, The Theory and Simulation of the 21-cm Background from the Epoch of Reionization. pp 68–74

Shapiro P. R., Iliev I. T., Raga A. C., 2004, MNRAS, 348, 753

Shapiro P. R., Giroux M. L., 1987, ApJ, 321, L107

Sheth R. K., Mo H. J., Tormen G., 2001, MNRAS, 323, 1

Sheth R. K., Tormen G., 1999, MNRAS, 308, 119

Sheth R. K., 1998, MNRAS, 300, 1057

Slosar A., Hirata C., Seljak U., Ho S., Padmanabhan N., 2008, J. Cosmology Astropart. Phys., 8, 31

Sokasian A., Abel T., Hernquist L., Springel V., 2003, MNRAS, 344, 607

Songaila A., 1998, AJ, 115, 2184

Songaila A., Cowie L. L., 1996, AJ, 112, 335

Spergel D. N., et al., 2007, ApJS, 170, 377

Spergel D. N., et al., 2003, ApJS, 148, 175

Springel V., White S. D. M., Jenkins A., Frenk C. S., Yoshida N., Gao L., Navarro J., Thacker R., Croton D., Helly J., Peacock J. A., Cole S., Thomas P., Couchman H., Evrard A., Colberg J., Pearce F., 2005, Nat, 435, 629

Stark D., Ellis R., Richard J., 2007b, in Bulletin of the American Astronomical Society Vol. 38 of Bulletin of the American Astronomical Society, The Case for an Abundant Population of Feeble Lyman-alpha Emitting Galaxies at z $>$ 8. pp 995–+

Stark D. P., Ellis R. S., Richard J., Kneib J.-P., Smith G. P., Santos M. R., 2007a, ApJ, 663, 10

Steigman G., 2007, Annual Review of Nuclear and Particle Science, 57, 463

Steinhardt P. J., Caldwell R. R., 1998, in Byun Y. I., Ng K. W., eds, Cosmic Microwave Background and Large Scale Structure of the Universe Vol. 151 of Astronomical Society of the Pacific Conference Series, Introduction to Quintessence. pp 13–+

Straumann N., 2004, General relativity with applications to astrophysics. General relativity with applications to astrophysics, by Norbert Straumann. Springer Texts and monographs in physics. Berlin: Springer, 2004

Sugiyama N., 1995, ApJS, 100, 281

Sugiyama N., Silk J., Vittorio N., 1993, ApJ, 419, L1+

Taniguchi Y., Ajiki M., Nagao T., Shioya Y., et al., 2005, PASJ, 57, 165

Tashiro H., Sugiyama N., 2006, MNRAS, 368, 965

Thomas R. M., Zaroubi S., Ciardi B., Pawlik A. H., et al., 2009, MNRAS, 393, 32

Thomas R. M., Zaroubi S., 2008, MNRAS, 384, 1080

Totani T., Kawai N., Kosugi G., Aoki K., et al., 2006, The Universe at z $>$ 6, 26th meeting of the IAU, Joint Discussion 7, 17-18 August 2006, Prague, Czech Republic, JD07, #19, 7

Trac H., Cen R., 2007, ApJ, 671, 1

Trenti M., Stiavelli M., 2009, preprint, arXiv:0901.0711

Venkatesan A., Tumlinson J., Shull J. M., 2003, ApJ, 584, 621

Verde L., Jimenez R., Kamionkowski M., Matarrese S., 2001, MNRAS, 325, 412

Viel M., Weller J., Haehnelt M. G., 2004, MNRAS, 355, L23

Walker A. G., 1933, MNRAS, 94, 159

Wang P., 2006, ApJ, 640, 18

Wang J. X., Malhotra S., Rhoads J. E., 2005, ApJ, 622, L77

Wang L., Steinhardt P. J., 1998, ApJ, 508, 483

Warren M. S., Abazajian K., Holz D. E., Teodoro L., 2006, ApJ, 646, 881

White R. L., Becker R. H., Fan X., Strauss M. A., 2003, AJ, 126, 1

Willis J. P., Courbin F., 2005, MNRAS, 357, 1348

Willott C. J., Delorme P., Reyle C., Albert L., et al., 2009, preprint, arXiv:0901.0565

Willott C. J., Delorme P., Omont A., Bergeron J., et al., 2007, AJ, 134, 2435

Wood-Vasey W. M., Miknaitis G., Stubbs C. W., et al., 2007, ApJ, 666, 694

Wyithe J. S. B., Loeb A., 2007, MNRAS, 375, 1034

Wyithe J. S. B., Loeb A., Barnes D. G., 2005b, ApJ, 634, 715

Wyithe J. S. B., Loeb A., Carilli C., 2005a, ApJ, 628, 575

Wyithe J. S. B., Loeb A., 2004, Nat, 427, 815

Wyithe J. S. B., Loeb A., 2003, ApJ, 586, 693

Zahn O., Zaldarriaga M., Hernquist L., McQuinn M., 2005, ApJ, 630, 657

Zaldarriaga M., Hui L., Tegmark M., 2001, ApJ, 557, 519

Zaroubi S., Thomas R. M., Sugiyama N., Silk J., 2007, MNRAS, 375, 1269

Zaroubi S., Silk J., 2005, MNRAS, 360, L64

Zel'Dovich Y. B., 1970, A&A, 5, 84

Zhang J., Hui L., Haiman Z., 2007, MNRAS, 375, 324

Contents